TECHNISCHE UNIVERSITÄT WIEN
Vienna University of Technology

Development of Tissue Mimicking Materials for Functional Anatomical Models

Towards Improved Surgical Rehearsal

DISSERTATION

carried out for the purpose of obtaining the degree of Doctor technicae (Dr. techn.) at TU Wien
Faculty of Mechanical and Industrial Engineering

by

Othniel James Aryeetey, MSc.
Matriculation Number 11946407

under the supervision
Univ. Prof Dr. techn. Dipl. -Ing. Dieter Pahr

Institute of Lightweight Design and Structural Biomechanics (ILSB) E317

The dissertation has been reviewed by:

Prof. Dr. Thomas C. Gasser KTH Royal Institute of Technology, Stockholm Sweden	Associate Prof. Dr.in techn. Melanie Todt ILSB, TU Wien, Vienna, Austria

Declaration of Authorship

I declare in lieu of oath, that I wrote this thesis and performed the associated research myself, using only literature cited in this volume. If text passages from sources are used literally, they are marked as such. I confirm that this work is original and has not been submitted elsewhere for any examination, nor is it currently under consideration for a thesis elsewhere. I acknowledge that the submitted work will be checked electronically and technically using suitable and state-of-the-art means (plagiarism detection software). On the one hand, this ensures that the submitted work was prepared according to the high-quality standards within the applicable rules to ensure good scientific practice "Code of Conduct" at the TU Wien. On the other hand, a comparison good scientific practice "Code of Conduct" at the TU Wien. On the other hand, a comparison with other student theses avoids violations of my personal copyright.

Funding

The research was a cooperation with the Austrian Center for Medical Innovation and Technology (ACMIT), funded in the "Forschung, Technologie & Innovation" (FTI) framework of the Provincial Government of Lower Austria (Land Niederösterreich) under grant assignment number WST3-F2-528983/005-2018. The authors want to appreciate the contribution of Lower Austria Landesgesundheitsagentur, legal entity of University Hospitals in Lower Austria, as well as the cooperation and support of the Austrian Center for Medical Innovationa & Technology (ACMIT), for providing the organizational framework to conduct this research. The authors acknowledge the TU Wien Bibliothek for financial support through its Open Access Funding Programme.

Acknowledgements

I extend my deepest gratitude to my supervisor, **Dieter Pahr**, for his invaluable support and guidance throughout my PhD. His extensive research experience was instrumental in helping me navigate this challenging journey.

Special thanks to **Martin Bittner-Frank** for his consistent guidance, helpful feedback, and most importantly, his steadfast encouragement. I am profoundly grateful for his support. I am thankful to my colleague, **Laszlo Jaksa**, whose contributions were crucial to the success of our project. I also owe a big thank you to **Andrea Lorenz** for her support and great insights and feedback.

Additionally, I appreciate my colleagues **Nedaa Amraish, Sarah-Jane Estermann, Katharina Nägl, Juan Diego Silva,** and **Lukas Warnung** and colleagues at the **Institute of Lightweight Design and Structural Biomechanics** for their productive discussions, as well as the enjoyable moments we shared. As well as thanks to **Andreas Reisinger** for all his assistance during my tenure at the **Karl Landsteiner University of Health Sciences**.

Finally, I am heartfully thankful to my friends and family, especially my wife **Julia Aryeetey** for her unwavering emotional support and and my daughter **Elora Aryeetey** for being my motivation, which were vital to the completion of my research work.

Abstract

The importance of advanced surgical preparation is crucial for improving treatment outcomes of patients. The integration of 3D-printed anatomical models is becoming increasingly important and has significantly improved the visualization of complex anatomical structures, and hence surgical training and surgical planning. Despite advancements in the design and creation of such models, they often fail to accurately replicate the mechanical properties of soft tissues. Characterizing these mechanical properties is complex, and producing tissues that accurately match these properties is a considerable challenge.

This dissertation introduces innovative methodologies for the modeling, characterization, and replication of soft biological tissues, and makes an important contribution in terms of biomechanical understanding of anatomical models towards surgical planning. The results presented apply a "parameter-reduced" adaptive quasi-linear viscoelastic (AQLV) material model designed to handle the complexities of soft tissue behavior at finite strains. This model not only simplifies the experimental characterization of viscoelastic properties, but also facilitates precise comparisons between different fabric types.

Building on this basic model, the dissertation extends its application to the challenging area of fracture toughness prediction in soft tissues, specifically targeting porcine liver and muscle. By differentiating strain-dependent viscous dissipated energies, the improved AQLV model provides deeper insights into the viscoelastic and fracture behavior of soft collagenous tissues and paves the way for improved biomechanical models.

With the building blocks to characterize the mechanical properties of soft biological tissues, another goal was to develop 3D printable tissues that better match those of the characterized soft tissues. Here, microstructuring techniques, fiber reinforcement and fluid injection are performed during the 3D printing process to achieve realistic mechanical properties of the synthetic tissues. This approach significantly refines the fidelity of 3D-printed anatomical models used for surgical planning and training and provides a pathway to more effective and error-free surgical procedures.

In summary, this dissertation establishes efficient methods for biomechanical characterization of soft tissue and provides a methodology for producing more realistic tissue-like materials for use as anatomical models, with far-reaching implications for surgical education and training as well as general patient care.

Kurzfassung

Die Bedeutung einer fortgeschrittenen chirurgischen Vorbereitung ist entscheidend für die Verbesserung der Behandlungsergebnisse der Patienten. Die Integration von 3D-gedruckten anatomischen Modellen gewinnt zunehmend an Bedeutung und hat die Visualisierung komplexer anatomischer Strukturen revolutioniert und damit die chirurgische Ausbildung sowie chirurgische Planung erheblich verbessert. Trotz Fortschritten in Design und Erstellung solcher Modelle gelingt es oft nicht, die mechanischen Eigenschaften weicher Gewebe genau nachzubilden. Die Charakterisierung dieser mechanischen Eigenschaften ist komplex, und die Herstellung von Geweben, die diese Eigenschaften genau abbilden, stellt eine erhebliche Herausforderung dar.

Diese Dissertation führt innovative Methoden für die Modellierung, Charakterisierung und Replikation von weichen biologischen Geweben ein und leistet einen wichtigen Beitrag hinsichtlich der chirurgischen Vorbereitung und des biomechanischen Verständnisses. Die vorgestellten Ergebnisse wendet ein "parameterreduziertes" adaptives quasi-lineares viskoelastisches (AQLV) Materialmodell an, das darauf ausgelegt ist, die Komplexitäten des Verhaltens weicher Gewebe bei endlichen Dehnungen zu bewältigen. Dieses Modell vereinfacht nicht nur die experimentelle Charakterisierung von viskoelastischen Eigenschaften, sondern erleichtert auch präzise Vergleiche zwischen verschiedenen Gewebetypen.

Aufbauend auf diesem Grundmodell erweitert die Dissertation dessen Anwendung auf den herausfordernden Bereich der Vorhersage der Bruchzähigkeit in weichen Geweben, insbesondere zielt sie auf Schweineleber und -muskel ab. Durch die Differenzierung von dehnungsabhängigen viskosen dissipierten Energien bietet das verbesserte AQLV-Modell tiefere Einblicke in das viskoelastische und Bruchverhalten von weichen kollagenösen Geweben und ebnet den Weg für verbesserte biomechanische Modelle.

Mit den Bausteinen zur Charakterisierung der mechanischen Eigenschaften von weichen biologischen Geweben war ein weiteres Ziel, 3D-druckbare Gewebe zu entwickeln, welche besser denen der charakterisierten weichen Gewebe entsprechen. Hierbei werden Mikrostrukturierungstechniken, Faserverstärkung und Flüssigkeitseinbringung während des 3D-Druckprozess durchgeführt, um realistische mechanischen Eigenschaften der synthetischen Gewebe zu erreichen. Dieser Ansatz verfeinert erheblich die Realitätstreue von 3D-gedruckten anatomischen Modellen, die für die chirurgische Planung und Ausbildung verwendet werden, und bietet einen Weg zu effektiveren und fehlerfreien chirurgischen Verfahren.

Zusammenfassend etabliert diese Dissertation effiziente Methoden zur biomechanischen Charakterisierung von weichem Gewebe und bietet eine Methodik zur Herstellung realistischerer gewebeähnlicher Materialien für den Einsatz als anatomische Modelle, mit weitreichenden Implikationen für die chirurgische Ausbildung und das Training sowie die allgemeine Patientenversorgung.

Contents

List of Symbols

σ Engineering stress

ϵ Engineering strain

A_0 Cross sectional area

L_0 Original length

L Deformed length

f Force

k Spring constant

b Damper coefficients

a Crack length

$V(\epsilon)$ Non-linear function of strain

$G(t)$ Relaxation function

t Time

τ Relaxation time

γ Integral of relaxation function (g(t))

E' Storage modulus

E'' Loss modulus

E_0 Instantaneous modulus

E_∞ Long term modulus

ω Angular frequency

$U_\mathbf{D}$ Dissipated energy ratio

$W_\mathbf{T}$ Total energy

$W_\mathbf{D}$ Dissipated energy

$W_\mathbf{S}$ Storage energy

$J_\mathbf{c}$ Fracture toughness parameter

B Thickness

$W_\mathbf{F}$ Fracture energy

$\tan\delta$ Tangent delta

List of Abbreviations

AQLV Adaptive Quasi-linear viscoelastic

ANLV Attenuated non-linear viscoelastic

TMM Tissue mimicking materials

LOOCV Leave One Out cross validation

RMSE Root mean square error

R2 R^2 Coefficient of determination

DIC Digital Image correlation

SCT Soft collagenous tissues

GC Glissons capsule

CCC Collagen type 1

3D 3 dimensional

FDM Fused deposition modeling

SRS Suture retention strength

BSS Break start strength

TPU Thermoplastic polyurethane

ELK Elkem

G30 Gyroid 30%

Fib Fibre reinforced

Flu Infill Fluid

PLA Polylactic acid

CHAPTER 1

Introduction

1.1 Problem Statement

Modern medical advancements aim to enhance patient care and outcomes. One statistic underscores the need for such progress: medical errors have been implicated in an average of 250,000 patient deaths annually in the United States alone [86]. Over 4000 incidents of surgical "never events" are estimated to occur in the United States alone annually [90]. "Never events" refer to sever incidents that are highly preventable. In the United Kingdom, a survey of the acute National Health Service trusts showed that a total of 742 surgically related "Never Events" occurred over three years, spanning between 2011 and 2014, with no significant difference in annual numbers [97]. In response, there has been a concerted effort to mitigate such risks, particularly through refined surgical planning and training methodologies. This has led to advancements in high resolution, non-invasive imaging techniques as well as the increased utilization of anatomical models in surgical research, training and rehearsal in the past few decades [46].

Although advanced imaging techniques have led to improved patient outcomes due to increased capture of intricate details of anatomical structures, 2D portrayal of organs may obscure the complex spatial relationship between soft tissues [87]. Recognizing this limitation, the integration of three-dimensional (3D) virtual models has emerged as a pivotal solution, offering enhanced visualization and communication capabilities [116]. Yet, for medical professionals, the absence of tactile feedback inherent in virtual models poses a significant drawback for surgical practice and rehearsal. The coupling of additive manufacturing, also known as 3D printing and 3D virtual models have led to the creation of intircate, patient- specific anatomical models [12, 123]. These anatomical replicas not only address the deficiency of tactile feedback but have also demonstrated profound impacts on pre-operative planning, implant customization, intra-operative guidance, and patient communication [163, 154]. 3D printing of anatomical models for surgical rehearsal has been applied in many medical fields including but not limited to

neurology [127, 153], cardiology [62, 89], Urology [130, 158], pulmonary medicine [58, 37] and abdominal [34, 132] (see Figure 1.1) amongst others.

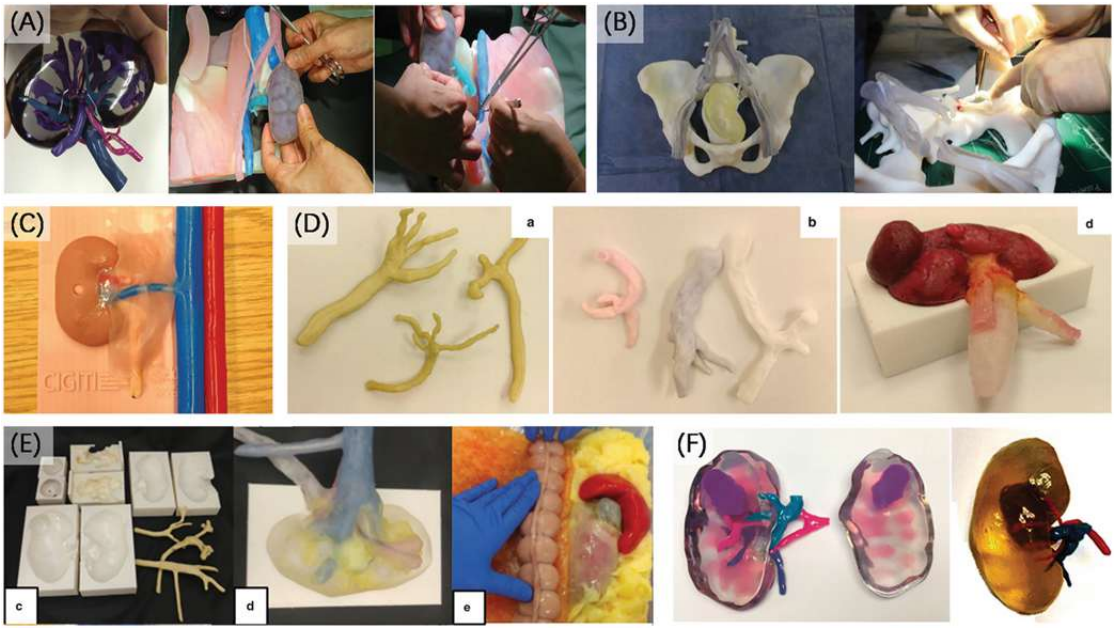

Figure 1.1: 3D printed models of liver organs [66]. Reproduced under terms of the Creative Commons CC-BY license.

In summary, it can be said that anatomical models are becoming increasingly important for surgical practice, especially models with realistic tactile feedback are desired and lead to a considerable improvement. Therefore, the creation, characterisation and modification of anatomical models with specific, tunable mechanical properties is cumbersome. Also the ability to specifically tune elastic, viscoelastic and fracture behaviour of tissue mimicking materials towards a specific tissue is lacking.

1.2 Goals and Objectives

The main aim of the dissertation is to develop 3D printable tissue mimicking materials with tunable elastic, viscoelastic and fracture toughness responses similar to that of specific soft biological tissues. Hereby an objective characterisation of the mechanical properties of selected soft tissues based on experimental testing and constitutive material modeling. The research objectives are divided into 3 main steps

- Characterisation of viscoelastic material response of soft biological tissues
- Characterisation of fracture toughness response with respect to viscoelastic properties of soft biological tissue

- Development of 3D printed tunable tissue mimicking materials for anatomical models

1.3 Materials and Methosds

1.3.1 Mechanical Properties of Soft Tissue

Soft tissue is often made up of several cell types embedded in extracellular matrix with diverse proteins that are able to store large quantities of water. The primary structures in soft tissues are elastin and collagen. While elastin is an elastic protein capable of 100% extension with little dissipation, collagen is a very tough material with a helical structure than can undergo large displacements until straightened. Currently there is a large amount of literature regarding the determination of tissue deformation behavior of biological soft tissue. Soft tissues have been shown to exhibit linear behaviour under some limited conditions (low strain) as well as non linear and anisotropic behavior under other conditions. Soft tissues also undergo creep or stress relaxation under constant load or strain respectively [73]. Therefore, it is necessary to determine the specific conditions of interest. In this study, the emphasis is laid on the mechanics of soft tissue during surgical procedures involving large deformation and fracture behaviour. Soft tissue in this regards has been shown to be non-linear and viscoelastic [47].

The determination of elastic, viscous and fracture material properties is essential in understanding the behaviour of soft tissue under various surgical conditions. Elastic properties of soft tissues are often determined by standard uniaxial tensile or compression tests (see Figure 1.2). The viscous property of solid materials, i.e.the ability of a material to inherently dissipate applied energy, is often tested by means of stress relaxation, creep tests or dynamic mechanical analysis (DMA) in tension or compression.

Tissue behavior during suturing and dissection involve the separation of tissues and therefore a propagation of defects in a material as seen from a mechanical point of view. An understanding of failure mechanisms in soft biological tissue is vital in assessing defects in a number of medical issues, such as iatrogenic rupture of fetal membranes during fetal surgery, raptures in skin or damage to tendons and ligaments during sporting activities or injuries [18]. This has been shown to be best represented by fracture mechanics [137]. is a branch of mechanics focused on understanding how cracks propagate in materials. It applies techniques from analytical solid mechanics to determine the forces acting on a crack and employs experimental solid mechanics to assess a material's resistance to breaking.. The behaviour of soft tissue materials during fracture is hypothesized to be dependent on tissue stiffness, viscoelasticity and material microstructure [9], [54], [107]. Various methodologies for determining fracture toughness have been proposed from fracture mechanics standpoint, these have implication For different tissues and soft materials each method has its advantages and disadvantages and must be chosen and analysed carefully to avoid erroneous results [162]. Specific tests to be used in this research project are specified in the Methodology section.

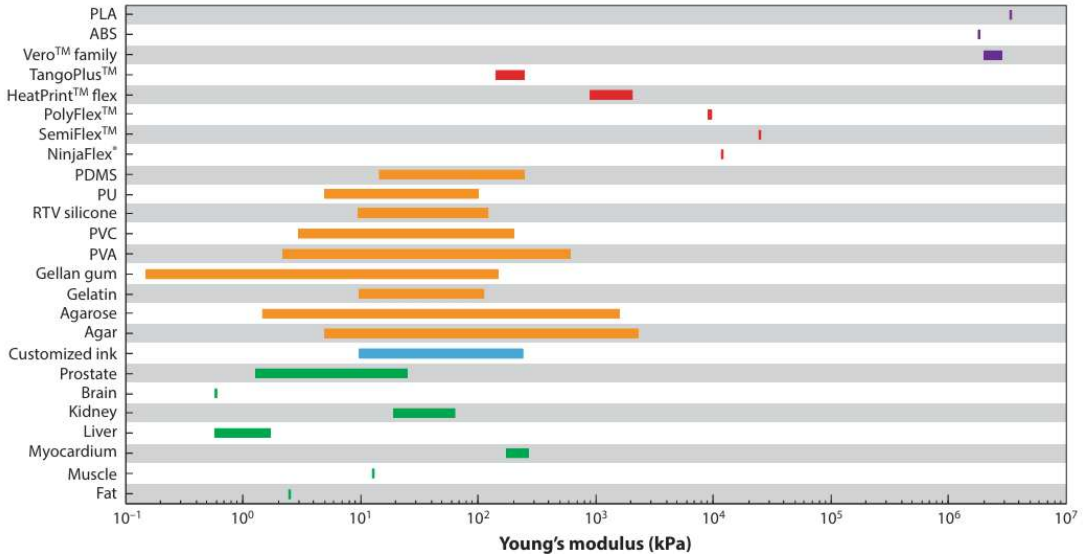

Figure 1.2: Young's modulus of common soft tissue and tissue mimicking materials [116].License number for reuse permission from publisher: 153546-1

1.3.2 Viscoelasticity

Most soft tissues in the human body consist mainly of water and hence exhibit both solid and fluid-like behaviour. This behaviour is described as viscoelasticity. Viscoelastic materials experience creep under constant applied stress, stress relaxation under constant applied strain or hysteresis effects under cyclic loading [67, 74, 11]. Furthermore, their response to dynamic loading is strain rate dependent [92, 11, 80]. Models describing soft tissue must therefore incorporate all these characteristics.

Typical stress strain curves of soft collagenous tissue and polymers is shown in Figure. 1.3. Three main ranges of strain for each curve are marked (I,II,III). Region I shows a range in which both soft tissues and polymers which can be approximated as being linear. A key feature of soft biological tissue is that at low strains ($< 3\%$) several tissues exhibit quasi-linearity [157, 80, 48]. Region II is the dynamic range which describes the typical working range of each of these materials and shows a high non-linear behaviour. The dynamic range for soft tissues is between 3% to 20% and polymers for polymers between 20% to 200% depending on the material [20]. Region III describes the typical failure strain ranges for these materials. An observable characteristic for soft tissue is the change from strain stiffening behaviour in the linear range to a strain softening behaviour in the dynamic range. This response is by virtue of the presence of stiff wavy collagen fibres which first straighten, stretch and then break. Polymers exhibit strain softening behaviour initially due to primary creep followed by strain stiffening behaviour towards failure [155].

Early linear viscoelastic models such as differential type Maxwell, Kelvin and Voigt model and Integral-type models such as Boltzmans models developed to describe rubbers and

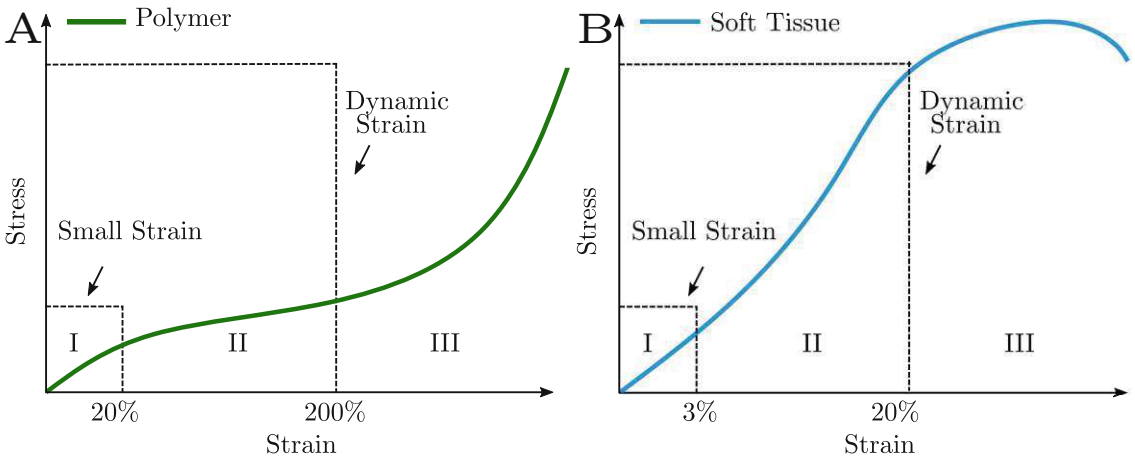

Figure 1.3: a) Typical stress strain curve of soft collagenous tissue showing strain softening behaviour and b)Typical stress strain curve of polymers showing strain stiffening behaviour. Regions of linearity (I), dynamic strain (II) and failure (III) are marked for each figure. Based on[155].

elastomers. Although linear viscoelastic models have often been applied to soft biological tissue with the constraint of small strain range, these are insufficient for use in soft tissue phantoms whose working range is often higher. Although linear viscoelastic models have often been applied to soft biological tissue with the constraint of small strain. A clear example is observed in the pre-operative assessment for a transcatheter aortic valve replacement (TAVR) for aortic stenosis. An assessment of the interaction between aorta, prosthesis and blood flow is critical. Since the maximum strain of the aorta is greater than 10%, the predicted mechanical responses from a linear viscoelastic model would differ significantly from the true response of the aorta.

Hence more advanced non-linear viscoelastic models had to be developed. A brief description of the most commonly applied linear and non-linear viscoelastic models is given in the next section. More detailed information can be found in [73, 47]

Linear Viscoelasticity

Maxwell model The simplest viscoelastic material model is the maxwell model consisting of a single spring and damper connected in series (see Figure.1.4). The series connection is referred to as a Maxwell element.

An applied Heaviside strain input (Figure. 1.5a) produces the same stress in both spring (σ_S) and damper (σ_D). Hence the total stress (σ) in the system is equal to the stress in each component.

$$\sigma = \sigma_D = \sigma_S \tag{1.1}$$

The total change in strain is the sum of the change in strain in the spring (ε_S) and the

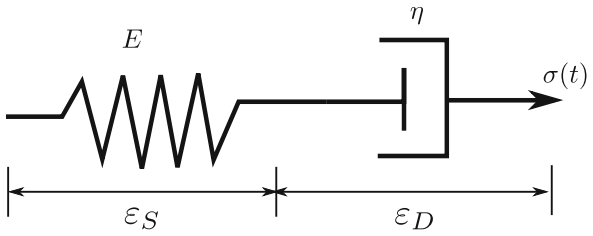

Figure 1.4: Maxwell element consisting of a spring with stiffness (E) and damper with damping coefficient (η) in series

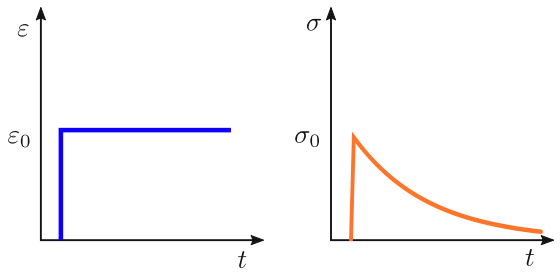

Figure 1.5: a)Heaviside strain ($\varepsilon(t)$) input function b)Stress response ($\sigma(t)$) of a Maxwell model to the Heaviside input strain

damper (ε_{D}). The resulting strain rate equation is given by :

$$\frac{d\varepsilon_{\mathrm{total}}}{dt} = \frac{d\varepsilon_{\mathrm{D}}}{dt} + \frac{d\varepsilon_{\mathrm{S}}}{dt} \tag{1.2}$$

The change in strain in the damper is related is time dependent and related to the damping coefficient (η) and in the linear spring only dependent on the elastic modulus (E), the equation becomes:

$$\frac{d\varepsilon_{\mathrm{total}}}{dt} = \frac{\sigma}{\eta} + \frac{1}{E}\frac{d\sigma}{dt} \tag{1.3}$$

For the applied Heaviside strain function, the initial strain (ε_0) is applied instantaneously, resulting in an instantaenous maximum stress (σ_0) (see Figure. 1.5), after which there is no change in strain and hence the change in strain with time is 0.

$$0 = \frac{\sigma}{\eta} + \frac{1}{E}\frac{d\sigma}{dt} \tag{1.4}$$

$$\frac{\sigma}{\eta} = -\frac{1}{E}\frac{d\sigma}{dt} \tag{1.5}$$

$$\frac{\sigma}{\eta} = -\frac{1}{E}\frac{d\sigma}{dt} \tag{1.6}$$

The stress response over time $\sigma(t)$ for a stress relaxation experiment will equate to:

$$-\frac{E}{\eta}dt = \frac{d\sigma}{\sigma} \tag{1.7}$$

$$\int -\frac{E}{\eta} dt = \int \frac{d\sigma}{\sigma} dt \tag{1.8}$$

The relaxation time (τ), which characterizes the rate of decay in the system. This represents the time it takes for the stress value to decay from σ_0 to σ_0/e. Hence only 37% of the initial stress will remain after time τ. It can be given as the ratio of the damping coefficient (η) to the Elastic modulus(E);

$$\tau = \frac{\eta}{E} \tag{1.9}$$

$$\int -\frac{1}{\tau} dt = ln(\sigma) + C \tag{1.10}$$

$$-\frac{t}{\tau} = ln(\sigma) + C \tag{1.11}$$

This simplifies Equation. 1.7 and the response of a maxwell element to a strain input at any given time :

$$\sigma(t) = \sigma_0 e^{-\frac{t}{\tau}} \tag{1.12}$$

where σ_0 is the initial instantaneous stress response to strain input.

The Voigt model This is a linear viscoelastic material model which can be described as the combination of a spring and dashpot in parallel. In this formulation the strain remains the same across both the dashpot and spring (see Fig. 1.6).This formulation is best suited for a creep experiment hence, for a creep experiment the total strain is calculated from the stress in each component.

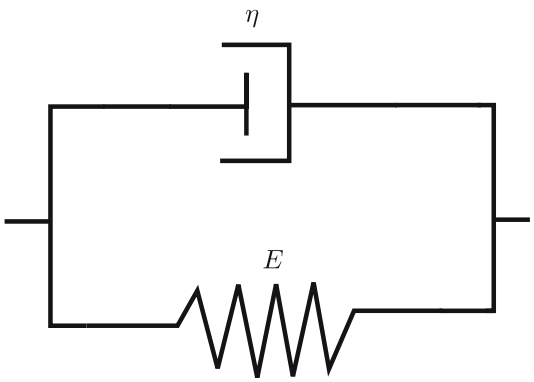

Figure 1.6: Voigt model consisting of a spring with stiffness (E) and a damper with coefficient(η) connected in parallel

.

Both spring and damper components will therefore experience the same strain

$$\varepsilon_{\text{total}} = \varepsilon_{\text{S}} = \varepsilon_{\text{D}} \tag{1.13}$$

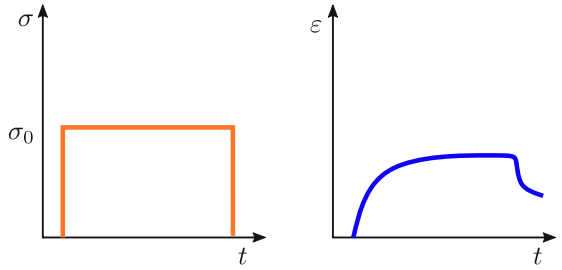

Figure 1.7: a) Rectangular stress input signal b) Strain response of a Voigt model to the rectangular input

.

The stress (σ_t) will be sum of the stress generated in each of the components by the given strain:

$$\sigma(t) = E\varepsilon(t) + \eta\frac{d\varepsilon(t)}{dt} \tag{1.14}$$

For a Voigt solid, a sudden application of load will produce no immediate deflection due to the presence of a damper in parallel. Hence the entire system will move at the rate of the damper. Voigt model is commonly used to model creep experiments hence for an applied unit rectangular stress signal (see Figure. 1.7a), the damper relaxes gradually allowing the spring to take a greater share of the load (see Figure.1.7b). The relaxation time (τ) is given similarly, as the ratio of damper coefficent (η) to spring stiffness (E). The strain response will be given by:

$$\varepsilon(t) = \frac{\sigma_0}{E}(1 - e^{-\frac{t}{\tau}}) \tag{1.15}$$

The SLS (Zener) model The Kelvin model also known as the Solid Linear Solid model, consists of a single spring in parallel with a maxwell element (see Fig. 1.8).

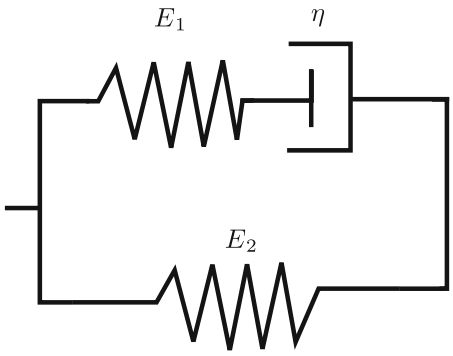

Figure 1.8: Standard Linear Solid model consisting of a maxwell element in parallel with a single spring

In this model the total stress σ_{total} in the system is the sum of the stress in the Maxwell element (σ_{m}) and in the parallel spring (σ_{S_1}). The applied strain is equal in each arm.

$$\begin{aligned} \sigma_{\text{total}} &= \sigma_{\text{m}} + \sigma_{\text{S}_1} \\ \varepsilon_{\text{total}} &= \varepsilon_{\text{m}} = \varepsilon_{\text{S}_1} \end{aligned} \tag{1.16}$$

For the maxwell element, the stress is equal in each component, while the strain is additive:

$$\begin{aligned} \sigma_{\text{m}} &= \sigma_{\text{D}} = \sigma_{\text{S}_2} \\ \varepsilon_{\text{m}} &= \varepsilon_{\text{D}} + \varepsilon_{\text{S}_2} \end{aligned} \tag{1.17}$$

Each stress component can be broken down into the following formulations:

$$\begin{aligned} \sigma_{\text{S}_1} &= E_1 \varepsilon_{\text{S}_1} \\ \sigma_{\text{S}_2} &= E_2 \varepsilon_{\text{S}_2} \\ \sigma_{\text{D}} &= \eta \frac{d\varepsilon}{dt} \end{aligned} \tag{1.18}$$

The governing equation for the maxwell element is given in Equation. 1.3.Implemeting Equation. 1.3 and Equation. 1.14 into time derivatives of the strain formulation of Equation. 1.17 gives :

$$\frac{d\varepsilon_{\text{total}}}{dt} = \frac{\frac{d\sigma_{\text{total}}}{dt} + \frac{E_2}{\eta}\left(\sigma_{\text{total}} - E_1 \varepsilon_{\text{S}_1}\right)}{E_1 + E_2} \tag{1.19}$$

Implementing these equations into the stress relation of Equation. 1.17 produces:

$$\sigma(t) + \frac{\eta}{E_2}\frac{d\sigma}{dt} = E_1 \varepsilon + \frac{\eta(E_1 + E_2)}{E_2}\frac{d\varepsilon}{dt} \tag{1.20}$$

The relaxation times are different for different materials; the relaxation time for constant strain (τ_ε) and the relaxation time for constant stress (τ_σ) are defined as follows:

$$\tau_\varepsilon = \frac{\eta}{E_2} \quad ; \quad \tau_\sigma = \frac{\eta}{E_1}\left(1 + \frac{E_1}{E_2}\right) \tag{1.21}$$

The stress response of the SLS model to a stress relaxation experiment i.e. to a Heaviside unit step strain input will be given by (see Figure. 1.9 :

$$\sigma(t) = E_1 \left[1 - \left(1 - \frac{\tau_\sigma}{\tau_\varepsilon}\right) e^{-t/\tau_\varepsilon}\right] \tag{1.22}$$

Although this model can be used to accurately predict the general shape of the strain curve, as well as behaviour for long time and instantaneous loads, the model lacks the ability to accurately model material systems numerically.

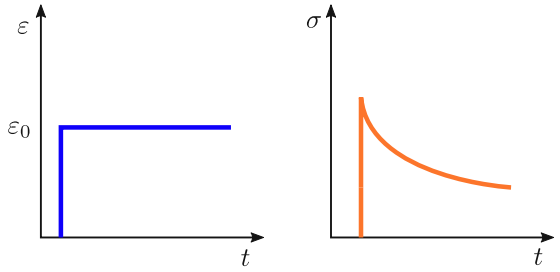

Figure 1.9: a)Heaviside strain ($\varepsilon(t)$) input function b)Stress response ($\sigma(t)$) of a Kelvin model to the Heaviside input strain

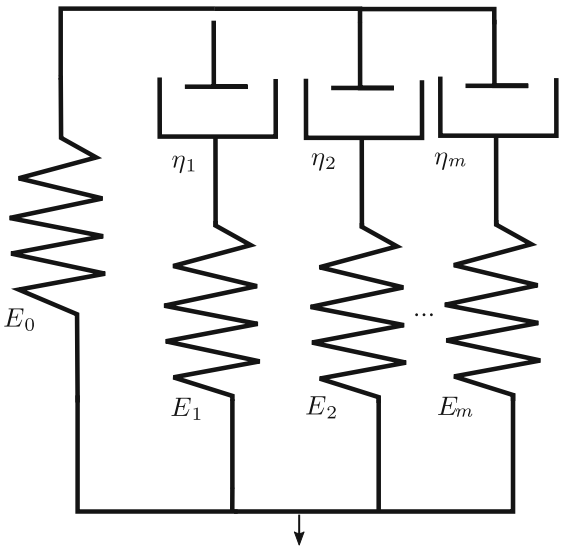

Figure 1.10: Generalized Maxwell model

Generalized Maxwell model The Generalized Maxwell model is the most generalized linear viscoelastic model. It consists of a parallel combination of maxwell elements (see Fig.1.10) and takes into account that the relaxation does not occur at a single time but in sets of times. It models the relaxation behaviour of linear viscoelastic materials with more freedom and hence more accuracy.

A stress relaxation for the Generalized Maxwell model is described by the summation of the stresses in the individual Maxwell elements. For each Maxwell element, the stress in each component is equal $\sigma_{\mathrm{D}} = \sigma_{\mathrm{S}}$, which follows that the strain in the component are additive:

$$\frac{d\varepsilon}{dt} = \frac{d\varepsilon_{\mathrm{S}}}{dt} + \frac{d\varepsilon_{\mathrm{D}}}{dt} \tag{1.23}$$

hence applied to all the maxwell elements, thechange in strain can be written as :

$$\frac{d\varepsilon}{dt} = \left(\frac{1}{E_i}\frac{d\sigma_i}{dt} + \frac{\sigma}{\eta_i}\right) \tag{1.24}$$

the total stresses will be the summation of the stresses in each maxwell element

$$\sigma = E_0\ \varepsilon + \sigma_1 + \sigma_2 + ... \tag{1.25}$$

Since the relaxation times are defined for the Maxwell elements as the ratio of damping coefficient to elastic modulus, this can be applied for all elements as

$$\tau_i = \frac{\eta_i}{E_i} \tag{1.26}$$

The Generalized Maxwell model can therefore be rewritten as follows:

$$\sigma(t) = \sum_{i=1}^{N} \sigma_i\ e^{-\frac{t}{\tau_i}} \tag{1.27}$$

Prony Series The Prony series is a commonly used formulation of a linear viscoelastic model. it is represented as a series of exponential functions. The relaxation times τ and relaxation coefficients are to be determined from the formulation

$$\sum_{i=1}^{N} = \alpha_i e^{\frac{-t}{\tau}} \tag{1.28}$$

where α_i are the coefficients of the exponential terms, N is the number of chosen elements. For a stress relaxation experiment, the model assumes an instantaneous unit step followed by a constant strain where the change in strain is 0 :

$$\sigma(t) = Y(t)\ \varepsilon \tag{1.29}$$

where $Y(t)$ is the relaxation function. The response under Prony Series can be described by :

$$Y(t) = E_0 \left(1 - \sum_{i=1}^{N}\ p_i\ (1 - e^{\frac{-t}{\tau}}\right) \tag{1.30}$$

where E_0 is the instantaneous modulus. p_i is the ith term of the Prony series; τ_i is the Prony relaxation time.

$$t = 0, \qquad Y(0) = E_0 \tag{1.31}$$

$$t = \infty, \qquad Y(\infty) = E_\infty \left(1 - \sum p_i\right) \tag{1.32}$$

where E_∞ is the long term modulus. The stress at any time in the system can be described by :

where E_0 is the instantaneous modulus, τ_i is the Prony relaxation time constant, p_i is the Prony constant.

Limitations Linear viscoelastic models are based on Boltzmanns Superposition Principle. The principle dictates that stress or strain responses to successive stimuli are additive. Hence the stress response to 2 successive strain stimuli $\Delta\varepsilon_1 + \Delta\varepsilon_2$ will produce additive stress responses $\Delta\sigma_1 + \Delta\sigma_2$. This principle however does not hold for larger strains (>3 %) in most soft tissues [47]. Secondly linear viscoelastic models can be described in terms of a unit step relaxation function ($G(t)$), which is the stress response to a unit step strain:

$$G(t) = \frac{\sigma(t)}{\varepsilon_0} \tag{1.33}$$

A stress relaxation experiment can therefore be described for a linear viscoelastic model by :

$$\sigma(t) = \int_{-\infty}^{t} G(t-\tau)\frac{d\varepsilon(\tau)}{d\tau}d\tau \tag{1.34}$$

where $G(t-\tau)$ qualitativelly describes the diminishing effect of the strain state at a time τ before the current time t. Since the relationship between stress and strain ($G(t)$) for soft biological tissues is however non-linear, these models cannot be applied. To overcome the shortcomings of these models non-linear viscoelastic models were proposed.

Non-linear viscoelastic models

There are several elegant non-linear viscoelastic models available in literature. Some advanced solutions such as the non parametric Volterra series approximation [126], which requires a Gaussian white noise input signal which cannot be used for uniaxial tensile loading that produces only positive forces[120]. Another approach proposed by Pipkin and Roger [112] involves incremental stress relaxation steps and is calibrated with a series of integrands. This methodology is however very computationally expensive and lengthy. There are also parameteric approaches where a general structure is hypothesized and and optimiation algortihm is used to identify parameters that fit the model data. If the initial hypothesis is however, wrong, the model fails [105].

The Schapery's Single Integral model [128] is a phenomenological model that aims to fit experimental data with a single integral in which non linear effects are incorporated into the strain or stress measure. These models are however out of the scope of this report. Fung's QLV model is the most common non-linear viscoelastic model applied to soft biological tissues hence will be the focus of this section. The advantages, limitations of the QLV model will be assessed. Subsequent adaptations, the Generalized Fung model and the Adaptive Quasi-linear viscoelastic models will also be reviewed.

Fungs QLV model Fung's Quasi-Linear Viscoelastic(QLV) model determines a class of quasi-linearity that is appropriate for several biological tissues. The Fungs's model incorporates nonlinearity into the general form of the linear convolution integral (Equation. 1.34) by replacing the strain with a non-linear function of strain ($d\sigma^{(e)}(\varepsilon)$), hence 'quasi-linearity':

$$\sigma(t) = \int_{-\infty}^{t} g(t-\tau)\frac{d\sigma^{(e)}(\varepsilon)}{d\varepsilon}\frac{d\varepsilon(\tau)}{d\tau}d\tau \tag{1.35}$$

where g(t) is called a "reduced" relaxation function, which is the unit step function (Equation. 1.33) normalized by its initial value and σ^e is a function of strain known as the "elastic stress".

The relaxation function $g(t-\tau)$ represents the shape of the normalized unit step function and is commonly described as a sum of exponential terms :

$$g(t) = a_o + \sum_{i=1}^{M} a_i \; e^{-t/\tau_i} \tag{1.36}$$

where M is the number of exponential terms with a corresponding relaxation time (τ_i) and amplitude a_i. This can be associated as a series connection with a single spring (a_0). Equivalent would be a series connection of Kelvin models with non-linear springs (see Fig.1.11) with a single non-linear spring.

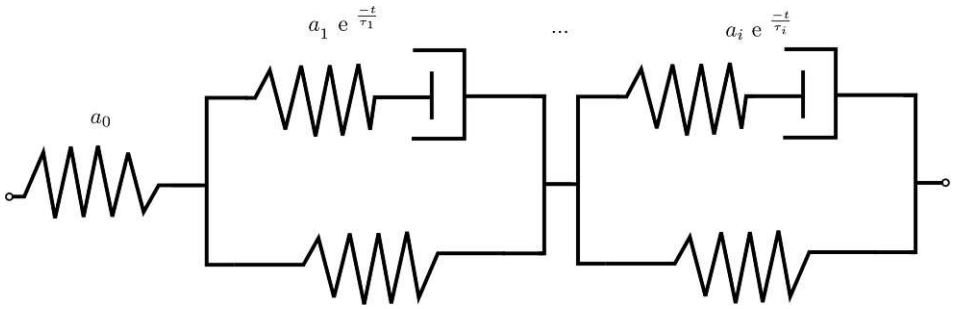

Figure 1.11: Fungs model schematic represented as a connection of spring damper systems in series with a single non-linear spring

The major limitation of the QLV model is the assumption of a single reduced relaxation function at all levels of strain. It has been observed that for varying strain amplitudes, the relaxation function also varies for a given biological tissue. This can be observed by plotting normalized relaxation functions of a given tissue at different strain amplitudes. Hence, once the QLV model is fitted to a given stretch and sequence, it is often unable to accurately describe the same material at other strain levels [114, 113]. This can be resolved by increasing the degrees of freedom of the model with respect to strain. Extensions of the QLV model have therefore been proposed such as the Generalized Fung model [114] and the Adaptive quasi-linear viscoelastic (AQLV) model[104, 103] which have been shown to fit model data well.

AQLV model The Adaptive quasi-linear viscoelastic model (AQLV) is a simplified approach to employing a strain dependence on the stress response to the existing QLV model. This is achieved by introducing an intermediate variable term known as the

viscoelastic strain $V^{(\varepsilon)}(t)$ and through the linear convolution integral as:

$$V^{(\varepsilon)}(t) = \int_{-\infty}^{t} g(t-\tau)\frac{d\varepsilon(\tau)}{d\tau}d\tau \tag{1.37}$$

where $g(t)$ is a reduced relaxation function that can be expressed as a sum of exponentials with different time constants (τ_i), as in Fung's model (see Equation. 1.36. $V^{(\varepsilon)}(t)$ represents the dependence of the stress on the history of straining. The stress response is given by a simple multiplication of the viscoelastic strain with a pure non linear function of strain $k(\varepsilon(t))$:

$$\sigma(t) = k(\varepsilon(t)) \quad V^{(\varepsilon)}(t) \tag{1.38}$$

k_ε introduces strain dependence and non-linearity into the model and converts the strain history (viscoelastic strain) into stress [103].

If shape functions are represented as exponential terms, the AQLV model can be represented in terms of parallel Maxwell elements with non-linear springs and dampers whose spring stiffnesses (k) and damper coefficients (b) are functions of the overall tissue strain (see Figure. 1.12).

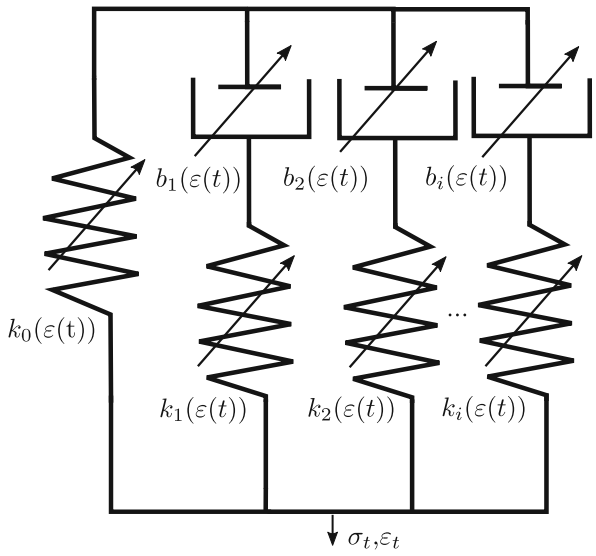

Figure 1.12: The AQLV model represented as a set of non-linear springs and dampers whose spring stiffnesses and damper coefficients are functions of the overall tissue strain

For the elastic response of the single spring, the stress is described simply by :

$$\sigma_0 = k_0(\varepsilon) = \sigma_0(\varepsilon) \tag{1.39}$$

For all the other non linear springs and dampers, each Maxwell element is required to be proportional to the same non-linear function of strain and hence the relaxation time

constant τ_i is independent of strain :

$$\tau_i(\varepsilon) = \frac{b_i(\varepsilon)}{k_i(\varepsilon)} = \frac{b_i}{k_i} = \tau_i \tag{1.40}$$

The total stress in the system implementing the viscoelastic strain term will be given as:

$$\sigma(t) = \sigma_0(t) + \sum_{i=1}^{M} k_i(\varepsilon(t)) V_i^{\epsilon}(t) \tag{1.41}$$

where M represents the number of Maxwell elements corresponding to each relaxation time and corresponding relaxation amplitude.

To calibrate the AQLV model, an incremental ramp and hold experiment (see Figure. 2.1) is required to determine the relaxation times (τ_i) and relaxation coefficients k_i and b_i.

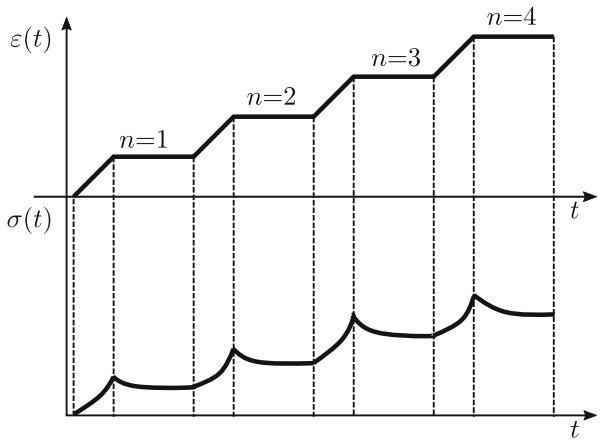

Figure 1.13: Incremental ramp and hold experiment for calibration of AQLV model

The strain function for n number of ramp and holds can be given as :

$$\varepsilon_n(t) = \begin{cases} (n-1)\Delta\varepsilon, & t < 0 \\ (n-1)\Delta\varepsilon + \frac{\Delta\varepsilon}{T}t, & 0 < t < T \\ n\Delta\varepsilon, & t > T \end{cases}$$

where T is the duration of of ramp loading in each increment, $\Delta\varepsilon$ is the equidistant strain increment for each step n. The hold (relaxation) stresses are used for the calibration of the model as there is no change in strain and strain rate is 0. The coefficient $k_i(\varepsilon)$ is no longer dependent on both strain and time but only on the strain at that hold level $n\varepsilon\Delta$. The general stress formulation can be rewritten:

$$\sigma_n(t) = \sigma_0(n\Delta\varepsilon) + \Delta\varepsilon \sum_{i=1}^{M} k_i(n\Delta\varepsilon)\ g_i(t) \tag{1.42}$$

where $\sigma_0(n\Delta\varepsilon)$ is the long term stress response. If exponential shape functions are chosen, the reduced relaxation functions for each element can be represented by :

$$\int_{-\infty}^{t} g_i(t)\ d\tau = \Delta\varepsilon g_i(t) = \tau_i\ (1 - e^{-t/\tau_i}) \tag{1.43}$$

The stress response recorded for the ramp phase during the experiments will be represented as R_n and for the hold phase as H_n. The model prediction for hold stress at each increment n is given by:

$$\sigma_H(t) = \sigma_0(\varepsilon(\Delta n)) + \frac{\Delta\varepsilon}{T} \sum_{i=1}^{M} \frac{\Delta\varepsilon}{T}\ k_i(n\Delta\varepsilon)\ (e^{-T/\tau_i})\ e^{-t/\tau_i} \tag{1.44}$$

Therefore the known shape functions $k_i(n\Delta\varepsilon)$ can be determined by minimizing the integral :

$$I_n = \int_{T}^{+\infty} (H_n(t) - \sigma_H(t))^2\, dt \tag{1.45}$$

The intermediate values of the functions of k_i can be determined by interpolation. Once the shape functions are calibrated, the values can be input into the model prediction for ramp stress, given by:

$$\sigma_{Rn}(t) = (\Delta\varepsilon(n-1) + \frac{\Delta\varepsilon}{T}t) + \frac{\Delta\varepsilon}{T} \sum_i k_i \left(\Delta\varepsilon(n-1) + \frac{\Delta\varepsilon}{T}t\right) g_i(t) \tag{1.46}$$

The major advantage of the AQLV model over Fungs QLV model is that it not only incorporates the strain dependent stress response of the tissue but also simplifies the computation of material parameters. There are however two limitations with the AQLV model. Although there is an ease of calibration, the model produces a high number of material parameters. It therefore requires an additional step Using the standard model as is, would produce at least 15 parameters, while a standard QLV model would produce 8 parameters.

1.3.3 Energy Storage and Dissipation

For interactions between soft tissues and surgical tools it is of interest to determine for a given mode of deformation the amount of energy stored and dissipated with and without interaction with a surgical tool. A characteristic of viscoelastic bodies is the ability of the material to dissipate heat through viscous losses during deformation with the rest of the energy being stored elastically. The net loss of energy over a complete cycle of deformation and recovery is known as hysteretic loss or hysteresis. Energy responses in a viscoelastic material are associated with lagging to loading by viscous dissipation. The total energy after a full cycle is composed of both the storage energy and the dissipated energy and is given by:

$$W_{\text{total}} = W_{\text{D}} + W_{\text{S}} \tag{1.47}$$

In a steady state cyclic deformation, the response to loading will return at the end of the cycle to the values they started with, hence there is no net energy stored in one full cycle of the deformation. Thus, the area enclosed by the hysteresis loop signifies the amount of energy dissipated per unit volume within the material during each cycle. The steady state is achieved after performing several cycles of the deformation, whereby the exact number is dependent on the material and loading parameters. In this research project, only steady state deformations will be considered. The net hysteresis energy during a complete cycle can be calculated is given by the following integral:

$$W = \int_0^t \sigma \, \mathrm{d}\varepsilon(t) = \int_0^t \sigma \, \dot{\varepsilon} \, \mathrm{d}t \tag{1.48}$$

This can be applied to all forms of steady state cyclic loading. In this section, the response of a viscoelastic material to harmonic and triangular wave excitations will be investigated.

Sinusoidal Wave excitation

This section will consider the response of a viscoelastic material to harmonic (sinusoidal) cyclic excitation. Given that a strain $\varepsilon(t)$ is applied to a sample as :

$$\varepsilon(t) = \varepsilon_0 \sin(\omega t) \tag{1.49}$$

The steady state stress response will be given by :

$$\sigma(t) = \sigma_0(\omega) \sin\left[\omega t + \theta(\omega)\right] \tag{1.50}$$

where σ_0 and ε_0 are the amplitudes of the harmonic wave;ω is the angular frequency and θ is the phase shift between the two signals.Some useful relations of stress and strain with the loss and storage moduli are given here:

$$\sigma(\omega)\cos\left(\theta(\omega)\right) = \varepsilon_0\ G'(\omega) \tag{1.51}$$

$$\sigma(\omega)\sin\left(\theta(\omega)\right) = \varepsilon_0\ G''(\omega) \tag{1.52}$$

$$\tan\left(\theta(\omega)\right) = \frac{G''(\omega)}{G'(\omega)} \tag{1.53}$$

where $G'(\omega)$ and $G''(\omega)$ refer to the storage and loss modulus respectively. The storage modulus is proportional to the average energy stored per unit volume of the material whiles the loss modulus is proportional to the dissipated energy.

$$W_{\text{loop}} = \oint \sigma(t)\mathrm{d}\varepsilon(t) = \omega\ \varepsilon_0\ \sigma_0(\omega)\ \int_0^{\frac{2\pi}{\omega}} \cos(\omega t)\sin\left[\omega t + \theta(\omega)\right]\mathrm{d}t \tag{1.54}$$

hence the energy absorbed over a full cycle given by the contour integral in Equation. 1.48 will be:

$$W_{\text{loop}} = \pi\ \varepsilon_0\ \sigma_0 \sin\left(\theta(\omega)\right) = \pi\varepsilon_0^2\ G''(\omega) \tag{1.55}$$

This relation shows that in a harmonic excitation the net energy dissipated over a cycle is also the net energy absorbed by the material over a cycle of deformation and there is no net stored energy. This applies only to steady state deformations. Figure. 1.14a shows the normalized stress and strain as a function of time. Figure. 1.14b shows stress as a function of strain for a half cycle steady state harmonic excitation with the resulting half ellipse having a phase shift of $\theta(\omega)$=$\pi/6$. The half ellipse represents half the hysteresis loop of a harmonic excitation.

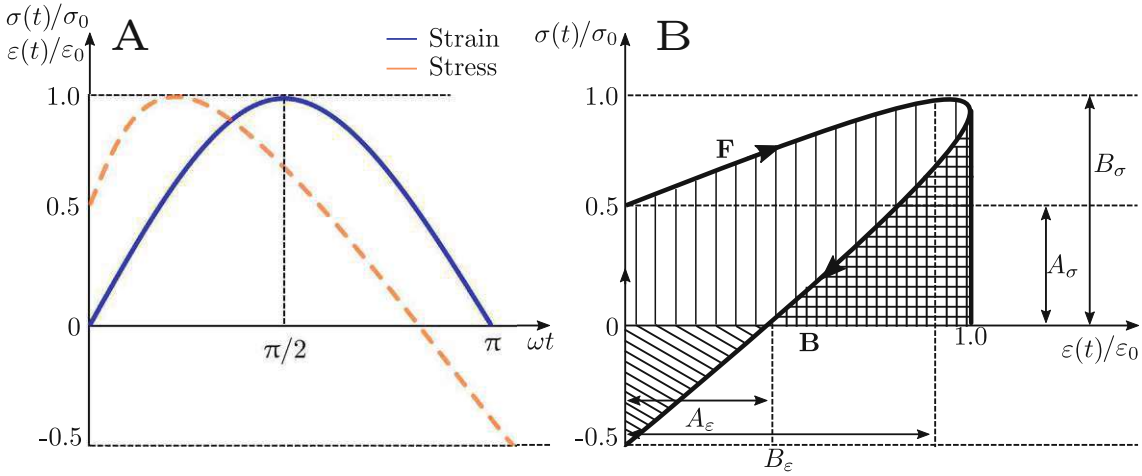

Figure 1.14: a) The normalized stress-time, strain-time curves are shown for a half cycle harmonic excitation. b) The stress-strain curve of the harmonic excitation showing a half ellipse

An analysis of Figure. 1.14 produces the following relations:

$$A_\sigma = \frac{\sigma(t)\ |_{\varepsilon(t)=0}}{\sigma_0(\omega)} = \sin\left(\theta(\omega)\right) \tag{1.56}$$

$$B_\sigma = \frac{\sigma(t)|_{\varepsilon(t)=\varepsilon_0}}{\sigma_0(\omega)} = \cos\left(\theta(\omega)\right) \tag{1.57}$$

$$\frac{A_\sigma}{B_\sigma} = \frac{\sigma(t)|_{\varepsilon(t)=0}}{\sigma(t)|_{\varepsilon(t)=\varepsilon_0}} = \tan\left(\theta(\omega)\right) \tag{1.58}$$

$$A_\varepsilon = \frac{\varepsilon(t)|_{\sigma(t)=0}}{\varepsilon_0} = \sin\left(\theta(\omega)\right) \tag{1.59}$$

$$B_\varepsilon = \frac{\varepsilon(t)|_{\sigma(t)=\sigma_0(\omega)}}{\varepsilon_0} = \cos\left(\theta(\omega)\right) \tag{1.60}$$

$$A_\varepsilon/B_\varepsilon = \frac{\varepsilon(t)|_{\sigma(t)=0}}{\varepsilon(t)|_{\sigma(t)=\sigma_0(\omega)}} = \tan\left(\theta(\omega)\right) \tag{1.61}$$

These relations enable the loss tangent ($\tan(\theta)$) to be determined. The loss tangent is the ratio of the loss modulus to the storage modulus and describes the phase lag between the stress and strain during a harmonic excitation.

To determine hysteretic energy the symmetry of the ellipse in Figure.1.14b, the half-loop is examined. It consists of two main sections denoted **F** and **B**. The section denoted **F** is the forward section during which the strain increases from zero to its maximum amplitude. The section denoted B is the backward section during which the strain again decreases to zero. The stress axis (marked with an arrow)is a fictive path along which the stress would be returned from $-\sigma_o \sin(\theta(\omega))$ to $+\sigma_o \sin(\theta(\omega))$ at zero strain. Since the strain is zero, no energy would be absorbed along this section.

The sum of dissipated and stored energy along the forward path (F)(quarter cycle) is represented by the area hatched vertically in Fig.1.14b and is given as:

$$\begin{aligned} W(\omega)_{\mathrm{F}} = \omega\ \varepsilon_0\ \sigma_0(\omega) \int_0^{\pi/2\omega} \cos(\omega t)\sin[\omega t + \theta(\omega)]\mathrm{d}t \\ = \left(\frac{\varepsilon_0^2}{2}\right)\left[\frac{\pi}{2}\ \mathrm{G}''(\omega) + \mathrm{G}'(\omega)\right] \end{aligned} \tag{1.62}$$

The energy stored and dissipated in the forward section can be obtained by the differentiation of the power rate of energy with time [144] and results in the stored energy and dissipated energy in the forward section to be :

$$W_{\mathrm{S}}(\omega)_{\mathrm{F}} = \left(\frac{\varepsilon_0^2}{2}\right)\left(G'(\omega) - \frac{\mathrm{d}\ G'(\omega)}{\mathrm{d}\ln\ \omega}\right) \tag{1.63}$$

$$W_{\mathrm{D}}(\omega)_{\mathrm{F}} = \left(\frac{\varepsilon_0^2}{2}\right)\left(\frac{\pi}{2}\ G''(\omega) + \frac{\mathrm{d}G'(\omega)}{\mathrm{d}\ln\ \omega}\right) \tag{1.64}$$

The total energy stored and dissipated along the backward section is obtained by integrating between the limits of $t_1 = \pi/2\omega$ and $t_2 = \pi/\omega$ which consists of the areas hatched diagonally and cross hatched.

$$\begin{aligned} W(\omega)_{\mathrm{B}} &= \omega\ \varepsilon_0\ \sigma_0(\omega) \int_{\pi/2\omega}^{\pi/\omega} \cos\left(\omega t\right) \sin\left[\omega t - \theta(\omega)\right] \mathrm{d}t \\ &= \left(\frac{\varepsilon_0^2}{2}\right)\left[\frac{\pi}{2}\ \mathrm{G}''(\omega) - \mathrm{G}'(\omega)\right] \end{aligned} \tag{1.65}$$

The storage and dissipated energies can be obtained in the same manner:

$$W_{\mathrm{S}}(\omega)_{\mathrm{B}} = -\left(\frac{\varepsilon_0^2}{2}\right)\left(G'(\omega) - \frac{\mathrm{d}G'(\omega)}{\mathrm{d}\ln\ \omega}\right) \tag{1.66}$$

$$W_{\mathrm{D}}(\omega)_{\mathrm{B}} = \left(\frac{\varepsilon_0^2}{2}\right)\left(\frac{\pi}{2}\ G''(\omega) - \frac{\mathrm{d}G'(\omega)}{\mathrm{d}\ln\ \omega}\right) \tag{1.67}$$

Energy stored during the first quarter is completely released during the second quarter, however because the storage modulus is monotone non-decreasing i.e less energy is dissipated in the backward section than in the forward. Putting the dissipated energy from both sections together gives:

$$\begin{aligned} W_{\mathrm{D}} &= W_{\mathrm{D}}(\omega)_{\mathrm{F}} + W_{\mathrm{D}}(\omega)_{\mathrm{B}} \\ &= \pi\ \varepsilon_0^2\ G''(\omega) \end{aligned} \tag{1.68}$$

This represents the area of the complete ellipse. Hence the hysteresis area (entire ellipse) for a harmonic strain excitation represents the total dissipated energy. The total storage energy in the same vein can be calculated by the following :

$$\begin{aligned} W_{\mathrm{S}} &= W_{\mathrm{S}}(\omega)_{\mathrm{F}} + W_{\mathrm{S}}(\omega)_{\mathrm{B}} \\ &= \frac{1}{2}\varepsilon_0^2\ G'(\omega) \end{aligned} \tag{1.69}$$

It can also be noted that the relative dissipation i.e. the ratio of the dissipated energy to the stored energy is given by

$$\frac{W_{\mathrm{D}}}{W_{\mathrm{S}}} = \frac{2\pi\ \varepsilon_0^2\ G''(\omega)}{\varepsilon_0^2\ G'(\omega)} \tag{1.70}$$

$$2\pi\ \ \tan\delta = \frac{W_{\mathrm{D}}}{W_{\mathrm{S}}} \tag{1.71}$$

Triangular Wave excitation

Energy absorption in response to a regular triangular strain excitation can also be examined. The stress strain and stress-strain-time curves for an steady state triangular wave excitation is shown in Figure. 1.15b. For an applied triangular wave strain defined as :

$$\varepsilon(t) = \begin{cases} \dot{\varepsilon}_0 t, & 0 \leq t \leq t' \\ -\dot{\varepsilon}_0 \left(t - 2t'\right), & t' \leq t \leq 2t' \\ 0, & t > 2t' \end{cases} \tag{1.72}$$

The stress response is given by :

$$\sigma = \begin{cases} \dot{\varepsilon}_0 \eta(t), & 0 \leq t \leq t' \\ \varepsilon_0 \left[\eta(t) - 2n\left(t - t'\right)\right], & t \leq t \leq 2t \\ \varepsilon_0 \left[n(t) - 2\eta\left(t - t'\right) + \eta\left(t - 2t'\right)\right], & t > 2t' \end{cases} \tag{1.73}$$

Assuming a unixial tensile loading with no pre-load, a steady state will be reached with the stress in a compressive state both at the beginning of the deformation half cycle and at the end of the recovery half cycle. The energy relations are derived a follows:

$$\sigma_{\text{load}}(\theta) = \dot{\varepsilon_0} \left[\{G_e\}\,\theta + \eta_{\{f\}} - 2\int_{-\infty}^{\infty} \tau G(\tau) \frac{\exp(-\theta/\tau)}{1 + \exp\left(-t'/\tau\right)} \mathrm{d}\ln\tau\right] \tag{1.74}$$

$$\sigma_{\text{unload}}(\theta) = -\dot{\varepsilon_0} \left[\{\mathrm{G_e}\}\left(\theta - 2t'\right) + \eta_{\{\mathrm{f}\}} - 2\int_{-\infty}^{\infty} \tau\ \mathrm{G}(\tau) \frac{\exp\left[-\left(\theta - t'\right)/\tau\right]}{1 + \exp\left(-\mathrm{t}'/\tau\right)} \mathrm{d}\ln\tau\right] \tag{1.75}$$

where G_e is a discrete viscoelastic constants added to account for arrheodictic (steady state) behaviour $G_e = 10^6/1.001\ \mathrm{N/m^2}$, $\eta_{\mathrm{f}} = 5X10^6\ Ns/m^2$ refers to the steady state viscosity. θ is the steady state time.

$$W(\theta) = \int_{\theta_1}^{\theta_2} \sigma(\theta)\dot{\varepsilon}(\theta) d\theta \tag{1.76}$$

integrating from 0 to t' and from t' to $2t'$

$$W\left(t'\right)_{\text{load}} = \left(\dot{\varepsilon}_0^2/\ 2\right)\left[\{G_e\}\,t'^2 + 2\ \eta_{\{f\}}t' - 4\int_{-\infty}^{\infty} \tau^2 H(\tau) \frac{1 - \exp\left(-t'/\tau\right)}{1 + \exp\left(-t'/\tau\right)} \mathrm{d}\ln\tau\right] \tag{1.77}$$

$$W\left(t'\right)_{\text{unload}} = \left(\dot{\varepsilon}_0^2/\ 2\right)\left[2\ \eta_{\{f\}}t' - \{G_e\}'^2 - 4\int_{-\infty}^{\infty} \tau^2 H(\tau) \frac{1 - \exp\left(-t'/\tau\right)}{1 + \exp\left(-t'/\tau\right)} \mathrm{d}\ln\tau\right]. \tag{1.78}$$

For a regular steady state excitation there is no net energy storage over a complete cycle hence, the energy of the hysteresis loop (see Figure.1.15a) is equal to the total dissipated

energy due to viscous losses. Thus, W_{diss} will be given as the difference between the energies for W_{load} and W_{unload} :

$$W\left(t'\right)\text{diss} = \left(\dot{\varepsilon}_0^2/2\right)\left[4\eta_{\{f\}}t' - 8\int_{-\infty}^{\infty}\tau^2 G(\tau)\frac{1-\exp\left(-t'/\tau\right)}{1+\exp\left(-t'/\tau\right)}\mathrm{d}\ln\tau\right] \tag{1.79}$$

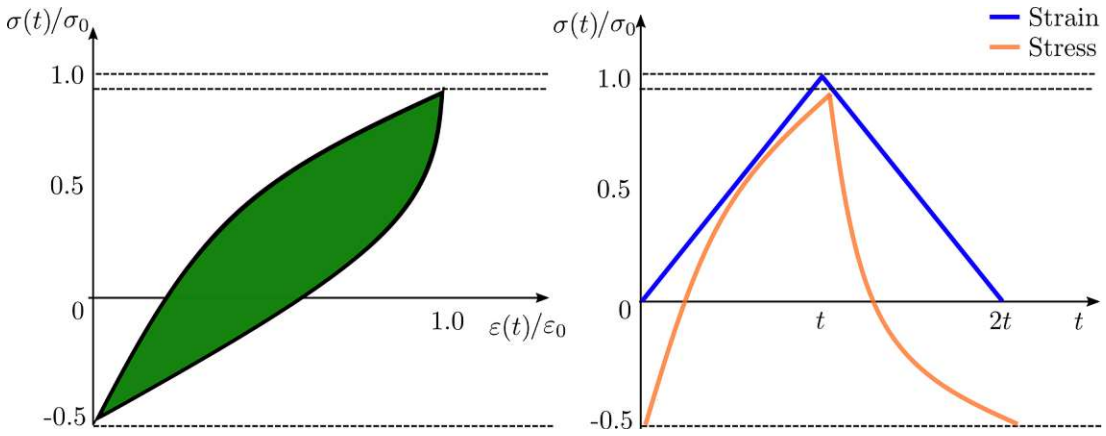

Figure 1.15: a) Stress response to a triangular wave strain excitation with hysteresis energy (green) b)Stress and strain as a function of time in triangular wave excitation

The hysteresis loop energy refers therefore to the total dissipated energy in a loading and unloading cycle, described by the area between the loading and unloading regions of stress as a function of strain, just as in a harmonic excitation [144].

1.3.4 Fracture Mechanics

Surgical procedures often involve the interaction of a surgical tool with a tissue. This interaction occurs with an exchange of energy that causes deformation or damage to the tissue. The most common surgical interactions have been modeled such as percutaenous (needle) insertion [2, 94, 71], sharp dissection [27, 28, 111, 85] and suturing [18, 110, 13, 14]. The damage to tissue during such interactions can be considered as a continuous crack propagation at the tools cutting edge. Furthermore, biological tissues have been shown to fail either mainly by cracking, such as bone fractures, or by tearing as in skin or cartilage. These processes can be represented as an exchange of energy between the tissue's internal strain energy and the irreversible work required to propagate a crack through the material. Generated damage leads to the creation of new surfaces occurring over time, thus, energy based methods will be the best representative models for such interactions[9]. This can best be described mechanically under fracture mechanics [137].

An important tissue specific parameter is the tissues specific resistance to fracture, referred to as fracture toughness or fracture resistance. Several authors have aimed at determining the tissue specific resistance to fracture for several biological tissues. In the following section, a short overview of the most important findings for fracture toughness of soft biological tissues is given. Furthermore, a clinically relevant procedure i.e. suturing will be assessed in the framework of fracture mechanics.

Fracture Toughness (J_c)

The ability of a material to resist crack propagation in the presence of a defect or its 'defect tolerance' has been denoted as fracture toughness, fracture resistance or tear resistance. The importance of the fracture toughness parameter is highlighted when materials with relatively high hardness and elastic modulus, such as glass or ceramics are observed to fail relatively quickly in the presence of a crack. In contrast to materials such as polymers, which have a relatively low elastic modulus and hardness but are able to absorb large amounts of energy before failure in the presence of defects. For ceramic materials, it is suggested to define a fracture toughness G_c or a critical stress intensity factor K_c, to better describe the failure in presence of defects. K_c describes the maximum stress required to cause failure by means of crack propagation. However, for polymeric materials and similarly for soft biological tissue the total energy that the material can absorb (i.e. the area under the stress strain curve) would be a better descriptor of toughness [139]. Therefore, in this project focus will be placed on the fracture toughness parameter defined in units of kJ/mm^2.

Fracture Toughness was defined by Griffith [1] in 1920 by the parameter G_c in which refers to the energy required to propagate a crack i.e. the energy per unit crack length formed. A typical fracture toughness experiment involves introducing a notch of length (a)into a material sample with thickness (B) fixated on both ends (see Figure. 1.16). A uniaxial tensile load is applied to the sample until crack propagation results in failure.

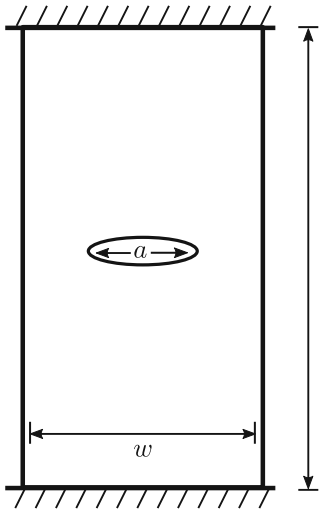

Figure 1.16: Sample geometry for fracture toughness testing of soft biological tissue with crack length (a) and sample width (w) and length (L_0)

The fracture toughness is calculated as:

$$G_c = \frac{1}{B}\frac{\Delta W}{\Delta a} \tag{1.80}$$

where the crack propagation energy (W) is calculated as the area under the load displacement curve for regions where a change in crack length was observed to grow. where W refers to the total energy in the body, B is the thickness of the sample and a is the crack length. G_c is usually applied to linear elastic materials, whereas it is defined as J_c for materials in which non-linearity is present due to plasticity or viscoelasticity.

Although the calculation of J_c is relatively simple, difficulty arises in defining experimental conditions. Taylor et al [140] determined the relation of failure stress to the initial crack length (see Figure. 1.17). Figure. 1.17 has three regions (I,II,III). In region I it is observed that for initial crack lengths under a critical length (a_0) the failure stress was equal to ultimate strength of the material and hence obtained fracture toughness parameter values were erroneous. The material is said to fail under strength control. In the second region, where the initial crack length is large enough to have an effect, certain corrections are required without which the J_c value is lower than the true value. The material is said to failed under mixed control in this region. For crack lengths sufficiently greater than the critical crack length (region III), failure is entirely determined by the fracture toughness and the ultimate strength can not be determined.

There are also several mechanisms that tend to absorb energy within a material such as multiple cracking, plasticity and viscoelasticity. These considerations are often not made when determining fracture toughness of a material. For soft biological tissues, the most dominant effect causing energy dissipation is assumed to be viscoelasticity. Oyen et al [109] proposed that the predicted J_c was less than the true value in soft biological

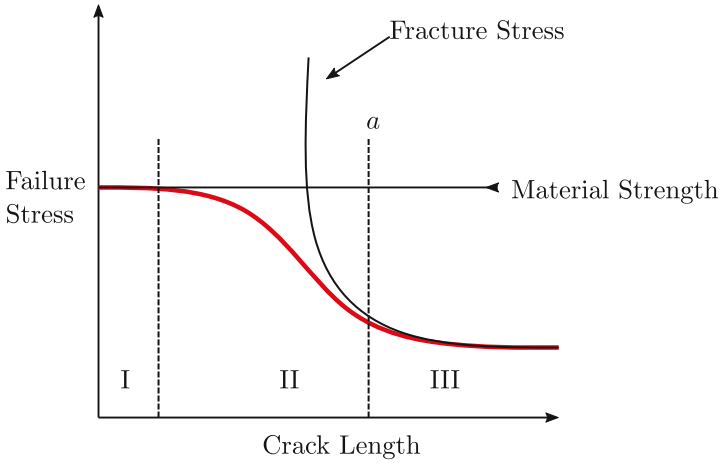

Figure 1.17: Effect of the initial crack length (a) on the measured fracture stress with regions I, II, III describing regions of strength control (I), mixed control (II) and toughness control (III) respectively [140]

tissues due to energy dissipation as a result of viscoelasticity. To determine the effect of viscoelasticity on the measured J_c, cyclic loading experiments on neocartilage were performed with and without notches. A dissipation energy ratio ($D(n)$) was determined and defined as the ratio of dissipated energy to total energy (U_T).

$$D(n) = U_D(n)/U_T(n) \tag{1.81}$$

where D(n) is the dissipated energy ratio per cycle number (n), U_D is the dissipated energy (hysteresis loop) and U_T the total energy applied to the sample. The working principle is that for an unnotched sample the total dissipated energy is due to viscous losses, however during crack propagation the dissipated energy is the sum of dissipated energy (U_D) and fracture energy (U_F). Hence J_c was defined

$$U_F = U_D(n) - U_T(n)\ D_0(n) \tag{1.82}$$

$$J_c(n) = \frac{U_F(n)}{[B\ \Delta a(n)]} \tag{1.83}$$

where D_0 is the dissipated energy ratio in the absence of a crack or the 'predictable viscous energy', B is the thickness and Δa is the change in crack length.

Suture Retention Test

Suturing is a common surgical procedure used for wound treatment to close cuts or during implantation to hold prosthesis to native tissue. The interaction between the suture and tissue is often assessed using tests aimed at measuring suture retention strength (SRS) and is popular in the cardiovascular grafting [110]. The AAMI/ISO/ANSI 7198 Standard (2016) defines suture retention strength or the anastomotic strength, as "the force needed to pull a suture from a prosthesis, or cause failure in a prosthesis". Hereby, a suture is classified sufficient if it is able to withstand a force of 2.0 N.

A typical suture retention test as described by the standard involves a rectangular shaped test specimen clamped on one edge with a suture material pulled through the a notch on the free edge (see Figure. 1.18). The notch is created with a suture needle and hence the notch size is dependent on the needle size. This is referred to as the suture bite. The suture bite depth is the distance from the free edge of the specimen (a_B) that shall amount to 2 mm as per the standard. The suture shall be tied off and pulled with a speed (v) of between 50-200 mm/min (ISO 7198, 2016). However, no specifications are given as to the type of suture and the bite size (needle size), thickness of the sample (d), specimen width (w) or the length of suture bite from the clamped edge L_0 (see Fig. 1.18).

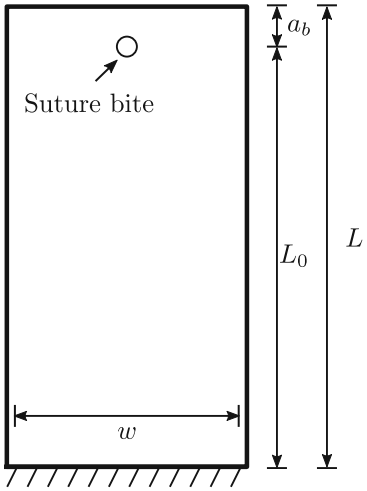

Figure 1.18: Sample geometry for the Suture Retention Strength (SRS) test with suture bite depth (a_b), sample length (L), distance to clamp (L_0) and width (w)

Each of these geometrical parameters have been shown to influence the outcome of SRS test. Several suture types with varying thickness of suture wire and needle sizes are available at different clinics and for different surgical applications. Several authors have investigated the effects of these geometrical parameters with the aim of standardizing test protocols. A study by Trostle et al [141] showed that the SRS increased logarithmically with suture bite size (needle size). Mine et al [93] showed a decreasing SRS force when thicker suture wires were used. They also proposed the existence of an early failure point

referred to as the breaking start strength (BSS) which depends only moderately on the sample thickness. Cooney et al [35] investigated the effect of the suture bite depth (a_B) and sample width (w) and observed that SRS values increased with increasing values of a_B and w. Pensalfini et al [110] suggested 'regions of trust' for geometrical parameters for the performance of suture retention strength test on soft biological tissue. They performed tests on bovine Glissons' capsule, porcine pericardium, human amnion as well as 4 types of Silicone, two Room temperature Vulcanizing (RTV) silicones and 2 Polydimethysiloxanes (PDMS) silicones, to determine both tearing energy and SRS and the effect of geometric and testing parameters.

A study of the geometric and testing conditions of the SRS test showed that both the bite depth (a_B) and specimen width only affect SRS whiles BSS remains relatively insensitive to them. The range of testing speeds (v) specified by the standard were tested and an increase of 25% in SRS and BSS was observed at faster pulling rates postulated to be related to the time dependent characteristics of the tissues tested. The distance of the suture bite depth from the clamped edge L_0 showed no significant impact on BSS. SRS however differed between the lowest and largest considered lengths. Investigation of the role of the sample thickness showed a proportional relation with the SRS.

Further results showed that failure always began before the peak catastrophic force, corresponding to the BSS force. The SRS/BSS ratio for soft biological tissues was between 1.5 and 4 and between 3 and 7 for silicones. The BSS for each material is shown to have a linear correlation with the tearing energy and is therefore hypothesied to be a fracture dominated metric. Considering BSS, the soft biological tissues are shown to be tougher than elastomeric materials. Considering SRS, elastomeric materials have stronger suture retention behaviour. In conclusion, a suture bite depth and specimen width of greater than 2 mm and greater than 10 mm respectively are sufficient for performing SRS tests, based on findings of Pensalfini et al [110]. The suture bite, suture material, loading speed and sample thickness should be recorded during testing to enable future comparisons.

1.4 Structure of Thesis

The main aim of the dissertation was to provide an objective means of characterizing both soft biological tissue as well as tissue mimicking materials in terms of mechanical properties of interest during surgical training and rehearsal. A short introduction to the current state of the art in anatomical models, the gap and motivation for the research, the main objectives, and summary of the scientific work was given first.

The following three original contributions form the core of the dissertation and were published in peer reviewed journals:

- **Chapter 2** - Based on self-published work [6] this research proposes the use of a reduced-parameter adaptive quasi-linear viscoelastic (AQLV) material model for the modeling of soft biological tissues at finite strain ranges. The research enables

an objective comparison of soft tissue material properties as well as reducing the experimental burden associated with viscoelastic characterisation.

- **Chapter 3** - Based on self-published work [7], this chapter describes the estimation of fracture toughness properties of soft biological tissues specifically porcine liver and porcine muscle tissue by the separation of strain level dependent viscous dissipated energy based on the AQLV material parameters. This research enables a better understanding of the constitutive viscoelastic and fracture behaviour of soft collagenous tissues.

- **Chapter 4** - Based on self published work [8], this chapter proposes a methodology to create tunable tissue mimicking tissues by introducing the concepts of microstructuring, fibre reinforcement and fluid infill into 3D printed polymeric material matrix in order to control non-linear elastic, viscoelastic and fracture behaviour. The research establishes techniques for refinement of 3D printed anatomic models towards improved surgical rehearsal.

The initial research goals, firstly to provide experimental methods and constitutive modeling approaches to objectively quantify the elastic, viscous and fracture responses of both soft biological tissues and tissue mimicking materials, were achieved in the initial two publications in Chapter 2 and Chapter 3. These served as a basis for comparison for developing 3D printed, tuned polymeric tissue mimicking materials shown in Chapter 4. The contribution to these works include but were not limited to the methodology, validation, software, investigation, formal analysis, visualization and original draft writing.

1.5 Summary of Publications and Contributions

The dissertation is based on the following publications. Publications I-III the author of the current dissertation is the first author and contributed to the methodology, software, validation, investigation, formal analysis, visualization and the writing of the original draft.

- I - Aryeetey OJ, Frank M, Lorenz A, Estermann SJ, Reisinger AG, Pahr DH. A parameter reduced adaptive quasi-linear viscoelastic model for soft biological tissue in uniaxial tension. J Mech Behav Biomed Mater. 2022;126:104999.

- II - Aryeetey OJ, Frank M, Lorenz A, Pahr DH. Fracture toughness determination of porcine muscle tissue based on AQLV model derived viscous dissipated energy. J Mech Behav Biomed Mater. 2022;135:105429.

- III - Aryeetey OJ, Jaksa L, Bittner-Frank M, Lorenz A, Pahr DH. Development of 3D printed tissue-mimicking materials: Combining fiber reinforcement and fluid content for improved surgical rehearsal. Materialia. 2024;34:102088.

In addition to the work presented in this dissertation, I contributed to the following publication (IV), which, although not included in the scope of this thesis, supported the overall research project and significantly informed the completion of my work. Here, I contributed as a second author to the methodology, formal analysis and writing review.

- IV - Jaksa L, Aryeetey OJ, Hatamikia S, Nägl K, Buschmann M, Pahr DH, Kronreif G, Lorenz A. 3D-printed multi-material liver model with simultaneous mechanical and radiological tissue-mimicking features for improved realism. Int J Bioprint. 2023;9(4):721.

1.6 Scientific Contribution

In this thesis, an important step towards the development of much more realistic anatomical models for surgical rehearsal has been applied by characterizing both soft biological tissue as well as tissue mimicking materials in terms of mechanical properties.

The complex nature of soft biological tissues has shown that there is a need to apply more flexible constitutive material models to better capture these complexities. However, the more flexible the constitutive model, the larger the number of material parameters required as well as the higher the number of experimental tests needed to calibrate the model. The application of the reduced parameter AQLV model enables a reduction in the number of experiments required as well as the number of material parameters whilst still maintaining a good accuracy with respect to experimental fitting. The reduced number of parameters also makes direct comparison between various tissues and materials easier.

In determining fracture toughness of soft biological tissues, it is necessary to account for the energy dissipated as a result of viscoelastic and plastic processes. The AQLV model parameters applied to the uniaxial tensile loading experiments based on previously calibrated material parameters showed a reasonable estimation of energy dissipation. The determination of fracture toughness based on these loss values were within reasonable range. It is hypothesized that other processes such as plasticity may account for slight discrepancies in the results as well. However the results show promising use of more flexible strain dependent constitutive models to help in determining fracture toughness of soft tissues which are paramount in surgical processes.

The proof of concept for the development of techniques to tune mechanical properties of polymeric materials showed that the reduction of material stiffness could be achieved by introducing a microstructure/infill in the polymeric matrix, essentially reducing the overall mass of material. The introduction of stiff wavy fibres analogous to collagen fibres in soft collagenous tissues, enabled the tuning of non-linear elastic response of the tissue mimicking materials. The novel concepts of introducing a viscous fluid to fill the internal cavities of the structure, fulfilled the goal of increasing the materials viscoelastic response as well. All in all the various applied techniques in this proof of concept can be applied to mimic various other soft tissues. This makes the approach more broadly applicable regardless of the type of 3D printer or polymeric ink being used.

CHAPTER 2

Paper 1

From manuscript:

A parameter reduced adaptive quasi-linear viscoelastic model for soft biological tissue in uniaxial tension

Othniel J. Aryeetey, Martin Frank, Andrea Lorenz , Sarah-Jane Estermann
Andreas G. Reisinger, Dieter H. Pahr

Published: J. Mech. Behav. Biomed.Mater. 10.1016/104999 December 2021

Abstract

Mechanical characterisation of soft viscous materials is essential for many applications including aerospace industries, material models for surgical simulation, and tissue mimicking materials for anatomical models. Constitutive material models are, therefore, necessary to describe soft biological tissues in physiologically relevant strain ranges. Hereby, the adaptive quasi-linear viscoelastic (AQLV) model enables accurate modelling of the strain-dependent non-linear viscoelastic behaviour of soft tissues with a high flexibility. However, the higher flexibility produces a large number of model parameters. In this study, porcine muscle and liver tissue samples were modelled in the framework of the originally published AQLV (3-layers of Maxwell elements) model using four incremental ramp-hold experiments in uniaxial tension. AQLV model parameters were reduced by decreasing model layers (M) as well as the number of experimental ramp-hold steps (N). Leave One out cross validation tests show that the original AQLV model ($3M4N$) with 19 parameters, accurately describes porcine muscle tissue with an average R^2 of 0.90 and

porcine liver tissue, R^2 of 0.86. Reducing the number of layers (N) in the model produced acceptable model fits for 1-layer (R^2 of 0.83) and 2-layer models (R^2 of 0.89) for porcine muscle tissue and 1-layer (R^2 of 0.84) and 2-layer model (R^2 of 0.85) for porcine liver tissue. Additionally, a 2 step ($2N$) ramp-hold experiment was performed on additional samples of porcine muscle tissue only to further reduce model parameters. Calibrated spring constant values for $2N$ ramp-hold tests parameters k_1 and k_2 had a 16.8% and 38.0% deviation from those calibrated for a 4 step ($4N$) ramp hold experiment. This enables further reduction of material parameters by means of step reduction, effectively reducing the number of parameters required to calibrate the AQLV model from 19 for a $3M4N$ model to 8 for a $2M2N$ model, with the added advantage of reducing the time per experiment by 50%. This study proposes a 'reduced-parameter' AQLV model ($2M2N$) for the modelling of soft biological tissues at finite strain ranges. Sequentially, the comparison of model parameters of soft tissues is easier and the experimental burden is reduced.

Keywords: Viscoelasticity, Quasi-linearParameter reduction, Soft tissue, Mechanical characterization

2.1 Introduction

The mechanical characterisation of soft viscous materials is essential in applications such as in the aerospace and automotive industry for sound damping [108], for anatomical models used in surgical training [117, 12, 123] and for medical diagnosis of diseased tissue [44, 131, 24]. However, this process can be difficult due to the non-linear, time-dependent behaviour of such materials, especially for soft biological tissue. Hence, complex material models with a large number of parameters are often required to model such material behaviour accurately.

The mechanical properties of different biological tissues vary over several orders of magnitude and are dependent on the strain level. For example, the initial tensile elastic moduli of human adipose tissue is ≈ 3kPa [56], porcine hepatic tissue [39] at 14 % strain ≈ 30kPa, and for leporine skeletal muscle [98] at 50% strain ≈ 450kPa. Moreover, there is also a high variability of mechanical properties of a specific tissue of a single species due to age, gender or disease [83]. Hence, it is necessary that constitutive models effectively capture these material characteristics to enable differentiation and comparison across different soft biological tissues.

Previous literature on the constitutive modelling has shown that soft biological tissues exhibit a quasi-linear behaviour i.e. a linear stress-strain behaviour at low strains and a non-linear behaviour at higher strains [80, 138, 48]. Several constitutive models can be applied, whereby Fungs' quasi-linear viscoelastic (QLV) model is the most common one[47]. The major advantage of the QLV model and its extensions are twofold. Firstly, it is a non-linear viscoelastic model describing the mechanical behaviour of soft tissues very accurately. Secondly, it enables modelling of both the non-linear elastic and linear viscoelastic behaviour of soft tissue, with a single set of parameters. In contrast, other

approaches implement a hyperelastic model to describe the non-linear elastic behaviour [48, 125, 151, 145], and a viscoelastic model to describe the viscous (relaxation or creep) response [40, 164, 21]. In the QLV a single set of parameters, which may be 8 or less, depending on the specific adaptation used [3, 68, 101], is sufficient for modelling the material behaviour of soft biological tissues.

A limitation of the QLV model is, however, the assumption of a single reduced relaxation function at all strain levels. Simply put, if the QLV model is fitted to experimental stresses at a specific strain level it would not accurately predict stresses at different strain levels. To overcome this shortcoming, some extensions of the QLV model with a higher flexibility were proposed, such as that of Pipkin & Rogers [112], the generalized Fung model by Pryse et al. [114], the attenuated non-linear viscoelastic model (ANLV) proposed by Quaia et al. [121] and the adaptive quasi-linear viscoelastic (AQLV) model proposed by Nekouzadeh et al. [104]. In general, the greater the flexibility of the model, the higher the number of parameters and computational expense required to fit the model to experimental data. Moreover, a large number of material parameters, makes comparison between various soft biological tissue as well as comparisons to polymeric tissue mimicking materials (TMMs), used in anatomical models, difficult and cumbersome. Hence a trade-off between accurate modelling and fewer parameters would be advantageous.

The AQLV model is a non-linear viscoelastic model with a greater flexibility to model strain dependent behaviour but still simple to calibrate, compared to other models. Its parameters are calibrated by fitting model parameters to the stress responses of incremental ramp and hold experiments simultaneously. Further, the AQLV model is able to describe with a single set of parameters both the ramp loading response and the relaxation behaviour of soft biological tissue with good material fits [103, 120]. The originally published model, however, produces a high number of model parameters (19) as it is modelled with 3 Maxwell layers ($M = 3$) over 4 incremental ramp-hold tests ($N = 4$). Due to its flexibility, the number of layers and incremental ramp-hold phases can be reduced. As a result, the number of material parameters, as well as the experimental burden (time per single experiment), is also reduced.

Generally, previous studies aimed to increase the modeling accuracy and capability of constitutive models, thereby increasing the complexity of such models. In contrast, the aim of the current work is, to investigate the effect of a reduction in the AQLV model parameters on model accuracy and fitting. Here, uniaxial tensile experiments are carried out on a reasonable number of porcine skeletal muscle (M. longissimus) and porcine liver tissue (8 per group) to determine the non-linear viscoelastic response of these tissues based on the AQLV model. Further, the accuracy of a reduced form of the original AQLV model is investigated by sequentially reducing the model layers (M) and number of ramp-hold tests (N). This is the first time to the authors knowledge that the AQLV model would be applied to model porcine skeletal muscle and liver tissue and that a parameter reduction study is carried out on the AQLV model. The reduced model parameters will enable future finite element simulation of these tissues, ease the comparison of tested tissues and reduce the experimental burden associated with the

calibration of a large number of tissue samples.

2.2 Methods

2.2.1 AQLV model theory

The AQLV model (originally described by Nekouzadeh et al. [104, 103]) is a constitutive model that relates stress σ to strain ε via a simple multiplication between the viscoelastic strain $V^{(\varepsilon)}(t)$ and a pure non-linear function of strain $k(\varepsilon(t))$. $V^{(\varepsilon)}(t)$ incorporates the relaxation function $g(t)$, which describes the diminishing effect of the strain history on the current level of stress. The AQLV model can be interpreted as M Maxwell elements in parallel with a single spring (see Figure 2.1A). In each layer i, $g_i(t)$ is chosen as a sum of exponential functions $g_i(t) = e^{-t/\tau_i}$ to represent the model in terms of parallel Maxwell elements, whereby the relaxation time τ_i is the ratio of the dashpot coefficient b_i to the spring constants k_i, ($\tau_i = \frac{b_i}{k_i}$).

$$\sigma(t) = k\Big(\varepsilon(t)\Big)\ V^{(\varepsilon)}(t) \tag{2.1}$$

$$V^{(\varepsilon)}(t) = \int_{-\infty}^{t} g(t-\tau)\frac{d\varepsilon(\tau)}{d\tau}d\tau \tag{2.2}$$

All the spring constants k_i and damper coefficients b_i are dependent on the overall tissue strain ε. For each Maxwell element i, a set of differential equations describes the stress and strain response:

$$\dot{V}_i + \frac{V_i}{\tau_i(\varepsilon)} = \dot{\varepsilon} \tag{2.3}$$

$$\sigma_i(t) = k_i(\varepsilon(t))\ V_i(t) \tag{2.4}$$

The relaxation times τ_i are therefore theoretically dependent on the overall tissue strain and not on the individual strains in each Maxwell element. A requirement of the model is that in each Maxwell element, both spring and damper elements should be proportional to the same non-linear function $\Psi_i(\varepsilon)$ of strain, since each element models a tissue-level strain-dependent relaxation mechanism. Hence the relaxation times τ_i are independent of strain:

$$\tau_i(\varepsilon) = \frac{b_i(\varepsilon)}{k_i(\varepsilon)} = \frac{b_i\Psi_i(\varepsilon)}{k_i\Psi_i(\varepsilon)} = \frac{b_i}{k_i} = \tau_i \tag{2.5}$$

Consequently, equation 3.11 and 3.12 become linear and their solution can be calculated in closed form from a linear convolution integral for a constant strain rate,

$$\dot{V}_i + \frac{V_i}{\tau_i(\varepsilon)} = \dot{\varepsilon} \rightarrow V_i(t) = \int_{-\infty}^{t} e^{-(t-\xi)/\tau_i}\frac{d\varepsilon(\xi)}{d\xi}d\xi \quad i = 1, 2, ...M \tag{2.6}$$

where M is the total number of parallel Maxwell elements. The total stress can be given as the following summation:

$$\sigma(t) = \sigma_0(\varepsilon(t)) + \sum_{i=1}^{M} k_i(\varepsilon(t))\ V_i(t) \tag{2.7}$$

The residual stress $\sigma_0(\varepsilon(t))$ for the fully relaxed model is a pure function of strain and is related to the spring constant of the single spring element $k_0(\varepsilon(t))$.

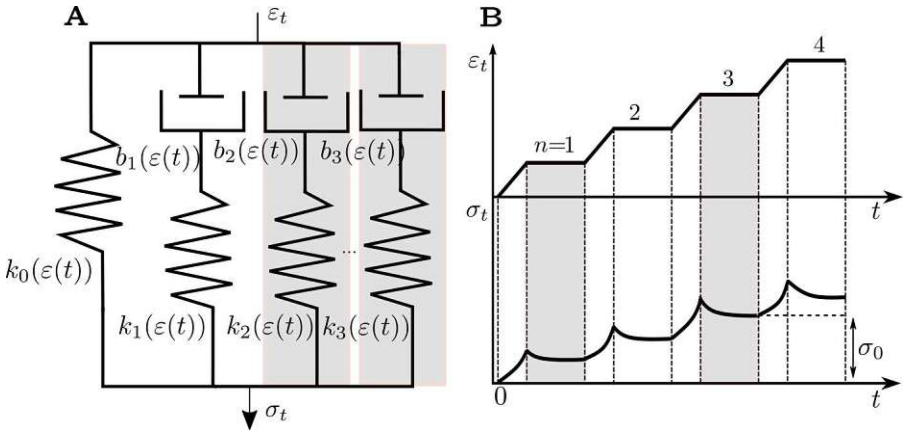

Figure 2.1: A) Maxwell element representation of the original AQLV model [103], showing the connection of non-linear springs k_i and dampers b_i. B) Strain-time inputs (top) and stress-time outputs (bottom) of a typical incremental ramp and hold experiment for the calibration of the original model with $N = 4$ levels. Highlighted (gray) are the elective Maxwell elements and ramp-hold steps that formulate the presented reduced models.

2.2.2 AQLV model calibration

The AQLV model is calibrated using an incremental ramp-hold protocol as seen in Figure 2.1B. This involves equidistant ramp stretches $\Delta\varepsilon$ over stretch time T at a constant strain rate $\frac{\Delta\varepsilon}{T} = const$, followed by hold phases for sufficiently long times, with $\dot{\varepsilon} = 0$ to allow relaxation of the sample to an equilibrium stress σ_0. To obtain the stress-strain relation, a strain function for the n^{th} ramp-hold test is given by :

$$\varepsilon_n(t) = \begin{cases} (n-1)\Delta\varepsilon, & t < 0 \\ (n-1)\Delta\varepsilon + \frac{\Delta\varepsilon}{T}t, & 0 < t < T \\ n\Delta\varepsilon, & t > T \end{cases} \tag{2.8}$$

and substituted into the equation for viscoelastic strain at each level $V_{i/n}^{(\varepsilon)}(t)$ (i^{th} Maxwell layer, n^{th} ramp-hold), represented for time phases between $0 < t < T$ given as:

$$V_{i/n}^{(\varepsilon)}(t) = \int_0^t g_i(t-\tau)\frac{\Delta\varepsilon}{T}d\tau = \frac{\Delta\varepsilon}{T}\gamma_i(t) \quad 0 < t < T \tag{2.9}$$

whereby $\gamma_i(t)$ is the integral of $g_i(t)$. For each n^{th} hold relaxation for time phases $t > T$, where T is the ramp time, the viscoelastic strain is given by:

$$V_{i/n}^{(\varepsilon)}(t) = \int_0^T g_i(t-\tau)\frac{\Delta\varepsilon}{T}d\tau = \frac{\Delta\varepsilon}{T}\Big(\gamma_i(t) - \gamma_i(t-T)\Big) \quad t > T \tag{2.10}$$

Incorporating equation 3.16 and 3.17 into equation 3.9 for the predicted stress $\sigma_{R/n}$ for ramp phases of the test gives:

$$\sigma_{R/n}(t) = \sigma_{0/n} + \frac{\Delta\varepsilon}{T}\sum_{i=1}^{M} k_{i/n}\ \gamma_i(t) \tag{2.11}$$

The predicted stresses for the hold phase of each n^{th} test is given by substituting equation 3.16 and 3.18 into equation 3.9:

$$\sigma_{H/n}(t) = \sigma_{0/n} + \frac{\Delta\varepsilon}{T}\sum_{i=1}^{M} k_{i/n}\Big(\gamma_i(t) - \gamma_i(t-T)\Big) \tag{2.12}$$

In the originally published model applied to neocartilage [103], the number of calibration steps (N) used was 4 and the number of model layers i.e. parallel Maxwell elements M was 3. The relaxation function represented as exponential shape functions can be given by:

$$g_1(t) = \tau_1\left(1 - e^{-t/\tau_1}\right),\ g_2(t) = \tau_2\left(1 - e^{-t/\tau_2}\right), \ldots \tag{2.13}$$

Substituting the shape functions into equation 3.18 gives the predicted hold phase stresses at each nth ramp-hold test as:

$$\sigma_{H/n}(t) = \sigma_{0/n} + \frac{\Delta\varepsilon}{T}\sum_{i=1}^{3} k_{i/n}\ \tau_i\left(e^{T/\tau_i} - 1\right)e^{-t/\tau_i} \tag{2.14}$$

Values for $\sigma_{0/n}$ and $k_{i/n}$ are obtained at each strain level (n). Values between obtained points are determined by means of a cubic spline interpolation as performed originally [103]. It is, however, possible to apply different interpolation functions such as a quadratic or exponential interpolation.

The values of τ_i and $k_{i/n}$ are calibrated using only the hold phase, whereby the integrals I_n are minimized, $\sigma_{H/n}(t)$ is the predicted hold stress, and $H_n(t)$ is the experimentally recorded relaxation stress:

$$I_n = \sum_n \int_T^{+\infty}\left(\frac{H_n(t) - \sigma_{H/n}(t)}{H_n(T)}\right)^2 dt \tag{2.15}$$

The fitted parameters are then implemented into equation 3.16 to predict ramp phase stresses. To account for non-linear strains in the ramp phase, experimentally obtained optical strains ($\varepsilon(t)$) might be implemented into the following adaptation of the equation 3.18 :

$$\sigma(\varepsilon, t) = \sigma_0(\varepsilon(t)) + \frac{\Delta\varepsilon}{T}\sum_{i=1}^{3} k_i(\varepsilon(t))\tau_i \mathrm{e}^{-t/\tau_i} \tag{2.16}$$

where k_i values have been implemented as a function, hence in the routine, $\sigma_0(\varepsilon(t))$ and $k_{i/n}(\varepsilon(t))$ are computed, in this case, from the cubic spline interpolation of $\sigma_{0/n}$, $k_{i/n}$ values, respectively.

2.2.3 Study Design

In the present study, the mechanical response of eight samples each, of porcine skeletal muscle and porcine liver tissue at (large) strains was modelled. Calibration was performed with experimental data of only the hold relaxation stresses at different strain steps $N = 4$ with three Maxwell elements (M=3) which describes the original (3-layer) model (see Figure 1). The calibration was implemented numerically in Python 3 based on the original available code and validated against previous data from Nekouzadeh et al. [103] and Smith et al [133]. Stresses in the ramp phase were then predicted using the obtained model parameters. The original Python functions were altered to implement parameter reduction techniques. To compare the quality of fit across the original and reduced models, the coefficient of determination (R^2) and the root mean square error (RMSE) were determined for each model (see section 2.4.3. for details). A leave one out cross validation (LOOCV) was performed for all samples to assess how well the model parameters of each AQLV model would predict future tissue samples. The process was performed for both porcine skeletal muscle and liver tissue.

2.2.4 Parameter reduction

Layer reduction

The originally published AQLV model [103] uses 3 parallel Maxwell elements and is, hence, referred to as the 3-layer model. Calibration of soft tissue material parameters in the framework of the original AQLV model with $M = 3$ layers and using $N = 4$ strain levels (experimental ramp-hold levels) would involve identification of $M = 3$ relaxation times (τ_i), $N \cdot M$ spring constants = 12 and $N = 4$ equilibrium stresses (σ_0). The number of total material model parameters L follows from

$$L = M + N \cdot M + N \tag{2.17}$$

resulting in $L = 19$ material model parameters. Here a 1- and 2-layer model ($M = 1$ and $M = 2$) and the usage of two or four strain levels (see Section 2.4.2) are further proposed. However, a decrease in accuracy of the model is expected with a reduction in the number of model parameters. The aim is to determine if reduced models could still reasonably model the viscoelastic behaviour of soft biological tissue similar to a AQLV model with three layers and four strain levels.

Reduction of strain levels

A further possibility of parameter reduction, as well as a means of reducing the experimental burden, is the reduction of the number of experimental steps (N) used for calibration (see Figure 2.1B). Conventionally, four strain levels are used to interpolate the behaviour of the residual stress and spring constants between zero and the maximal experimental strain. Here, we propose the use the calibrated values of the model parameters at two strain levels $N = 2$, instead of at all four strain levels ($N = 4$). Four additional muscle tissue samples were tested at 2 ramp-hold steps and k_1 and k_2 were obtained at those

2 strain levels (0.2 and 0.4 strain). A higher strain level was chosen to investigate how well the model predicts material behaviour close to the yield range of muscle tissue. However only values of k_1 and k_2 at 0.2 strain were compared to those obtained from a four ramp-hold ($N = 4$) experiment.

Average model parameters and fits

The material parameters ($\sigma_{0/n}, \tau_i, k_{i/n}$) of each model (3-,2-,1-layer) are obtained for each of the samples individually. The leave one out cross validation (LOOCV) is applied to the mean values of material parameters obtained.

The quality of model fits are compared using the coefficient of determination (R^2) and the root mean square error (RMSE). Hereby, R^2 and RMSE are determined for each tissue using the average of the 7 remaining tissue samples. Each R^2 and RMSE obtained from each individual prediction is measured and the mean of the values is reported. This describes how well a given set of material parameters would predict the next tissue sample.

Comparison to commonly used material properties

Although the AQLV model enables accurate modeling of soft biological tissue, it requires a large number of material parameters for calibration, which makes it cumbersome to compare. However, commonly used elastic and viscous parameters such as the instantaneous modulus ($E_0, \dot{\varepsilon} \to \infty$), long term modulus ($E_\infty,\ \dot{\varepsilon} \to 0$), storage modulus ($E'$), loss modulus ($E''$) and loss tangent ($tan\delta$) could be calculated based on the $k_{i/n}$ values at calibrated strain levels by the following equations, assuming linear viscoelasticity and small amplitude oscillations on top of an offset strain [55]. It is however noted that these values only represent approximations serve only to provide easier physical interpretation of AQLV model parameters and comparison to literature.

$$E'(\varepsilon(t)) = k_0(\varepsilon(t)) + \sum_{i=1}^{M} \frac{k_i(\varepsilon(t))\omega^2\tau_i^2}{1+\omega^2\tau_i^2} \tag{2.18}$$

$$E''(\varepsilon(t)) = \sum_{i=1}^{M} \frac{k_i(\varepsilon(t))\omega\tau_i}{1+\omega^2\tau_i^2} \tag{2.19}$$

whereby the angular frequency (ω) is assumed to be 1 Hz throughout the current study, for 1 mm/s loading rate. The loss tangent ($\tan\delta$) is the ratio of the loss to storage modulus and is computed as :

$$\tan\delta(\varepsilon(t)) = \frac{E"(\varepsilon(t))}{E'(\varepsilon(t)} \tag{2.20}$$

Long term modulus (E_∞) and instantaneous modulus (E_0) are calculated as :

$$E_\infty(\varepsilon(t)) = \sigma_0(\varepsilon(t)) \tag{2.21}$$

$$E_0 = \sigma_0(\varepsilon(t)) + \sum_{i=1}^{M} k_i(\varepsilon(t)) \tag{2.22}$$

2.2.5 Sample Preparation

Whole porcine skeletal muscle (M. logissimus) and liver organs were obtained fresh from a local abbattoir. Porcine skeletal muscle samples were directly sliced (see Figure 2.2A), whilst Glisson's capsule of porcine liver tissue was firstly excised, leaving parenchyma tissue only (see Figure 2.2B). Tissue was sliced into rectangular $75 \cdot 20 \cdot 5$ mm^3 ($L \cdot B \cdot T$) samples as described previously by Estermann et al. [40], for stress relaxation experiments. Specimens were stored in a physiological saline solution (9 g/l NaCl) at room temperature immediately after incision, until testing, to ensure hydration. A total of 12 porcine muscle (8 samples for $4N$ and 4 for $2N$ ramp-hold experiments) as well as 8 liver tissue specimens, were used for model calibration.

2.2.6 Mechanical testing

Experiments were performed with an electro-mechanical test machine (ZwickiLine Z2.5, Zwick Roell GmbH, Ulm, Germany) in combination with a 100 N load cell (S2M HBM, Freiburg, Germany) and a data acquisition system (QuantumX MX440B HBM, Freiburg, Germany) operated at 10 Hz (see Figure 2.2C). A high resolution camera (Sony α-6400, Sony, Tokyo, Japan) was used for optical video recording at 1 Hz.

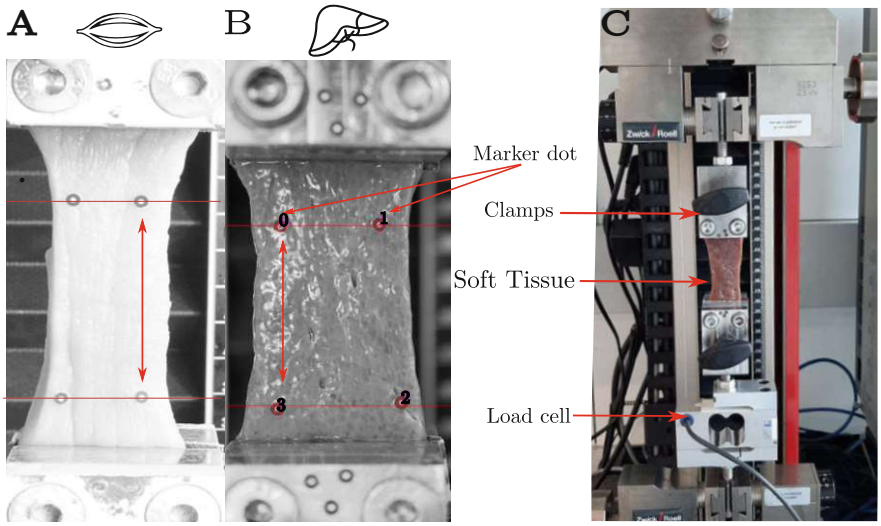

Figure 2.2: A) Porcine muscle tissue and B) porcine liver tissue samples with markers used for optical strain tracking. Lines indicate the average position of markers on top and bottom of the sample. C) Mechanical test setup for uniaxial tensile testing, the sample is fixed with clamps and connected to a 100 N load cell mounted in a electro-mechanical testing machine.

Incremental ramp and hold experiments were performed to calibrate the AQLV model, as described previously by Nekouzadeh et al. [104]. Samples were preconditioned directly

prior to experiments individually by clamping approximately 15 mm of one edge (top) and allowing to hang for a period of 300 s. In the meantime, white dot markers (GOM, Braunschweig, Germany) were placed slightly below the upper clamped region and above 15 mm from the bottom end to avoid bell ends and to ensure that the gauge area was vertical. These were used for strain tracking analysis with a point tracking algorithm described previously by Frank et al. [45] (see Figure 2.2A).

Effective gauge length was approximately 40 mm for both tissue types. Specimens were subsequently clamped on both edges. The tissues were pulled at a speed of 1 mm/s, as performed in the original study by Nekouzadeh et al [103] for four equal strain steps ($N = 4$). The exact strains were determined optically with the strain tracking algorithm. The loading rates were assumed to be adequately small that inertial effects are negligible. The hold phases were 1500 s; this was tested prior to allow the tissue to reach an equilibrium state. Samples were hydrated intermittently by means of spraying to prevent severe dehydration in final stages of testing.

2.2.7 Stress and strain determination

Actual sample strains were obtained via digital image correlation (DIC). Hereby, the position of the markers is tracked over time and the relative displacement between the marker positions at the top and bottom is determined. Hence, engineering strain is computed as :

$$\varepsilon(t) = \frac{l(t) - l_0}{l_0} \tag{2.23}$$

where l_0 is the initial length (at zero-force) and $l(t)$ the actual length of the tissue. The uniaxial linear engineering stress (σ) is calculated from the axial measured force (f) and the cross sectional area ($A_0 = B \cdot T$), measured with a caliper (prior to testing) and averaged at 3 positions, using the following equation:

$$\sigma(t) = \frac{f(t)}{A_0} \tag{2.24}$$

2.2.8 Statistical analysis

Model fits (R^2, RMSE) between each reduced model (1-, 2-layer) as well as results of step reduction for spring constant values k_1 and k_2 for step reduced models 2-layer models at 4 strain levels $2M4N$ and at 2 strain levels $2M2N$ were tested for statistical significance with respect to the 3-layer model using the Mann-Whitney U test for a significance level of $\alpha = 0.05$ implemented in Python 3.

2.3 Results

The mean experimentally determined stress curves with standard deviation for 8 porcine muscle tissue samples is shown in Figure 2.3A and for 8 porcine liver tissue is shown in

2.3B. A relatively high variation in tissue stresses is still observed in both tissue types, with an increasing deviation in stresses at higher strain levels.

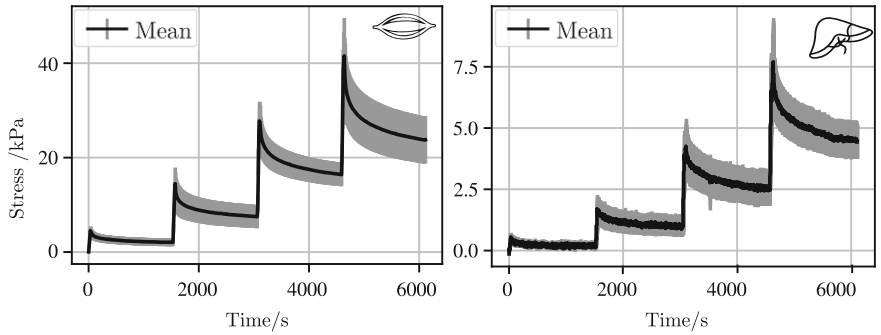

Figure 2.3: Mean stress-time results of incremental ramp-hold tests (black) with standard deviation (gray) of A) porcine longissiumus muscle and B) porcine liver tissue.

2.3.1 Comparison of AQLV models

Calibration of all model parameters was done for each sample individually for all samples to obtain material parameters ($\sigma_{0/n}$, $k_{i/n}$ and τ_i). R^2 and RMSE values from the Leave One Out cross validation (LOOCV) were calculated and tabulated for both porcine muscle and porcine liver tissue (see Table.1).

Muscle	3-Layer				2-layer			1-layer	
	τ_1/s	τ_2/s	τ_3/s		τ_1/s	τ_2/s		τ_1/s	
	10 ± 7	88 ± 54	840 ± 442		25 ± 7	411 ± 44		130 ± 18	
ε_n	σ_0/kPa	k_1/kPa	k_2/kPa	k_3/kPa	σ_0/kPa	k_1/kPa	k_2/kPa	σ_0/kPa	k_1/kPa
0.06	2.0 ± 1.5	220 ± 100	22 ± 7.2	10 ± 2.7	2.0 ± 1.0	241 ± 74	22 ± 6.0	2.0 ± 0.9	164 ± 38
0.13	8.0 ± 4.8	650 ± 310	76 ± 44	41 ± 14	7.0 ± 3.1	720 ± 210	66 ± 20	8.0 ± 4.0	430 ± 100
0.20	13 ± 5.0	1020 ± 390	120 ± 34	69 ± 16	13 ± 5.3	1230 ± 400	120 ± 30	14 ± 2.8	790 ± 170
0.26	20 ± 6.3	1570 ± 790	180 ± 38	95 ± 22	18 ± 7.3	1510 ± 380	143 ± 46	20 ± 8.6	850 ± 230
Metric	R^2	RMSE/kPa			R^2	RMSE/kPa		R^2	RMSE/kPa
Mean	**0.90 ± 0.13**	**3.24 ± 1.74**			**0.89 ± 0.15**	**2.52 ± 1.6**		**0.83 ± 0.08**	**2.61 ± 2.54**
Liver	τ_1/s	τ_2/s	τ_3/s		τ_1/s	τ_2/s		τ_1/s	
	8.7 ± 4.7	88 ± 74	750 ± 320		18 ± 6.8	460 ± 82		168 ± 24	
ε_n	σ_0/kPa	k_1/kPa	k_2/kPa	k_3/kPa	σ_0/kPa	k_1/kPa	k_2/kPa	σ_0/kPa	k_1/kPa
0.04	0.1 ± 0.05	48 ± 28	13 ± 5.5	3.3 ± 2.2	0.1 ± 0.05	18 ± 10	4.4 ± 2.7	0.1 ± 0.06	6.7 ± 5.1
0.08	0.8 ± 0.3	120 ± 69	24 ± 9.4	8.4 ± 4.1	0.8 ± 0.3	87 ± 57	13 ± 8.3	0.8 ± 0.3	32 ± 22
0.12	2.5 ± 0.6	210 ± 61	56 ± 40	25 ± 11	2.4 ± 0.6	190 ± 31	30 ± 11	2.6 ± 0.8	100 ± 84
0.16	4.4 ± 1.1	470 ± 150	110 ± 100	45 ± 17	4.4 ± 1.1	330 ± 80	57 ± 31	4.3 ± 1.5	220 ± 22
Metric	R^2	RMSE/kPa			R^2	RMSE/kPa		R^2	RMSE/kPa
Mean	**0.86 ± 0.10**	**0.28 ± 0.06**			**0.85 ± 0.07**	**0.29 ± 0.22**		**0.84 ± 0.01**	**0.35 ± 0.15**

Table 2.1: Mean ± standard deviations of time constants τ_i, residual stresses σ_0, spring constants k_i, for each strain level ε_n of AQLV models for porcine muscle and liver tissue.

The mean parameters σ_0, $k_i(\varepsilon)$ were fitted with a cubic spline interpolation, to obtain intermediate points and are illustrated for porcine muscle tissue in Figure 2.4.

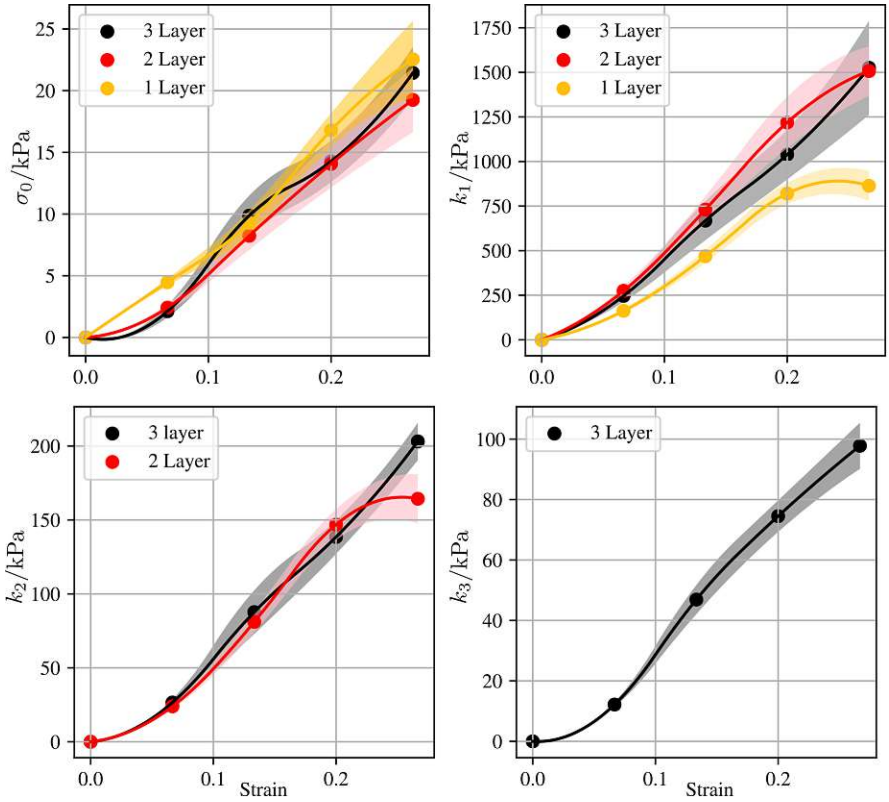

Figure 2.4: Mean ± confidence interval equilibrium stresses (σ_0) and spring constants (k_i) values shown as a function of global strain (ε) of AQLV models of porcine muscle. Dots represent calibrated average values connected by cubic spline interpolations. Shadowed regions represent the 95% CI. A similar representative image was obtained for porcine liver tissue (see Appendix).

A similar representative image was obtained for porcine liver tissue (see Appendix). For the LOOCV, a single representative porcine muscle tissue sample was chosen to show the predictive behaviour of a 1-layer (blue), 2-layer (red) and 3-layer (black) AQLV model with respect to experimental (gray) data (see Figure 2.4).

For porcine muscle tissue, it was observed, that the 3-layer and 2-layer model produced relatively close R^2 values (qualitative) fits, (0.90 ± 0.13 and 0.89 ±0.15 respectively), whereas the 1-layer showed a worse fit (0.83 ± 0.08). Quantitatively, the 3-layer model, however showed a slightly higher RMSE (3.24 ± 1.74) kPa compared to the 2-layer (2.52 ± 1.61) kPa and 1-layer (2.61 ± 2.54) kPa model. For porcine liver tissue, the 3-layer model showed better fits, albeit only slightly, both qualitatively (0.86 ± 0.10) and quantitatively (0.28 ± 0.06), as compared to the 2-layer (0.85 ± 0.07, 0.29 ± 0.22) and 1-layer (0.84 ± 0.01, 0.35 ± 0.15) AQLV models.

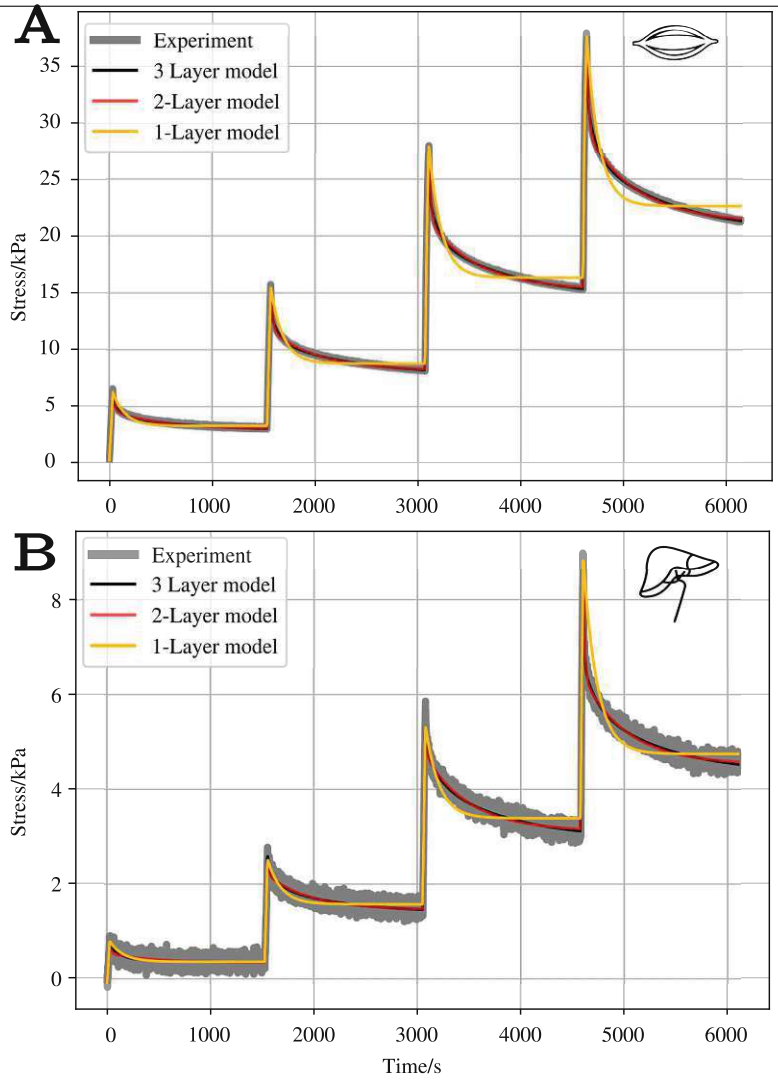

Figure 2.5: Representative plot demonstrating the predictive behaviour of 1-layer (blue), 2-layer (red) and 3-layer (black) AQLV models with respect to experimental (gray) data of a representative A) porcine muscle tissue and B) porcine liver tissue.

2.3.2 Reduction of strain levels

Four additional porcine muscle tissue samples were calibrated with a 2-layer AQLV model at a two step incremental ramp-hold test performed on 4 porcine muscle samples. A representative muscle tissue sample calibrated at 2 ramp-hold steps ($N = 2$) is shown in Figure 2.6.

Determined values of k_1 (1370 $\pm$ 310) kPa for a $2M2N$ AQLV model were within the range of measured values for muscle tissue calibrated at 4 strain levels ($N = 4$) for a 3-layer AQLV model (1020 $\pm$ 390) kPa and 2-layer model (1230 $\pm$ 400)kPa calibrated at 4 ramp-hold steps ($N = 4$). There was no significant difference between the values of each pair of calibrated k_1 values ($p = 0.22$) based on the Mann-Whitney U test. This

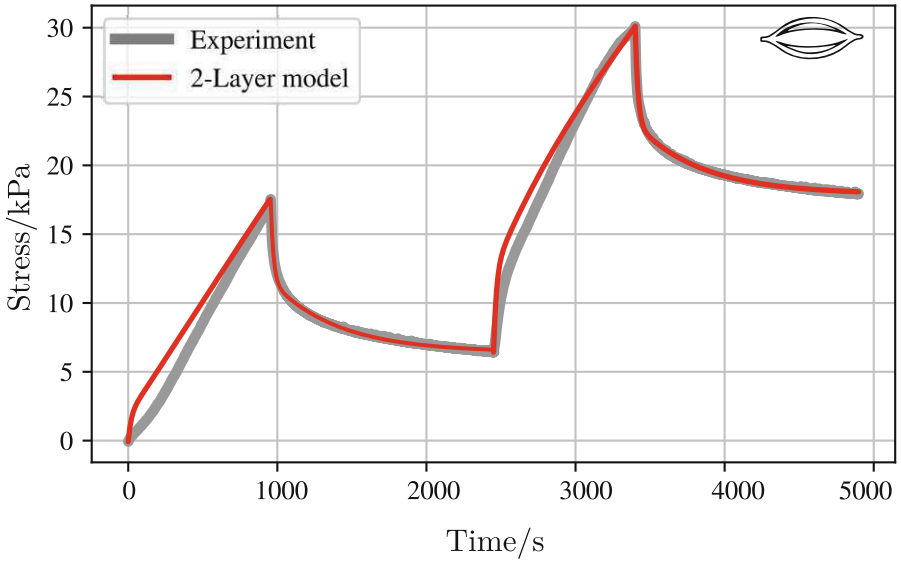

Figure 2.6: Predictive behaviour of a 2-layer AQLV model (red) calibrated at 2 ramp and hold ($2N$) levels with respect to experimental data (gray).

accounts for a maximum percentage deviation of $\approx 16.8\%$ for k_1. Values determined for k_2 (76 $\pm$ 17) kPa for a $2M2N$ AQLV model showed a higher maximum percentage deviation ($\approx 38\%$) as compared to k_2 determined 4 ramp hold steps for a 3-layer (120 $\pm$ 34) kPa and 2-layer (120 $\pm$ 30) kPa model. There was a significant difference for tests between each pair of calibrated k_2 values ($p = 0.006$).

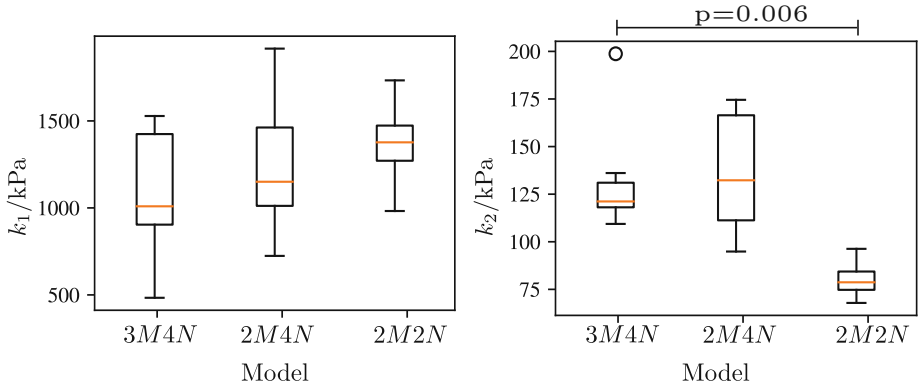

Figure 2.7: Plots showing k_1 (left) and k_2 (right) calibrated with varying Maxwell layers M and ramp-holds N steps at 0.2 strain for porcine muscle tissue.

2.3.3 Comparison to commonly used material properties

To obtain material parameters that are commonly used in literature, the long term elastic modulus $E_\infty(\varepsilon(t))$, and instantaneous elastic modulus $E_0(\varepsilon(t))$ for each strain level was calculated from equations 2.21 and 2.22 respectively (see Table 2.2). An increasing trend is observed with increasing strain level. While a decreasing stiffness is observed with decreasing model layers for both muscle tissue and liver tissue. The storage modulus E'',

	3-layer		2-layer		1-layer	
ε	E_0	E_∞	E_0	E_∞	E_0	E_∞
Muscle						
0.06	2.0	250	2.0	270	2.0	170
0.13	7.5	650	7.0	720	7.7	440
0.20	13	1030	13	1240	14	68
0.26	20	1590	18	1530	20	870
Liver						
0.04	0.1	64	2.0	22	0.1	6.8
0.08	0.8	150	7.7	100	0.8	33
0.12	2.5	300	14	190	2.6	100
0.16	4.4	630	20	400	4.3	220

Table 2.2: Identified long term elastic modulus (E_∞) and instantaneous elastic modulus (E_0) based on identified spring constant values (k_i) for each strain level (n) for porcine muscle and liver tissue.

loss modulus E' and loss tangent $tan\delta$ per calibrated strain level n were also calculated (see Table 2.3), based on AQLV model parameters. Loss tangent values ranged from 0.073 to 0.086 for porcine muscle tissue and from 0.044 to 0.085 for porcine liver tissue with small variations with increasing strain level and model layer reduction.

	3-layer			2-layer			1-layer		
ε	E'	E''	$\tan\delta$	E'	E''	$\tan\delta$	E'	E''	$\tan\delta$
Muscle									
0.06	254	19.0	0.074	300	24.4	0.081	164	14.2	0.086
0.13	758	56.7	0.074	783	62.6	0.079	434	37.2	0.085
0.20	1210	89.8	0.073	1360	107	0.079	790	68.0	0.085
0.26	1850	137	0.074	1660	132	0.079	860	73.6	0.085
Liver									
0.04	33.0	2.1	0.065	19.0	1.3	0.067	11.2	0.9	0.086
0.08	59.0	3.6	0.061	39.6	1.9	0.047	17.8	1.5	0.084
0.12	164	11.4	0.069	81.0	3.6	0.044	46.0	3.9	0.085
0.16	405	30.2	0.074	179	11.2	0.063	90.7	7.7	0.085

Table 2.3: Identified storage modulus (E'), loss modulus (E'') and loss tangent ($\tan\delta$) per strain level based on identified spring stiffness values (k_i) for porcine muscle and liver tissue.

2.4 Discussion

In this study, soft biological tissue (porcine muscle and liver), was modelled in the framework of the AQLV model under physiologically relevant large strains ($\varepsilon > 3\%$ [155]). Model parameter reduction was performed to ease comparison across different soft biological tissues and tissue mimicking materials, and further, to reduce the experimental burden.

Nie et al. [106] performed uniaxial tensile tests on porcine muscle and showed engineering stresses in the range of 25 kPa for 20% strain. Experimentally determined stresses for porcine muscle was $\approx$ 30 kPa for 20% strain obtained in the current study. Song et al. [134] applied varying strain rates on porcine muscle tissue and showed similar stress ranges ($<$ 100kPa), to experimental stress values for applied strain of $\approx$ 40% on porcine muscle tissue (for a strain rate of 0.007/s). These differences in stresses can be related the influence of anatomical locations, of obtained tissue [134] as well as differences in strain rates. Previously, porcine liver tissue was also tested in tension and compression with strains up to 20%, reporting stress levels in the range of 10 kPa by Chui et al. [33]. Similarly, in the current study, a stress amplitude of $\approx$ 8 kPa stress was determined for a strain level of 16%. These comparisons indicate a good overlap of our experimental stresses to previous literature.

Extraction of material properties from constitutive models is commonly performed by minimizing a target function, containing model stress and experimental stress with a set of material parameters. Results of modelling are usually compared by means of R^2 [3, 157, 169] or a root mean square error (RMSE) [33, 92, 122, 142]. R^2 values are a relative measure of fit and hence, are useful in comparing between models while RMSE values are absolute measures of fit and are useful for comparing models to experimental results. Thus, both measures were applied in this study.

Early literature on modelling of soft tissue was based on simple linear elastic models [98, 150]. Later, more complex hyperelastic material models were also used in modelling the non-linear behaviour observed in soft tissue such as in [48, 145, 81, 19, 96]. Chui et al. [33] modelled liver tissue with a hyperelastic model and determined an RMSE in the range of 0.047 to 0.09 kPa. Miller et al. [92] applied a strain energy based non-linear hyper-viscoelastic model to describe monkey liver tissue with a single strain level up to 35%, reporting high model fits ($R^2 = 0.974$ to 0.996) for varying loading speeds. Loocke et al. [147] measured strain dependent Young's moduli of porcine muscle tissue, modelled as transversely isotropic, at 30 % strain with good experimental fits (R^2 =0.99) and mean prediction errors of between 3.5% and 9.5%. Linear viscoelastic models such as the Prony series have also been applied to modelling soft biological tissue [39, 148, 159], however, due to the complexity of soft tissue mechanical behaviour, non-linear viscoelastic models were further required [15, 91, 70]. For example, Capilnasiu et al. [25] applied viscoelastic adapted forms of the Mooney-Rivlin and Ogden exponential models to model liver tissue, while Loocke et al. [149] modelled porcine muscle tissue in the framework of the QLV model at varying strain rates, and determined errors of $<$ 25% between model

and experimental data.

Generally, authors focused on the strain rate dependence of soft biological tissues at a single strain level; here however, the original AQLV model ($3M4N$) is applied to several strain levels, each tested at the same strain rate. Theoretically, the flexibility of the AQLV model should enable the variation of strain rates of a calibrated soft tissue, this however, requires further testing to be conclusive. In the current study, the AQLV model showed high model fits (≈ 0.98) when samples are fitted individually, however slightly lower model fits (R^2=0.90 and R^2=0.86 for porcine muscle and liver respectively) were obtained when based on the LOOCV. The LOOCV shows how well the average set of parameters obtained from the set of specimens would predict a stress behaviour of a new tissue sample, these values were therefore lower due to the high variations in soft tissues. Previous studies also produced comparable individual model fits, for e.g. the QLV model for a single level ramp-hold test by Abramowitch et al. (R^2=0.99 [3]) or a neo-Hookean based QLV model by MacManus et al. (R^2=0.94)[83]. Quaia et al. [121, 120, 119] applied both the QLV and AQLV models to eye muscles in primates. They showed that the AQLV model provided a better fitting to experimental data but required a large number of parameters (35) as compared to the QLV model with (8) parameters and proposed a further extension of the models.

In this study, the AQLV model was applied as originally published and an investigation into material parameter reduction was conducted. A reduction of the number of model layers (M) as well as a reduction in the number of ramp-hold steps (N) for calibration of the AQLV model was performed. Model parameters are obtained by calibrating relaxation stresses with AQLV models. The non-linear elastic ramp fits are produced by implementing the calibrated parameters from hold equation Eqn.3.19 into the ramp equation Eqn.3.18, as originally described Nekouzadeh et al. [103], which serves as a form of parameter validation. Alternatively, and for a possibly better fit, one could optimize the non-linear elastic response directly with the ramp stresses and obtain material parameters and response. The predictive ability of the original 3-layer ($3M4N$) model and 'reduced' ($2M4N$, $1M4N$) models were also compared qualitatively based on the R^2 values. For porcine muscle tissue, there was no significant difference between the 3-layer (0.90 ± 0.13) and 2-layer model (0.89 ± 0.15) fits ($p = 0.47$). The 1-layer model showed notably poorer results (0.83 ± 0.08) however no significant difference with the original 3-layer AQLV model ($p = 0.16$) was determined. Similar results are observed for porcine liver tissue with no significant difference between the 3-layer (0.86 ± 0.10) and 2-layer (0.85 ± 0.08) model fits ($p = 0.44$). The 1-layer model also showed poorer results (0.84 ± 0.01) but was not significantly different from the 3-layer model ($p = 0.22$). The slight difference of only 1 % when adding a third layer (in muscle and liver tissue) does not substantially add meaning to fits in terms of underlying internal processes. In contrast, subtle differences between tissues may still be highlighted with more relaxation time constants, but also may lead to ambiguity, as previously mentioned for a discrete QLV model [10].

Quantitative results (RMSE) following LOOCV of porcine liver tissue indicated the

original 3-layer model as the best fit model RMSE (0.284 ± 0.06) kPa as expected. The 2-layer model showed a RMSE (0.295 ± 0.219) kPa and the 1-layer model demonstrated a higher RMSE (0.346 ± 0.154) kPa. No significant difference between the 1-, and 2-layer models was observed ($p = 0.45$ and $p = 0.26$ respectively). For porcine muscle tissue the 1-layer and 2-layer models showed a relatively similar RMSE of (2.61 ± 2.54) kPa and (2.52 ± 1.61) kPa each better than the 3-layer model values. No significant difference however was observed between the results of the 1-layer and 2-layer models and the original 3-layer model ($p = 0.14$ and $p = 0.22$ respectively). An overall observed poorer performance of the 3-layer model at larger strains in the ramp phase was associated with the cubic spline interpolation, causing a greater oscillation of the model predicted stresses as compared to the experimental data. Hence, due to fewer parameters in the 1-layer model, the ramp prediction produces a better fit, compared to the 2-layer and 3-layer model. Since each phase (ramp and hold) are weighted equally, this offsets the poorer performance in the hold phase of the 1-layer model. The RMSE results are more conspicuous for porcine muscle tissue due to high stresses produced by porcine muscle tissue, as compared to liver tissue. A reasonable compromise in terms of accuracy and number of parameters was therefore the 2-layer AQLV model, with a total number of 14 parameters ($L = 14$).

The mean k_1 and k_2 for four samples of porcine muscle tissue tested at two strain levels (0.2 and 0.4 global strain) ($N = 2$) were determined for the 2-layer AQLV model. For k_1, which has the greatest effect on the predicted stresses, values of (1370 ± 310 kPa) were obtained for $2M2N$, which were within a similar range of values calibrated at four strain levels ($N = 4$) for $2M4N$ (1230 ± 400) and $3M4N$ (1020 ± 390), given a maximum i.e greatest percentage deviation of 16.8%.There was no significant difference between values obtained k_1 values ($p = 0.22$). Values for k_2 were however slightly underestimated for ($N = 2$) (76 ± 17) kPa as compared to those obtained from ($N = 4$), $2M4N$ (120 ± 29) kPa and $3M4N$ (120± 34) kPa. There was a significant difference between values of k_2 obtained from a 4 step test and 2 step test ($p = 0.006$). This may lead to a slight underestimation in model stresses. Notwithstanding, the reduced AQLV model ($2M2N$) is able to accurately model the stress behaviour of a 2 ramp-hold experiment with high accuracy ($R^2 = 0.96 \pm 0.02$ and RMSE =1.74 ± 0.82) kPa. The proposed reduced-parameter AQLV model ($2M2N$) produces 8 parameters in total ($L = 8$). This would be a reasonable compromise between accuracy of the model, number of material parameters for comparison and experimental burden. Taken together, the AQLV model provides a comprehensive description of both, the non-linear elastic and viscoelastic behaviour of soft biological tissue; higher model fits are generally obtained for single strain level model calibrations, however these models are unable to accurately describe stress responses at varying strain levels as compared to the AQLV model. A higher accuracy is also possible with the AQLV model, however with at the expense of a high number of material parameters and greater experimental burden. It is noted that relaxation times often describe short and long-term responses of internal physical processes undergone during loading within the tissue. An example of such, would be the fast response of collagen fibres (≈7s -100s) as well as the long-term response of other constituent

materials such as proteoglycans [129]. However, it is difficult to specifically link these processes to parameters obtained from the AQLV models without testing individual tissue constituents.

To obtain commonly used material parameters, Nava et al. [101] applied the QLV model to human hepatic tissue in vivo and obtained long term (E_∞) and instantaneous elastic modulus (E_0) to be 20 kPa and 60 kPa, respectively. Estermann et al. [39] estimated E_0 for porcine liver tissue to be around 130 $\pm$ 65 kPa. However, values for the elastic moduli of both porcine muscle and liver tissue in literature vary greatly due to variation of anatomical locations of tissues, test protocols, maximum strains, strain rates and whether or not optical strain measurement was used [81, 60, 32]. In the current study, values obtained from the AQLV model for E_0 for lower strains ($4\% - 8\%$) are within the general range (E_0 =33 - 58 kPa) of reported values. Interestingly, E_0 was observed to decrease with the number of Maxwell elements. Hence the response of reduced models to an instantaneous deformation is softer in comparison to the 3-layer model. This is unexpected, as an increase in the individual stiffness is expected in order to offset the loss of springs from the the 3-layer model. These values are, however, based on the assumption of linear viscoelasticity of spring damper systems and are less useful for representing the true non-linear behaviour of soft tissue [144]. It is also noted that the values obtained from the AQLV model, which represent the spring and dampers do not exist physically [104], but are numerical values that enable modelling of material behaviour.

The loss tangent ($\tan\delta$) has been shown, in previous literature [38, 170], to be a more robust material property and is more dependent on frequency or strain rate than on strain level. It has been reported in the range of 0.07 - 0.22 for porcine liver tissue [39, 159]. Similarly, results of approximations of loss tangents derived from current AQLV parameters (Table 2.3) show relatively small variations with across different strain levels. Loss tangent values for the 3-layer and 2-layer models were within a similar range (0.074 to 0.086) for porcine muscle, and in the range of (0.044 to 0.074) for porcine liver tissue. Higher values of loss tangent are observed for the 1-layer model. One could speculate that this may be due to the pronounced effect of the damper in the 'simpler' 1-layer model, however, this is conjecture without further analysis. These derived parameters are mostly only valid for small strain levels (linear viscoelasticity) are only useful for giving rough estimates to allow for the comparison of AQLV model parameters to existing literature.

In summary, the original AQLV model could accurately model the strain dependent non-linear viscoelastic behaviour of porcine muscle and liver tissue. The flexibility of the model enabled the proposal of a 'parameter-reduced' AQLV model, with a reduced number of parameters and a reduced experimental burden. This is especially advantageous for comparing several different biological tissues. Further, given the large variation in biological tissues due to age, sex and disease [82, 5, 143, 88], it is questionable if a much higher accuracy is advantageous over the decreased experimental burden and less than half of the material parameters of the AQLV model. This becomes especially important when it is more important to gain both an accurate understanding of tissue behaviour as well as a representative order of magnitude of material properties.

2.5 Conclusion

This paper characterized the non-linear viscoelastic behaviour of soft biological tissue (porcine skeletal muscle and liver) at physiologically relevant large strains ($\varepsilon > 3\%$) based on the AQLV model. Adaptations of the originally published model were made to reduce the number of material parameters by reducing the number of layers i.e. the number of parallel spring damper systems in the standard AQLV model as well as the number of ramp-hold tests used for calibration. The adaptations eased the comparison of material parameters for the different soft biological tissues (porcine muscle and liver), while still providing sufficiently accurate modelling of their non-linear viscoelastic behaviour. In conclusion, a reduced AQLV model (2 Maxwell layers, 2 ramp-hold phases) is able to predict the visco-elastic behaviour of soft biological tissues with a sufficient accuracy. Hence, this proposed reduced AQLV model will ease comparison across different soft biological tissues in future and reduce the experimental burden associated with calibrating the model.

Acknowledgements

The research was a cooperation with the Austrian Center for Medical Innovation and Technology (ACMIT), funded in the “Forschung, Technologie & Innovation” (FTI) framework of the Provincial Government of Lower Austria (Land Niederösterreich) under grant assignment number WST3-F2-528983/005-2018. The authors want to appreciate the contribution of Lower Austria Landesgesundheitsagentur, legal entity of University Hospitals in Lower Austria, for providing the organizational framework to conduct this research. The authors acknowledge TU Wien Bibliothek for financial support through its Open Access Funding Programme.

Appendix A.

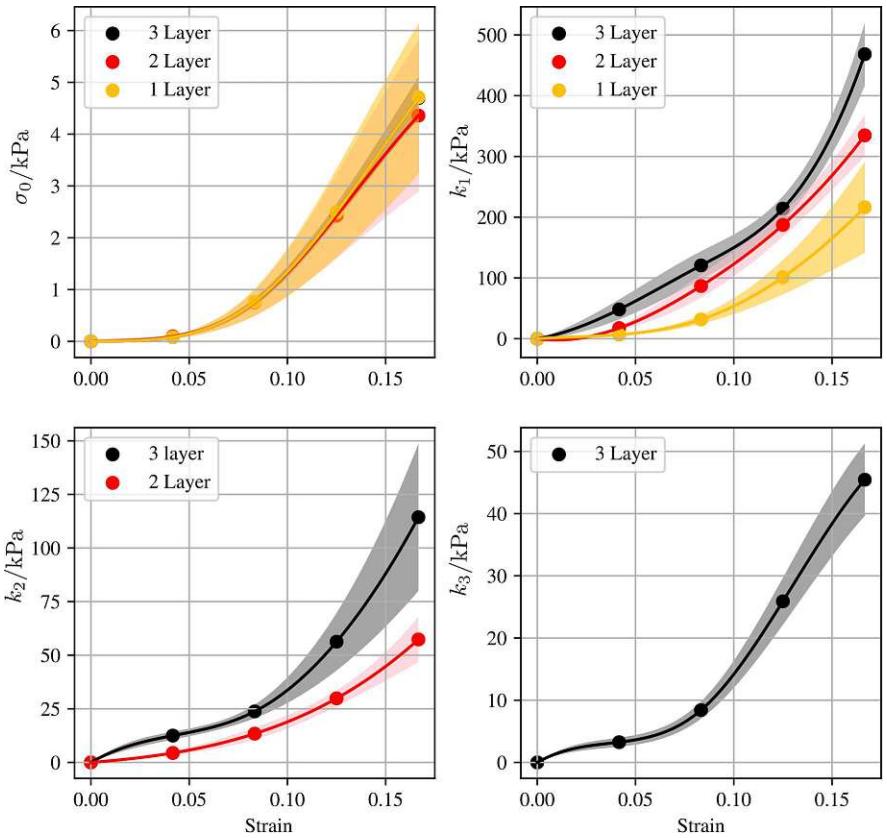

Figure 2.8: Mean ± confidence interval of equilibrium stresses (σ_0) and spring constants (k_i) values of AQLV models of porcine liver. Dots represent calibrated average values connected by cubic spline interpolations. Shadowed regions represent the 95% CI.

CHAPTER 3

Paper 2

From manuscript:

Fracture toughness determination of porcine muscle tissue based on AQLV model derived viscous dissipated energy

Othniel J. Aryeetey, Martin Frank, Andrea Lorenz, Dieter H. Pahr

Published: J. Mech. Behav. Biomed.Mater.10.1016/105429 August 2022

Abstract

The ability of soft collagenous tissue (SCT) to withstand propagation of a defect in the presence of a macroscopic crack is termed the 'fracture toughness parameter'. In soft tissues not undergoing significant plastic deformation, it is purported that a considerable amount of additional energy is dissipated during failure processes, due to viscoelasticity. Hence the total work, measured experimentally during failure, is the sum of fracture and viscoelastic energies. Previous authors have aimed to apply constitutive modeling to describe viscoelastic hysteresis for fracture toughness determination with a tendency of models to either over or underestimate the viscous energy. In this study, the fracture toughness of porcine muscle tissue is determined using two strategies. Firstly, it was determined experimentally by calculation of the difference in dissipated energy of notched and unnotched tissue specimens undergoing cyclic 'triangular wave' excitation with increasing strain levels in uniaxial tension. The second strategy involved the extension and use of the adaptive quasi-linear viscoelastic model (AQLV) to model cyclic loading (model parameters were obtained from a previous study) and sequentially the dissipated energy was calculated. The mean value of the dissipated energy based on the AQLV approach was

then subtracted from the total dissipated energy of notched porcine muscle tissue samples to determine the fracture toughness. The mean experimental viscous dissipated energy ratio was 0.24 ± 0.04 in the experimental approach, compared to 0.28 ± 0.03 for the AQLV model. Fracture toughness determined experimentally yielded 0.84 ± 0.80 kJ/m2, and 0.71 ± 0.76 kJ/m2 for the AQLV model, without a significant difference (p = 0.87). Hence, the AQLV model enables a reasonable estimation of viscous dissipated energy in porcine muscle tissue with the advantage to perform tests only on notched specimens, instead of testing additional unnotched samples. Moreover, the AQLV model will help to better understand the constitutive viscoelastic behaviour of SCTs and might also serve as a basis for future fracture toughness determination with constitutive model simulations.

keywords: *viscosity, energy dissipation, fracture toughness, soft tissu, quasi-linear viscoelasticity*

3.1 Introduction

An understanding of failure mechanisms in soft biological tissue is vital in assessing defects in a number of medical issues, such as iatrogenic rupture of fetal membranes during fetal surgery and skin or tendons and ligaments during sporting activities or injuries [18]. Hereby, the ability of a material to withstand propagation of a defect is generally referred to as fracture toughness [140].

Soft collagenous tissues (SCT) have been shown to be highly non-linear viscoelastic in their mechanical response [135, 47] and are thus capable of absorbing large amounts of energy per unit volume with relatively low elastic moduli [140]. Hence, the process of fracture in SCTs is often observed as a 'yawning' of a defect upon application of a tensile load leading to a decrease in stress concentration around the defect [166]. These processes can be modelled as an interchange of energy between the internal strain energy of the tissue and the irreversible fracture work done to propagate a crack through the material [1]. Thus, energy based fracture mechanics (FM) methods are the best representative models for such interactions [9].

Previous authors have applied linear viscoelastic fracture mechanics methods to describe the fracture behaviour of soft biological tissues. Chin-Purcell and Lewis [31] applied elastic and hyperelastic models to describe fracture mechanics in soft biological tissue. The large deformation and strain rate dependency of the tissue were however only approximated and a further analysis was proposed. Purslow et al. [115] showed the time-dependent behaviour of fracture toughness on rat skin. A commonly used approach was presented by Oyen-Tiesma and Cook [109] who determined the fracture resistance of cultured neocartilage from cyclic tensile tests with notched and unnotched specimens and determined the dissipated energy of each cycle. The work done for fracture in a notched sample was determined from the difference of the total dissipated energy and the predicted viscoelastic energy (from unnotched cycles). Fedewa et al. [41] also applied a similar method but determined the viscous energy in a notched sample during cycles where the crack did not propagate. Both methods showed that large amounts of energy

are required to overcome dissipated energy due to viscoelasticity. Koop and Lewis [75] showed that the Oyen method underestimates the viscoelastic energy for high strain rates (>2.5 mm/s) and overestimates for lower strain rates and hence proposed the use of a linear viscoelastic constitutive model to determine the 'exact' viscoelastic energy. The model, however, imposes an almost instantaneous drop in strain to simulate crack propagation and employs a single time constant, which may lead to errors.

Further work done by Babaei et al. [11] showed that the hysteresis energy could be determined using a non-linear viscoelastic model, the quasi-linear viscoelastic (QLV) model. Babaei et al. showed the ability of the model to describe hysteresis regions with varying strain rates. However, for the QLV model, it is known that, material parameters calibrated at a given strain level do not fit well with changing strain levels [114]. Furthermore, since cyclic tensile tests in a fracture toughness experiment are often performed at increasing strain levels with constant strain rate [109], it is necessary to implement a formulation that accounts for this loading scenario. The adaptive quasilinear viscoelastic model (AQLV) developed by Nekouzadeh et al. [104] has been shown to model the strain-dependent viscoelastic behaviour of soft biological tissue [120, 119, 6] for different strain levels.

In this study, the fracture toughness of porcine muscle tissue was determined using two strategies. Firstly, by determining experimentally the difference in dissipated energy in notched and unnotched tissue specimens undergoing cyclic 'triangular wave' excitation with increasing strain levels in uniaxial tension. The second strategy involved the extension and use of the adaptive quasi-linear viscoelastic model (AQLV) to model cyclic loading (model parameters were obtained from a previous study [6] to determine the dissipated energy of the 'unnotched' sample. The mean value of the dissipated energy based on the AQLV approach was then used to determine the fracture toughness of experimental (notched) porcine muscle tissue samples. It was hypothesized that the viscoelastic energy and further, the fracture toughness parameter obtained from both approaches are not significantly different. Hence, it was speculated that the AQLV model can be reasonable applied to determine the dissipated energy of soft biological tissue as well as used to determine the fracture toughness.

3.2 Methods

The current study aimed to determine the viscous dissipated energy of a soft biological tissue at varying strain levels within the framework of the AQLV model and to thereby determine the fracture toughness of the tissue. The material parameters of porcine muscle tissues were determined based on incremental ramp hold experiments in a previous study [6]. A deep description of the AQLV model is given by the original authors of the AQLV model (Nekouzadeh et al., 2007; Nekouzadeh and Genin, 2013). Here, the AQLV model is extended to describe constant strain rate cyclic (triangular wave) loading based on concepts from Yang et al. (Yang and Chen, 1982) and Babaei et al. (2018) to determine the hysteresis energy at varying strain amplitudes.

In the current study, the AQLV model is extended to describe the deformation and recovery half-cycle, and accounting for the strain level dependency of the model. The stress response of the loading half-cycle (0 ≤ t ≤ T/2) and the recovery half-cycle (T/2 ≤ t ≤ T) is given by:

$$\sigma(t) = \begin{cases} E_0\dot{\varepsilon}_0(t) + \sum_{i=1}^{n} E_i\tau_i\dot{\varepsilon}_0\left(1 - e^{(-t/\tau_i)}\right), & 0 \le t \le \frac{T}{2} \\ E_0\dot{\varepsilon}_0(T-t) + \sum_{i=1}^{n} E_i\tau_i\dot{\varepsilon}_0\left(2e^{\left(\frac{T-2t}{2\tau_i}\right)} - 1 - e^{\left(-\frac{t}{\tau_i}\right)}\right), & \frac{T}{2} \le t \le T \end{cases} \tag{3.1}$$

whereby the relaxation time τ_i is the ratio of the dashpot coefficient $b_i(\epsilon(t))$ to the spring constants $k_i(\epsilon(t))$, $(\tau_i = bi/ki)$. A brief description of the concepts used are given in Appendix A.

3.2.1 Theory

The current study aims to determine the viscous dissipated energy of a soft biological tissue at varying strain levels within the framework of the AQLV model and to thereby determine the fracture toughness of the tissue. The material parameters of porcine muscle tissues were determined based on incremental ramp hold experiments in a previous study [6]. A deep description of the AQLV model is given in the original authors of the AQLV model [104, 103]. Here, the AQLV model is extended to describe constant strain rate cyclic (triangular wave) loading based on concepts from Yang et al [165] and Babaei et al. [11] to determine the hysteresis energy at varying strain amplitudes. A brief description of the concepts used are given in the Appendix A.

Dissipated energy

The total energy of a triangular wave cycle W_T is the area under the loading half cycle, while the storage energy i.e. elastic energy W_S is the area under the unloading half cycle. The dissipated energy W_D is the area between the loading and unloading half cycles. The ratio of the dissipated energy to the total energy is referred to as the dissipated energy ratio (U_D) as defined by Oyen et al. [109] is given by :

$$U_{\mathrm{D}} = \frac{W_{\mathrm{T}} - W_{\mathrm{s}}}{W_{\mathrm{T}}} = \frac{W_{\mathrm{D}}}{W_{\mathrm{T}}} \tag{3.2}$$

The analytical solution to determine the hysteresis energy can be determined based on Yang et al. [165] as follows:

$$W_D = \sum_{i=1}^{N} k_i(\varepsilon(t))\dot{\varepsilon}_0^2\tau_i^2\left(-3 - \mathrm{e}^{-\frac{T}{a_i}} + 4\mathrm{e}^{-\frac{T}{2\tau_i}} + \frac{T}{\tau_i}\right) \tag{3.3}$$

In this study, the fracture toughness parameter J_{c}, which is defined as the amount of energy required to propagate a crack in a sample is determined. For viscoelastic materials,

a significant amount of energy is dissipated by viscoelastic processes. In the absence of crack propagation, the dissipated energy W_D is equal to the dissipated energy W_D^v due to viscoelasticity. Here cyclic loading is performed at the same strain level for several cycles. It is assumed that for each strain level, the initial cycle dissipates energy due to both viscous and plastic processes, hence at the final steady state, the effect of plastic deformation is negligible. For notched samples crack propagation occurs within the first cycle, hence most of the energy is associated with irreversible plastic deformation and tearing. These are not directly separable and are here denoted as fracture energy W_F. Hence during crack propagation, the $W_D > W_D^v$. The fracture energy W_F per cycle n, where a crack is propagated, is the difference of the dissipated energy W_D and the dissipated energy W_D^v due to viscous processes, and can be given by:

$$\begin{aligned} W_F(n) &= W_D(n) - W_D^v(n) \\ &= W_D(n) - (W_T(n) * U_D(n)) \end{aligned} \tag{3.4}$$

The fracture toughness parameter J_c per cycle n, is calculated per increase in the change in crack length Δa:

$$J_c(n) = \frac{W_F(n)}{[B \cdot \Delta a(n)]} \tag{3.5}$$

, where B is the thickness of the sample. This typically leads to the Resistance curve (R-curve), however, due to the relatively large thickness of the samples and distortion in tearing through the tissue samples, determination of the crack length at each cycle is difficult and prone to errors. Accordingly, Chin-Purcell et al. [31] showed that for very compliant materials, the measurement of crack propagation can become unwieldy and hence create confusion in the definition of a crack. To overcome this issue, the total fracture toughness parameter was calculated as the sum of the fracture energy over the total number of cycles N and the total change in crack length Δa, which is essential the difference between the sample width and the length of the initial crack a. Hence the single parameter fracture toughness of the tissue, J_c was calculated by the following relation:

$$J_c = \frac{\sum_{n=1}^{N} W_F}{[B \cdot \sum \Delta a]} \tag{3.6}$$

3.2.2 Study Design

Material parameters of the originally published AQLV model were obtained from stress relaxation experiments of porcine muscle tissues performed in a previous study [6]. Triangular wave excitation was applied to both unnotched and notched samples to obtain stress strain data (8 specimens each).

The experimental stress strain curves were plotted and energies i.e. W_T, W_S, W_D were calculated numerically by means of the area under the curves using the *numpy.trapz* function in Python 3 for both notched and unnotched samples. The dissipated energy

ratio U_{D} at the steady state (8th, final cycle) of each strain level of the unnotched samples, was determined and the mean steady state U_{D} for porcine muscle tissue was calculated. It is assumed that for each strain level, the initial cycle dissipates energy due to both viscous and plastic processes, hence at the final steady state, the effect of plastic deformation is negligible

The AQLV model was extended to model triangular wave excitation as described in 3.1 & 3.3. Relaxation times τ_i and spring stiffnesses $k_i(\varepsilon(t))$ as well as strains from cyclic (unnotched) loading experiments were fed as inputs to the analytical model in Python 3. The dissipated energy ratio U_{D} (analytical)at the steady state (final cycle) of each strain level was determined. A condition was placed on the model that each strain level was modelled with a start time of 0 and hence, the entire strain history was not modelled, instead each strain level was modelled individually. This approach was necessary to avoid complete relaxation at later cycles in the model, which was not observable in experiments. Material parameters were obtained from previous stress relaxation experiments [6].

8 unnotched samples were tested and the dissipated energy in each cycle was calculated and the average UD over all samples was obtained. 8 additional samples were notched and tested in cyclic loading. The dissipated energies displayed in 3F are of a typical notched sample test. To obtain the fracture energy of each individual notched sample, the average UD from the unnotched sample was applied to each cycle to obtain the fracture energy. The total remaining energy was then summed up over all cycles to obtain the total fracture energy per sample. The porcine muscle tissues in these previous tests (ramp-hold) were preconditioned by allowing samples to relax for 300s prior to testing, while current cyclic samples were preconditioned in a cyclic manner as done previously [109].Also, although porcine muscle tissue was taken from the same muscle region (M. longissimus), specimens for these experiments were ultimately from different animals. Therefore, peak stresses obtained with the AQLV model were scaled to experimental stresses to overcome differences due to tissue variation and tissue preconditioning. Since both loading and unloading stresses are scaled by the same value, no effect is noted on the ratio of energies.In this engineering stresses and strains are used in order to simplify the study.

3.2.3 Sample Preparation

Whole porcine skeletal muscle (M. logissimus) were obtained fresh from a local abbattoir. Porcine skeletal muscle samples were sliced (see Figure 3.1), into rectangular $75 \cdot 20 \cdot 5$ mm^3 ($L \cdot B \cdot T$) samples as described previously by Estermann et al. [40]. Specimens were stored in a physiological saline solution (9 g/l NaCl) at room temperature immediately after incision, until testing, to ensure hydration. A total of 16 porcine muscle specimens (8 samples for unnotched and 8 for notched testing) were tested experimentally.

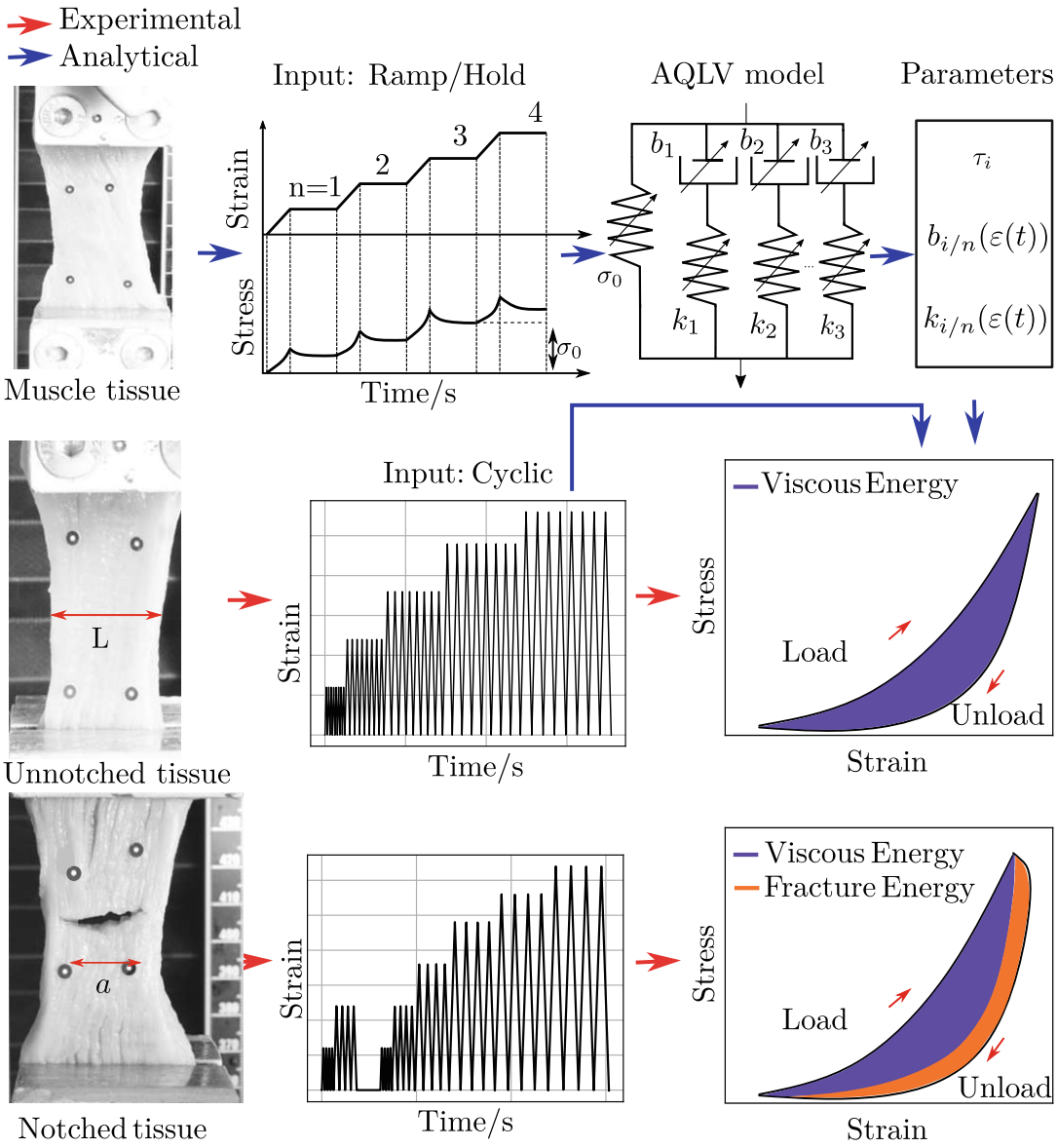

Figure 3.1: Study design showing the work-flow of experimental and analytical (AQLV) modelling approaches applied in this study. Porcine muscle tissue (M. longissimus) is tested in incremental ramp-hold tests in uniaxial tension to determine the AQLV material parameters as well as with triangular wave excitation to determine the hysteresis (dissipated) energy for notched and unnotched samples.

3.2.4 Mechanical Testing

Experiments were carried out using an electro-mechanical test machine (Zwickiline Z2.5, Zwick Roell GmbH, Ulm, Germany) in combination with a 100 N load cell (S2M HBM, Freiburg, Germany) operated at 10 Hz. A high resolution camera (Sony α-6400, Sony, Tokyo Japan) was used for optical video recording at 1 Hz.

White dot markers (GOM, Braunschweig, Germany) were placed slightly below the upper clamped region and above 15 mm from the bottom end to avoid bell ends and to ensure that the gauge area was vertical. These were used for strain tracking analysis with a point tracking algorithm described previously by Frank et al. [45] (see Figure 3.1). Effective gauge length was approximately 40 mm for both tissue types. Specimens were subsequently clamped on both ends. Cyclic loading tests were performed on rectangular specimens following a preconditioning phase. Preconditioning was performed for all cyclic tests by loading samples cyclically to peak strain amplitudes between 0.04 and 0.20 and then allowing the sample to relax for 300s. Eight unnotched specimens each were tested under cyclic loading. For fracture toughness determination, 8 additional unnotched specimens were preconditioned similarly, after the relaxation phase, notching was performed with a No. 11 B3 scalpel and an incision of approximately 12 mm was made in the sample. Cyclic loading was performed with peak strains ranging from 0.04 to 0.36 for notched samples as these required higher displacements to enable crack propagation.

3.2.5 Stress and strain determination

Actual sample strains were obtained via digital image correlation (DIC). Hereby, the position of the markers is tracked over time and the relative displacement between the marker positions at the top and bottom is determined. In this study, engineering stresses and strains from digital image correlation (DIC) are used in order to simplify the study. Hence, engineering strain is computed as:

$$\varepsilon(t) = \frac{l(t) - l_0}{l_0} \tag{3.7}$$

where l_0 is the initial length (at zero-force) and $l(t)$ the actual length of the tissue. The uniaxial linear engineering stress (σ) is calculated from the axial measured force (f) and the cross sectional area ($A_0 = B \cdot T$), measured with a caliper (prior to testing) and averaged at 3 positions, using the following equation:

$$\sigma(t) = \frac{f(t)}{A_0} \tag{3.8}$$

3.2.6 Statistical analysis

Statistical significance was determined between the experimentally determined and analytically determined dissipated energy ratio U_D using the Mann-Whitney U test for a significance level of $\alpha = 0.05$ implemented in Python 3.7.

3.3 Results

3.3.1 Experiment

Stress-strain-time behaviour under cyclic loading

Plots showing the averaged (black) and standard deviation (gray) of stresses obtained during unnotched cyclic loading of porcine muscle tissue specimen is shown in Figure 3.2. Viscoelastic relaxation i.e. Mullins-type softening [99] of the stresses over time with each cycle at each increasing strain level is observed. A more pronounced stress relaxation behaviour is observed at higher strain levels (see Figure 3.2B).

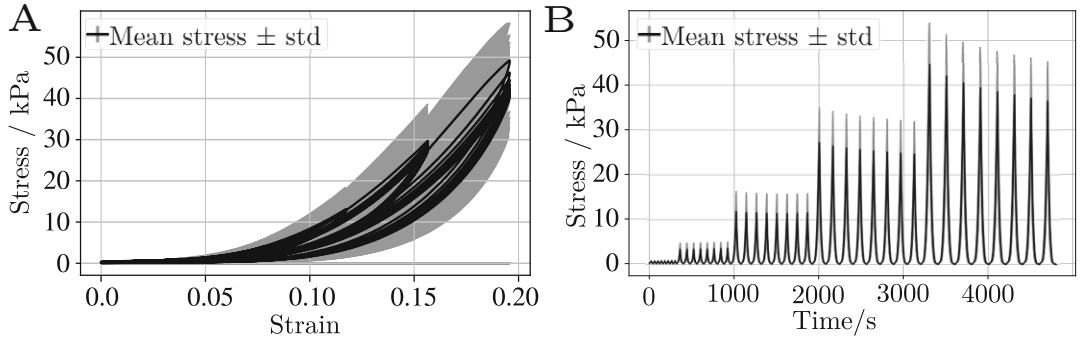

Figure 3.2: Plots showing the averaged (black) and standard deviation (gray) of the A) stress-strain B) stress-time response of uniaxial tensile test of porcine muscle tissue over all 8 specimens and 4 strain levels.

Viscous dissipated energy

The stress strain curves of a representative unnotched porcine tissue sample is shown Figure 3.3A. The energy distributions per cycle for each representative specimen, showing a decreasing trend in energy at a given strain level for the unnotched samples, is shown in Figure 3.3B. The dissipated energy ratio U_D for the unnotched samples shows quantitatively the observed larger hysteresis energy in the initial cycle of each incremental strain level (see Figure 3.3C), which is referred to as the 'transient state' [144], followed by cycles with increasing compliance up to the 'steady state' where no significant differences in hysteresis regions can be observed.

Fracture energy

The stress strain curve of a representative notched sample is shown in Figure 3.3D. Crack propagation is clearly observable by the jagged response of the stress strain curve in several cycles as compared to the smoother response of the unnotched sample in Figure 3.3A. The energy distributions W_T, W_S, W_D are calculated similarly for the notched tissue sample as for the unnotched sample where crack propagation is observable in cycles with a general increase in the dissipated energy W_D (see Figure 3.3E). Sequentially, U_D of the notched samples are larger describing regions of crack propagation. Initial cycles,

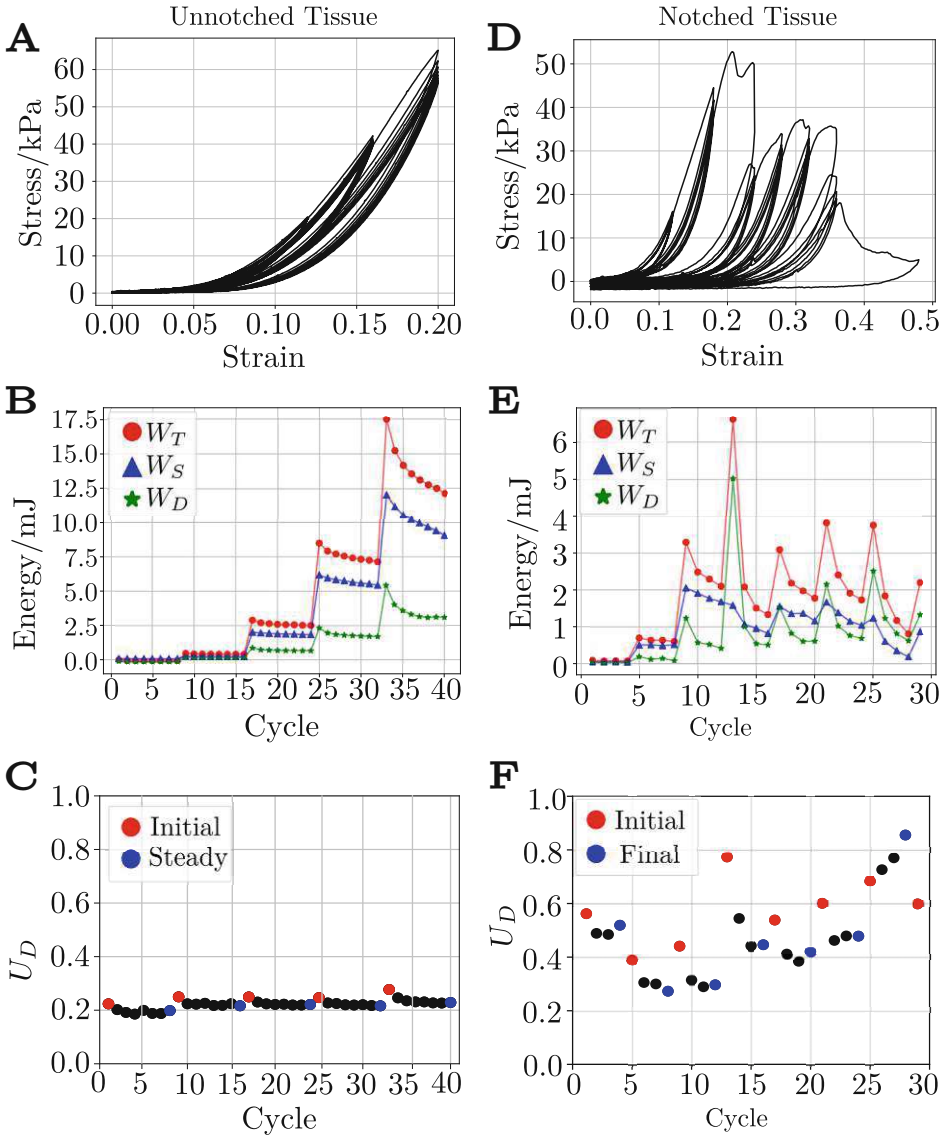

Figure 3.3: Results of representative porcine muscle tissue samples showing the stress-strain response with inherent hysteresis behaviour of A) unnotched D) notched sample. The distribution of distribution of total energy W_{T}, storage energy W_{S} and dissipated energy W_{D} in B) unnotched and E) notched sample as well as the dissipated energy ratio U_{D} for the C) unnotched sample showing the initial transient state and final steady state and F) notched samples.

show the largest energy dissipation at each strain level, are marked in red, and final cycles are marked in blue for differentiation (see Figure 3.3F).

3.3.2 Analytical solution

AQLV model Paramters

Average material model parameters were obtained from calibrating the adaptive quasi-linear viscoelastic model (AQLV) using incremental ramp-hold uniaxial tensile experiments on 8 porcine muscle specimens individually from a previous study [6]. The determined strain-dependent material parameters i.e., relaxation times τ_i, residual stress σ_0 and dynamic stiffness parameters k_i and standard deviation are provided in Table 3.1.

		τ_1/s	τ_2/s	τ_3/s
		10 ± 7	88 ± 54	840 ± 442
ε_n	σ_0	k_1/kPa	k_2/kPa	k_3/kPa
0.06	2.0 ± 1.5	220 ± 100	22 ± 7.2	10 ± 2.7
0.13	8.0 ± 4.8	650 ± 310	76 ± 44	41 ± 14
0.20	13 ± 5.0	1020 ± 390	120 ± 34	69 ± 16
0.26	20 ± 6.3	1570 ± 790	180 ± 38	95 ± 22

Table 3.1: Mean ± standard deviations of time constants τ_i, spring constants k_i, for each strain level ε_n of AQLV model for porcine muscle.

AQLV cyclic load prediction

The AQLV model was extended to model the loading and unloading stress response. Hence, the hysteresis area and the dissipated energy of porcine muscle tissue was determined, based on model parameters obtained from stress relaxation experiments. The mean stress-time results obtained using the average AQLV model parameters are shown in Figure 3.4A at each steady state strain level with standard deviation (blue) superimposed over the mean experimental stress-time curves. A detailed view of each steady state cycle is shown in Figure 3.4B-F for clarity. Rescaling of peak stresses produced a mean factor of ≈ 2.8 with the exception of the first 2 (4% and 8%) strain levels with a mean factor of ≈10, likely due to the larger effect of residual stress parameters on peak stresses.

A plot of the distribution of experimentally derived U_D(exp) across all samples over all cycles is shown in Figure 3.5A. A slight increase in the dissipated energy ratio is observed with increasing strain level. At each strain level, the initial U_D the 'transient' state is clearly observed to be higher with a decreasing trend to the final 'steady state' cycle. A relatively stable value for the steady state can be observed with only a slightly increasing trend in strain level for porcine muscle tissue. The distribution of the steady state U_D values of each steady state (final) cycle per strain level, is shown in Figure 3.5B for the experimental and AQLV approach. The mean dissipated energy ratio obtained from experimental stress strain curves was determined to be 0.24 ± 0.04, whereas the mean dissipated energy obtained from the AQLV model 0.28 ± 0.03 with an overestimation of U_D by an average of 16%. The dissipated energy during the notched cyclic loading tests per cycle for all tissue samples is shown in Figure 3.5C.

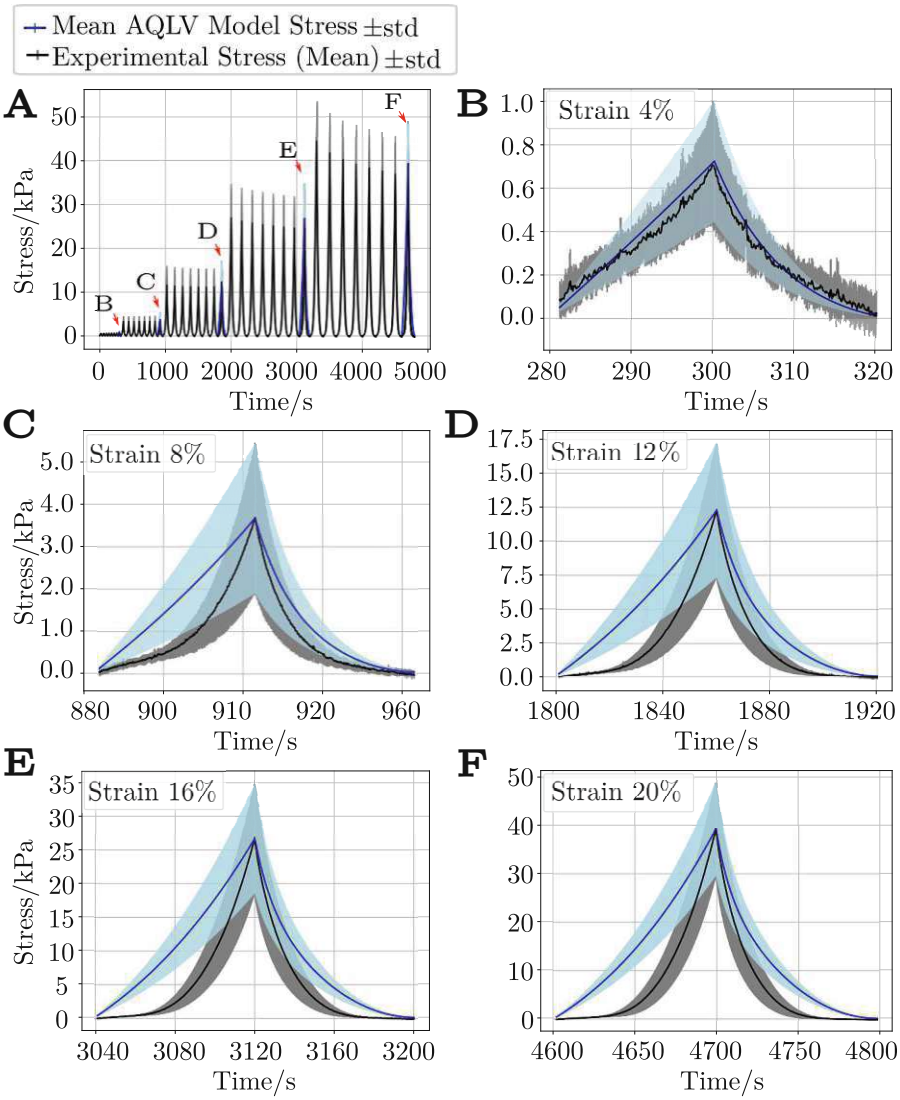

Figure 3.4: Mean AQLV model stress (red) and standard deviation (blue) of the steady state (final) cycles superimposed over experimental mean stress (black) and standard deviation (gray) A) over the entire cycle and B-F) at each steady state for clarity.

3.3.3 Fracture Toughness

A single fracture toughness of porcine muscle tissue (per specimen) was determined based on the dissipated energy ratio obtained from experiment as well as AQLV modeling. The mean fracture toughness obtained from experimental approach was $0.84 \pm 0.80\ kJ/m^2$ and from the AQLV model approach $0.71 \pm 0.76\ kJ/m^2$.

Although the distribution of U_D obtained from the experimental and AQLV approaches are significantly different (p=0.002), the effect of applying the mean value to determine

fracture toughness over several cycles and over varying tissues is not significant (p=0.87) (see Figure 3.5D).

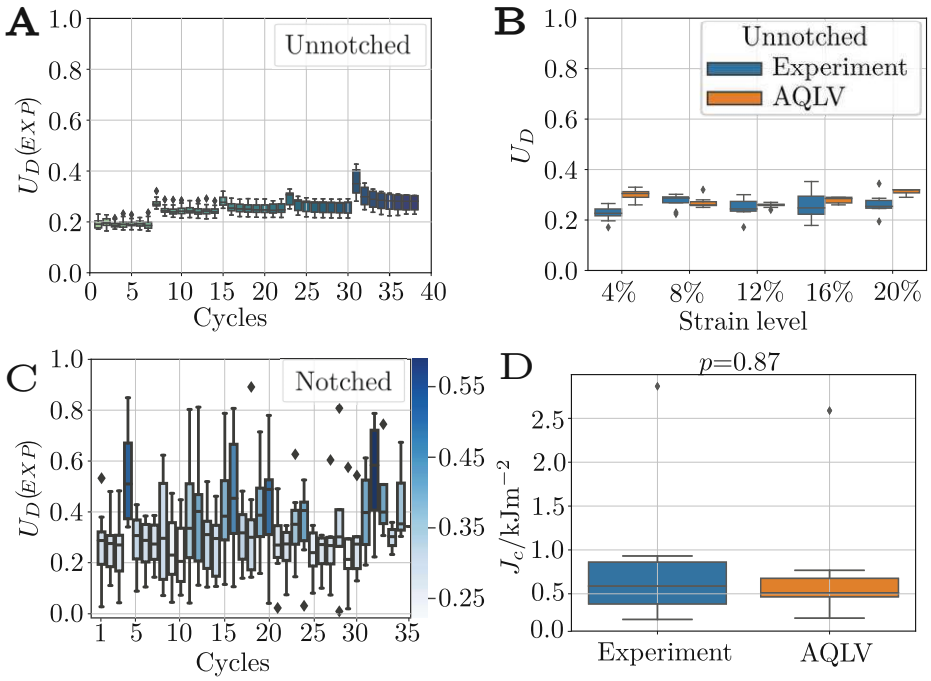

Figure 3.5: Box-plot showing the statistical distribution of A) Experimental dissipated energy U_{D} over all unnotched samples per cycle and B) Plot of experimental and AQLV model U_{D}. C) U_{D} of notched samples per cycle D) Fracture toughness obtained from calculation.

3.4 Discussion

In this study, the ability of the AQLV model to determine the viscous dissipated energy (hysteresis) of porcine muscle tissue with increasing strain levels was investigated. The obtained viscous dissipated energy ratio U_{D} of the model was compared to that of experiments. Fracture toughness was determined using both analytical and experimental measures. It was found that the viscoelastic dissipated energy could be modelled using the AQLV model and further, that the fracture toughness parameter obtained from both approaches was not significantly different.

For a given strain level, relaxation of peak stresses is observed with each proceeding cycle, known as the characteristic Mullins-type softening [99, 100] (see Figure 3.2B). A corresponding reduction in U_{D} is also observable until differences in U_{D} for subsequent cycles at a strain level are negligible. Hence, for each strain level, there is a change of viscous behaviour from the initial 'transient' cycle to the 'steady-state' cycle.

For a given strain level, the relaxation of peak stresses is observed with each proceeding cycle (see Figure 3.2B). A corresponding reduction in U_{D} is also observable until differences

in UD for subsequent cycles at a strain level are negligible. Hence, there is a change of viscous behaviour from the initial 'transient' cycle to the 'steady-state' cycle per strain level, known as the characteristic Mullins-type softening [99, 100]. The steady state value of U_D, over all strain levels, remained relatively constant, for a given strain rate and can hence, be considered a material constant. The mean experimental U_D calculated was 0.24 $\pm$ 0.04. The mean U_D determined from the steady state AQLV model was 0.28 $\pm$ 0.03, a mean deviation of $\approx$ 16%. There is a significant difference between the distribution of the model and experimental U_D (p = 0.002), however, the mean dissipated energy predicted by the AQLV model is within a reasonable range of the experimental results.

Previous authors have also applied varying models to describe the hysteresis energy in soft biological tissues. Best et al. [15] applied the QLV model to describe the hysteresis energy based on parameters obtained from the stress relaxation experiments. The dissipated energy ratio was determined experimentally for a rabbit muscle to be $\approx$ 0.4, however, the QLV model underestimated this value by $\approx$ 30%. The elastic response of the QLV model also did not describe the experimental behaviour of the experimental stresses accurately. Best concluded that the QLV model can model the structural response of muscle tissue, however with differences in the elastic behaviour.

Babaei et al. [11] applied the QLV model to describe cyclic loading in engineered tissue constructs and showed a relatively high viscous damping in the tissue constructs, depending on strain rate. The material parameters were obtained by directly fitting the QLV model on experimental results of cyclic loading, producing better model fits with data as compared to Best et al. [15]. Nava et al [102] also performed cyclic loading on bovine liver tissue and modelled the response in the framework of the QLV model. They noted however, that the QLV model fails to model the evolution of the model from 'virgin' to preconditioned state and hence the modeling of the Mullins-softening with the QLV model required additional modification i.e., the introduction of a softening variable.

As described in the aforementioned studies on QLV models, the AQLV model also fails to accurately predict triangular loadingunloading, if material properties are obtained from ramp-hold data (see Fig. 3.4).The deviation is observed to be larger during the loading phase than in the unloading phase, explaining the larger U_D, compared to experiments. Furthermore, although the AQLV model is able to model the strain history dependent behaviour i.e. the Mullins-type softening at a single strain level it was necessary to impose the condition that each strain level begun at time 0, to account for this effect at every strain level. Hence the full strain history of the experiment is not taken into consideration and each strain level is modelled individually. The material parameters of the model were obtained from previous incremental stress relaxation experiments and resulting peak model stresses had to be scaled by peak experimental stresses per strain level. A full relaxation of the sample between strain levels would be ideal. However, it is observed that following the peak stresses of each cycle for a given strain level showed a relaxation behaviour to a steady state. We observe that the model reset for each strain level showed a much better fit to the repeated cycles when set to each new strain level, due to this relaxation behaviour being sufficient. However, the peak stresses are not accurate since

they do not take that strain history into consideration. This is a limitation of the study and should be improved in future work. An additional cause may be attributed to the differences in preconditioning of the porcine muscle tissue as well as variations in the tissue samples due to age or sex of the animal. Theoretically, preconditioning is usually performed to overcome the effects of tissue handling or cutting. However, Carew et al. [26] showed that the preconditioned state of a tissue is not unique but a function of the strain history. Stress relaxation experiments were preconditioned by allowing samples to hang under its own weight for a period of 300s as performed by previous authors [69, 40].In contrast, for cyclic loading experiments, cyclic preconditioning was performed as described previously [47, 52].

These factors may therefore lead to deviations in the determination of peak stresses with the AQLV model. An alternative is to calibrate the material parameters of the AQLV model directly on triangular wave cyclic loading stress results.

Fracture toughness of porcine muscle tissue in this study is calculated using the mean U_{D} of both approaches. The fracture toughness determined from the experimental approach was 0.84±0.80 kJ/m^2 and from the AQLV model approach 0.71 ±0.76 kJ/m^2. Hence applying the mean value of U_{D} from both approaches produced fracture toughness results within the same order of magnitude with no significant difference (p=0.87). Sequentially, the proposed method might be reasonable used to determine the fracture response of other soft biological tissues.

In a study by Mayumi et al. [**?**], a similar approach consisting of using unnotched and notched samples to determine the fracture energy was used. Here bulk dissipation was separated from fracture energy in polymeric samples. The bulk dissipation is attributed to the viscoelasticity resulting from the breaking/healing of irreversible crosslinks of hydrogels. In this study, a special focus was placed on the change in fracture energy with varying loading rates. Our study did not consider the effect of strain rate on the fracture energy due to complexity but focuses on the use of increasing cyclic loads. Here cyclic loading is performed at the same strain level till a 'steady state'. This steady state should have negligible energy dissipation due to plastic processes, leaving the viscous dissipation energy. In our study, we purport that the estimated fracture energy contains both crack propagation energy and plastic energy.

Fracture toughness or tearing energy of various soft tissues has been investigated in a variety of previous studies. However, due to variability of test sample size, width and crack length and mode of fracture, all of which have been shown to have significant effect of fracture toughness measurements [140, 139], direct comparisons are often difficult. For example, Bircher et al. [17] noted that the fracture toughness of the tissue is related to the collagen fibre content. Bircher et al. [18] applied the term apparent tearing energy to describe fracture toughness in collagenous tissue samples due to its high dependence on initial sample length and determined tearing energy for bovine Glissons capsule (GC) to be 0.45 J/m^1 and for a collagen type 1 material (CCC) 0.021 J/m^1. Taylor et al. [140] determined an apparent toughness of 2.49 kJ/m^2 for porcine muscle tissue with tissue thickness ranging from 4 to 18 mm, whereby showed that the fracture toughness was

higher for smaller specimen dimensions. Chin-Purcell and Lewis [31] reported 0.14 and 1.16 kJ/m^2 for the measured fracture toughness of varying grades of articular cartilage. Based on this previous literature, results obtained in this study, 0.71 and 0.84 kJ/m^2, are within reasonable range for porcine muscle tissue and variations in toughness parameter for porcine muscle tissue are likely due to variations in location of tissues as well as dimensions of the specimens, age and sex of the animal [83].

3.5 Conclusion

In spite of the limitations, the AQLV model enables a reasonable estimation of the viscous dissipated energy in porcine muscle tissue at incremental strain levels. This in turn enables fracture toughness determination of tissue samples in a reasonable order of magnitude. Future work should, however, focus on optimizing the model parameters for a given tissue. This will enable usage of the AQLV model across varying testing scenarios and loading protocols. This knowledge will help to better understand the constitutive viscoelastic behaviour of SCTs and also enables replacement of testing unnotched specimens for fracture toughness determination with AQLV model simulations.

Appendix A. Theory

The foundation of this study was built up based on some fundamental concepts proven by previous authors. The concepts are described shortly and arranged in logical order to enable easy tracking.

- Tschoegl et al. [144] proved that the net energy stored over a loop in a steady state triangular pulse, i.e. an excitation with constant strain rate $\dot{\varepsilon_0}$ in the deformation half-cycle ($0 \leq t \leq T/2$) and $-\dot{\varepsilon_0}$ in the recovery half-cycle ($T/2 \leq t \leq T$) is zero, where T is the total time of a single pulse. Hence, only in the steady state, the area of the hysteresis loop i.e the energy of the loop W_{hys} represents the total energy dissipated in the material. Essentially for the following given relations in a single steady state pulse, the deformation half-cycle, the total energy W_{T} is given by :

$$W_{\text{T}} = \int_0^{T/2} \sigma(t)(\dot{\varepsilon}_0)dt \tag{3.9}$$

  where $\sigma(t)$ is the stress response with time. For the recovery half-cycle, the recovery energy i.e. storage energy W_{S} is defined as:

$$W_{\text{S}} = \int_{T/2}^{T} \sigma(t)(-\dot{\varepsilon}_0)dt \tag{3.10}$$

  and hence the hysteresis area is given by:

$$\begin{aligned} W_{\text{hys}} &= |W_{\text{T}}| - |W_{\text{S}}| \\ &= \int \sigma(t)\dot{\varepsilon_0}dt \end{aligned} \tag{3.11}$$

for the steady state, no net energy is absorbed over a complete cycle (see [144] for details), hence, the dissipated energy W_{D} is essentially:

$$W_{\mathrm{D}} = W_{\mathrm{hys}} = \int \sigma(t)\dot{\varepsilon_0} dt \tag{3.12}$$

- Yang et al. [165] discussed the stress response and energy dissipation of a linear viscoelastic material under isothermal periodic constant strain rate loading (triangular wave) for arbitrary times. The relation is applied to the generalized Maxwell model which has a continuous relaxation function ($G(t)$) described by :

$$G(t) = G_e + \int_{-\infty}^{\infty} G(\tau) e^{-t/\tau} d\ln\tau \tag{3.13}$$

where τ is the relaxation time, $G(\tau)$ designates the relaxation modulus and G_e represents the equilibrium modulus. Hence, for periodic strains of a triangular wave applied at arbitrary times, i.e. the loading and unloading ramp strains can be described by the following relations (as described by Yang et al. [165], the actual notation is adapted from Babaei et al. [11]):

$$\varepsilon(t) = \begin{cases} \dot{\varepsilon}_0 t = 2\varepsilon_0 \frac{t}{T}, & 0 \le t \le \frac{T}{2} \\ \dot{\varepsilon}_0 (T-t) = 2\varepsilon_0 \left(1 - \frac{t}{T}\right), & \frac{T}{2} \le t \le T \end{cases} \tag{3.14}$$

The stress response corresponding to the deformation and recovery half-cycles for a generalized Maxwell model for a sufficiently fast viscoelastic relaxation in which the material does not slack, the stress response can be given by:

$$\sigma(t) = \begin{cases} E_0 \dot{\varepsilon}_0(t) + \sum_{i=1}^{n} E_i \tau_i \dot{\varepsilon}_0 \left(1 - e^{(-t/\tau_i)}\right), & 0 \le t \le \frac{T}{2} \\ E_0 \dot{\varepsilon}_0(T-t) + \sum_{i=1}^{n} E_i \tau_i \dot{\varepsilon}_0 \left(2e^{\left(\frac{T-2t}{2\tau_i}\right)} - 1 - e^{\left(-\frac{t}{\tau_i}\right)}\right), & \frac{T}{2} \le t \le T \end{cases} \tag{3.15}$$

where E_0 is the elastic modulus of the solitary spring in the generalized Maxwell model and E_i elastic moduli of the springs in combination with dampers. The first term of the relation describes the equilibrium state of the stress response.

- Nekouzadeh et al.[104, 103] proposed the adaptive quasi-linear viscoelastic mode (AQLV) to overcome the inability of the Fungs QLV model, once calibrated at a specific strain level, to accurately describe the viscoelastic stress response at other strain amplitudes. The AQLV model is a constitutive model that relates stress σ to strain ε via a simple multiplication between the viscoelastic strain $V^{(\varepsilon)}(t)$ and a pure non-linear function of strain $k(\varepsilon(t))$. The AQLV model can be interpreted as a generalized Maxwell model with non-linear springs and dampers, specifically if exponential shape functions are chosen to describe the relaxation function $g_i(t)$. The AQLV model is given by :

$$\sigma(t) = k\Big(\varepsilon(t)\Big)\ V^{(\varepsilon)}(t) \tag{3.16}$$

$$V^{(\varepsilon)}(t) = \int_{-\infty}^{t} g(t-\tau)\dot{\varepsilon}(\tau)d\tau \tag{3.17}$$

where $g_i(t) = e^{-t/\tau_i}$ to represent the model in terms of parallel Maxwell elements, whereby the relaxation time τ_i is the ratio of the dashpot coefficient $b_i(\varepsilon(t))$ to the spring constants $k_i(\varepsilon(t))$, ($\tau_i = \frac{b_i}{k_i}$). Hence, the ramp stress response $\sigma_R(t)$ of the AQLV model is described by :

$$\sigma_R(t) = \sigma_0(\varepsilon(t)) + \sum_{i=1}^{M} k_i(\varepsilon(t))\dot{\varepsilon}_0\tau_i(1 - e^{-t/\tau_i}), \quad 0 \le t \le T/2 \tag{3.18}$$

where $T/2$ here refers to the time at the end of the ramp phase during a ramp-hold experiment.

- Babaei et al. [11] showed that the stress response of soft biological tissues under triangular wave excitation can be determined for various constant strain rates (2s, 20s, 200s) based on a quasi-linear viscoelastic (QLV) model. This shows that the quasi-linear viscoelastic framework can be applied to determine the energy dissipation in a viscoelastic material. The formulation is not the focus of this study and hence is not provided (see [11] for details).

- In the current study, the AQLV model is extended to describe the deformation and recovery half-cycle, and accounting for the strain level dependency of the model. For the applied strains in Equation 3.14.

$$\sigma(t) = \begin{cases} \sigma_0(\varepsilon(t)) + \dot{\varepsilon}_0 \sum\limits_{i=1}^{n} k_i(\varepsilon(t))\tau_i \left(1 - e^{(-t/\tau_i)}\right), \\ \qquad ...0 \le t \le \frac{T}{2} \\ \sigma_0(\varepsilon(T-t)) + \dot{\varepsilon}_0 \sum\limits_{i=1}^{n} k_i(\varepsilon(t))\tau_i \left(2e^{\left(\frac{T-2t}{2\tau_i}\right)} - 1 - e^{\left(-\frac{t}{\tau_i}\right)}\right), \\ \qquad ...\frac{T}{2} \le t \le T \end{cases} \tag{3.19}$$

Hence, the analytical solution to determine the hysteresis energy can be determined from the following analytical solutions Equations 3.9- 3.11 as follows:

$$W_D = \sum_{i=1}^{N} k_i(\varepsilon(t))\dot{\varepsilon}_0^2\tau_i^2 \left(-3 - \mathrm{e}^{-\frac{T}{a_i}} + 4\mathrm{e}^{-\frac{T}{2\tau_i}} + \frac{T}{\tau_i}\right) \tag{3.20}$$

CHAPTER 4

Paper 3

From manuscript:

Development of 3D printed tissue-mimicking materials: Combining fiber reinforcement and fluid content for improved surgical rehearsal

Othniel J. Aryeetey, Laszlo Jaksa, Martin Bittner-Frank, Andrea Lorenz, Dieter H. Pahr

Published: Materialia, 102088 April 2024

Abstract

The prevalence of medical errors during surgical procedures has led to a higher emphasis on improving surgical outcomes, by improving surgical planning and training. Anatomical models have become valuable tools for preoperative planning and current 3D printed models strive to better match real soft biological tissues. This study aimed to develop novel 3D printed material composites with controllable mechanical properties that mimic soft tissue. Concepts of microstructuring, fiber reinforcement and fluid infill in extrusion-based 3D printing are combined to design tunable materials towards target tissues of porcine muscle and liver. Material characterization was performed in triangular wave cyclic experiments under uniaxial tension with increasing displacements. Hereby, initial EI and final EII elastic moduli were evaluated. Further, the viscous response was characterized by the dissipated energy ratio UD and suture retention strength (SRS) was determined by single tensile pull-out tests Elastic moduli of printed materials were successfully tuned to 510 ± 10 kPa, closely resembling porcine muscle with 580 ± 150 kPa. The dissipated energy ratio UD of the silicone was increased from 0.09 ± 0.01 to 0.46 ± 0.17 by addition of

gyroid infill and viscous fluid. Suture retention strength (SRS) for porcine liver tissue was 1.64 ± 0.42 N, while that of 3D printed silicone showed a mean SRS of 5.1 ± 0.6 N. Although the exact properties of porcine muscle and liver tissue require finer tuning, this study established techniques for refinement of 3D printed tissue-mimicking materials, ultimately enabling more accurate models for surgical rehearsal.

4.1 Introduction

Recently, it has been suggested that 'medical errors' lead to a mean death rate of about 250,000 patients each year in the United States alone [86]. Hence, a higher emphasis has been placed on reducing patient mortality through improved surgical planning and training. The use of anatomical models in research, teaching and surgical rehearsal has therefore risen significantly in the past few decades [46].

Advancements in medical imaging technology have led to the emergence of higher resolution, non invasive imaging methods. Although these techniques are increasingly capable of capturing more intricate details of the anatomical structures within a patient's body, a two-dimensional portrayal of anatomy can obscure the complex spatial relationships between tissues [87]. 3D virtual models help here to visualize organs structures and enhance visualization and communication, they however, lack the tactile feedback necessary for surgical rehearsal and practice. Producing a 3D physical model of an individual's organ can significantly improve this aspect, offering a more tangible approach for medical professionals [116]. The advent of additive manufacturing, commonly referred to as 3D printing, along with improvements in image processing, has enabled complex patient-specific physical anatomical models to be developed [12, 123]. The use of 3D printed models has been shown to significantly improve the quality of pre-operative planning in terms of key feature identification, implant customization and intra-operative guidance and even patient communication [163, 154].

3D printed anatomical models have been implemented in many surgical fields [66]. In the field of neurosurgery, surgeries in the brain and spinal regions often require a high degree of accuracy [137]. 3D printing has been applied to creating various anatomical models, such as of a cerebral aneurysm using ABS and photoresins by Scerrati et al. [127] and more recently, neonatal anatomical model by Wagner et al. [153] using polyjet technology. In other fields, such as in Urology, resin printed prostate tumor models from Shin et al. [130] and Wang et al. [158] serve as additional examples. Other fields of medicine, where anatomical models have made an impact include cardiology [62, 51, 146, 152, 89], pulmonary medicine [58, 37, 59], hepatology [168, 50] and abdominal surgery [34, 132, 136] among others. The materials often used in these research papers, tend to be stiffer and less compliant than real soft biological tissue.

This led to the use of softer more compliant materials such as silicone and hydrogels [36, 77, 79], often combining indirect method such as molding, casting or injection with 3D printing [66]. Models of blood vessels are created by applying 3D printing to a sacrificial part which is later melted or dissolved away to create hollow structures [124, 78]. Maddox

et al. [84] created 3d printed renal units using multi-jet 3D printer to form the outer shell of the renal tissue and injected agarose gel solution into the inner cavity of the model in order to model more realistic patient-specific renal malignancies. Ishii et al. [61] created patient-specific liver model composed of 3 separate parts by firstly directly 3D printing blood vessels and shell of the liver and then printing the mold, followed by molding the parenchyma with soft polyurethane resin. The aim of these studies have been primarily to ensure that the mechanical properties of anatomical models are in the same order of magnitude as the target soft tissues. This is a clear trend showing the importance of the tactile response properties of anatomical models for surgical rehearsal. Although these combined direct and indirect methods tend to exhibit overall more realistic tissue behaviour, the mechanical properties of combined casted and 3D printed parts may be difficult to characterize accurately with conventional testing methods. Also the material properties created are often not easily tunable to better match other use cases.

Here, we propose a methodology for the creation of anatomical tissue models with tunable and measurable mechanical properties. The approach involves direct 3D printing of two types of silicones in combination with standard fused deposition modeling (FDM) printing. Tissues are printed with a controllable microstructure or 'infill', to tune the material's stiffness and viscous properties. A novel concept was applied to increase the material's viscous response under uniaxial cyclic loading by introducing a fluid silicone oil with high viscosity into the matrix of the designed sample. Additionally, stiff wavy fibres were printed directly into the matrix of the samples to tune the material' elastic response to a more non-linear responsetypical of soft tissue. This study is novel in that it combines fibre reinforcement, microstructuring and fluid infill in extrusion-based 3D printed materials to produce tunable tissue mimicking materials for the creation of anatomically accurate surgical rehearsal models.

4.2 Methods

4.2.1 Theory

Target tissues were selected to be porcine liver and porcine muscle as reference mechanical properties and due to the readily availability of these tissues for testing. Hepatic tissue is regarded as being homogenous and isotropic and one of the softer biological tissues[29] and hence served as a lower boundary of target tissues. Muscle tissues have been shown to be in the upper range of soft biological tissue stiffnesses,[134, 43, 6] and hence serve as the upper boundary of target tissues.

The main approach employs 3D printable condensation-crosslinking single component (1K) silicone materials as a base material for the tissue mimicking material (TMM). Addition of microstructuring or infill enables the control of material stiffness [53] and may introduce some viscoelastic responses [65, 4]. Elastomers display linear stress strain behaviour in the range of surgical manipulation (10% to 25%), whereas soft biological tissues have a non-linear stress-strain relationship [156]. Hence, a technique to introduce the strain softening behaviour of soft biological tissue into linear elastic polymer is the inclusion

of wavy fibre reinforcement in the matrix of the material, as seen in previous literature. This creates a controlled mismatch, such that the material stiffness is dominated at lower strains by the matrix and higher strains by the stiffness of the fibres [57, 160, 155, 49]. Soft biological tissues have been shown to have higher energy absorption .i.e. larger hysteresis under cyclic loading [7, 42] as compared to elastomers.Here, novel approach was developed to include silicone oil as a filler fluid is employed to increase the elastomers viscosity. In total, four major specimen groups were created and tested: Soft biological tissue, base silicones, i.e., with unaltered material properties, fibred samples and tuned samples. Three samples per specimen group were tested for repeatability and mean results with standard deviation are reported.

Elastic Stiffness tuning

Elastic tuning to change the non-linear elastic behaviour of the samples was performed by incorporating stiffening fibres into the silicon matrix. Wang et. al [155, 156] as well as by Garcia et al. [49] showed that the non-linear response of base polymeric materials can be tuned to achieve strain stiffening behaviour by embedding stiff wavy fibres in the soft polymeric material, given that these structures have the right design parameters. During loading the stiffer wave fibres are engaged once fully stretched and produce an increase in stiffness at a given strain range. This inflection region is characteristic of a given soft tissue that mimics the effect of collagen fibres within the soft tissue [161]. The increase in stiffness is dependent on the stiffness of the fibre, while the inflection region is based on the wavelength of the embedded fibres. In order to reduce the general stiffness of the material, the study focused on both the initial E_I and final $E_I I$ elastic moduli. The overall stiffness was lowered by introducing an infill pattern whilst printing, also reducing the overall material mass.

Viscous behaviour tuning

It has been shown that an increase in fluid content in soft biological tissue corresponds to a faster rate of relaxation and hence an increase in the dissipated energy [30, 16]. Viscous tuning aims to increase the energy dissipation by the tissue mimicking material under cyclic loading. To achieve this, a high viscous fluid, PDMS oil is introduced to the polymeric matrix to introduce a dampening effect.

Suture Retention Test

The suture retention strength (SRS) as defined by the AAMI/ISO/ANSI 7198 Standard (2016) as the anastomotic strength or "the force necessary to pull a suture from a prosthesis or cause failure in the wall of a prosthesis". Mine et al [93]showed that, depending on the breakage pattern for a biological tissue, a break starts much earlier than the maximum suture retention strength (SRS), this is referred to as the breaking start strength (BSS). The influence of the test design has been shown to also have a marked effect on the results of the suture retention test and hence test parameters were chosen with special

care considering the effect of suture bite size [141], location and suture size [110] and clamping [13].BSS and SRS of porcine liver tissue and a 3D printed sample were assessed in the current study.

4.2.2 Sample Preparation

Multi-material 3D printer

Samples were created using a custom-made multi-material 3D printer capable of printing two highly viscous fluids as well as a filament extrusion. The printer was developed using a modified Railcore II 300 ZL open-source 3D printer system with an extrusion-based extruder printhead composed of a Vipro-HEAD 3/3 two-component printhead (Viscotec GmbH, Toging am Inn, Germany). This enables processing two single-component silicones, or a two-component silicone in combination with a standard E3D V6 FFF printhead for depositing thermoplastic filaments (see Figure 1). A customized printing nozzle was designed to enable the use of various printer nozzle diameters.

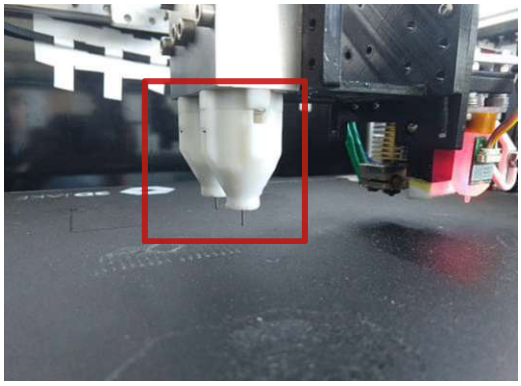

Figure 4.1: Custom-made multi-material 3D printer with a 2 component ViproHead printhead (Viscotec GmbH, Toeging am Inn, Germany) capable of printing in combination with standard E3D V6 FFF printhead.

The silicone printing nozzle is connected to the outlet of the extruder through a Luer-thread and is secured against unscrewing with a retainer part. These white Luer-adapters and retainers were custom-made for the extruder. A nozzle with 0.4 mm outlet diameter was selected for silicone extrusion. The original E3D V6 FFF printhead on the other side of the carriage is capable of melting and depositing thermoplastic filaments through a 0.4 mm diameter nozzle (see Figure 1). Accuracy of the 3D printed models was considered in terms of recommendation made in previous publication by Jaska et al. [63, 64] with regards to aspects such as recommended wall thickness, slenderness ratios, bridging lengths and overhang angles.

Materials

To create tissue mimicking specimens, three main material components were required. A 3D printable base material, a stiffening material component to mimic the strain stiffening effect of soft biological tissue, and a viscous fluid-like component for the tuning of viscoelastic mechanical properties.

Four single-component high viscosity, condensation-crosslinking liquid silicone rubber Elkem AMSil20101, AMSil20102, AMSil20103, AMSil20104 (Elkem Silicones SAS, Lyon, France) were tested for use as a base matrix. The selection was made primarily based on the ease of printability and curing of the material as well as the Elastic moduli of the silicones. To enable elastic tuning, two printable stiffer material components were tested. A standard polylactic Acid (PLA) fibre (Material4Print GmbH & co. KG, Loehne, Germany) and a more flexible Thermoplastic Urethane (TPU) filament, Varioshore Natural (ColorFabb B.V. Belfeld, Netherlands), each filament with a standard 1.75 mm diameter. The latter was printed at 210° C to activate the foaming expansion to decrease the fibre stiffness. For viscous tuning, a high dynamic viscosity (100 Pas) Polydimethylsiloxane (PDMS) oil (Optimal Products GmbH, Bad Oeynhausen, Germany) was selected as a fluid filler material. Additionally, the PDMS oil was mixed with 1 w/w% Silc Pig "Blood" paint (Smooth-On Inc., Macungie, PE). It was assumed that this coloring additive does not have a significant effect on the overall mechanical behavior of the PDMS oil, due to negligible weight amount. It was hypothesized that the fluid like nature as well as the inherent viscosity of the PDMS Oil would significantly increase the overall viscous response of the designed material.

Sample design

In this study, soft biological tissues, porcine muscle and liver tissue were prepared into rectangular shape 70 mm x 20 mm x 5 mm thick samples as previously described in [6] for cyclic uniaxial testing (see Figure 4.2 A). Initial tests were conducted on base silicone materials (Elk01, Elk02, Elk03, Elk04) as well as fibre reinforced samples (Elk01LF, Elk01MF, Elk01HF) using Type I dogbone samples in accordance with ASTM Standard D638-14 as shown in Figure 4.2.

Tuned concept specimens (G30, G30Fib, G30Flu, G30FibFlu) were designed based on the results of preliminary tests (see Table 4.1 for a description of all designed samples). In order to create cavities for the fluid infill, and prevent fluid loss during testing, the samples required an outer wall thickness of at least 1 mm. To mitigate the effect of thickened walls on the test results, the sample design was increased in width and thickness to 10 mm and 14 mm respectively, with a gauge length of 70 mm (see Figure 4.2B).

Tuned samples were created with gyroid infill structures using parametric CAD design tools, specifically Rhinoceros®and Grasshopper^{TM}, along with the Crystallon plugin. A basic CAD design of the dogbone sample was created in the Rhinoceros®CAD design environment and shelled to a thickness of 1.2 mm. The shell thickness defines the thickness of the printed wall. Using the Crystallon Plugin, the obtained cavity within

the shelled CAD object was filled with a gyroid structure, the minimum thickness of each gyroid was the print head nozzle diameter (0.4 mm) plus a tolerance of 0.1 mm i.e (0.5mm). The gyroids were patterned in x, y and z directions such that they filled a 30% volume of the CAD dogbone model, based on comparisons to Prusa Slicer infill volumes. A boolean operation was carried out to ensure that the internal gyroid structure conformed to the internal volume of the dogbone structure and outliers were removed. The internal cavity was then copied, to give an additional dogbone model with internal dimensions of the shelled CAD model. The internal dogbone was booleaned by the fitted internal gyroid structure to produce the negative volume which would serve as the negative space for fluid infill. The stiff wavy fibres were produced by a simple sinusoidal wave function line in Rhinoceros 7 plugin Grasshopper. A pipe function was applied to the line with a radius of 0.9 mm. Fibre structures were designed based on literature studies by Wang et. al [156, 155], which showed that a sinusoidal wave embedded in a soft polymeric material with a selected wavelength introduced strain stiffening behaviour. 3 main design parameters were considered, the wavelength of the fibre λ, the amplitude A and the radius of the fibre R_F. 3 types of fibres were designed. A High frequency fibre (HF) with λ=6 mm, A=3 mm, r_f=0.8 mm; a mid frequency fibre (MF), with λ=10 mm, A=3 mm, r_f=0.8 mm; and a low frequency fibre with λ=20 mm, A=3 mm, r_f=0.8 mm. PLA fibres were initially printed as reinforcement into Elk01 material and tested in uni-axial tension and later replaced by more flexible TPU fibres. 2 print layers (0.8 mm + tolerance (0.1 mm)were used to create the final fibre stls. The 3 stl files were combined and the fibre stl was boolean subtracted from all other components to create a cavity within the gyroid stl, the negative space and the dogbone structure. This allowed for the creation of both the base material's gyroid infill structure, equivalent to approximately 30% of internal sample volume, and the negative space volume, for the fluid filler, as separate stl files. This further enabled multi-material slicing using Prusa Slicer. The samples were labelled based on their constituents. G30 samples referred to 3 samples prepared with only the 30% 'empty' gyroid infill. G30Fib refers to 3 samples with a single fibre reinforcement, layered centrally in a gyroid structure. G30Flu refers to samples with PDMS oil as a fluid filler in the negative space of a similar G30 structure, whilst G30FibFlu contains both fibre reinforcement and fluid filler components.

4.2.3 Mechanical Testing & Analyses

Test protocol

Experiments were carried out using an electro-mechanical test machine (Zwickiline Z030, Zwick Roell GmbH, Ulm, Germany) operated at 10 Hz. A high resolution camera (Sony α-6400, Sony, Tokyo Japan) was used for optical video recording at 1 Hz.

White dot markers (GOM, Braunschweig, Germany) were placed slightly below the upper clamped region and above 15 mm from the bottom to avoid bell ends and ensure that the gauge area was vertical. These were used for optical strain tracking analysis with a point tracking algorithm described previously by Frank et al.[45]. Specimens were subsequently clamped on both ends (see Figure 2C).

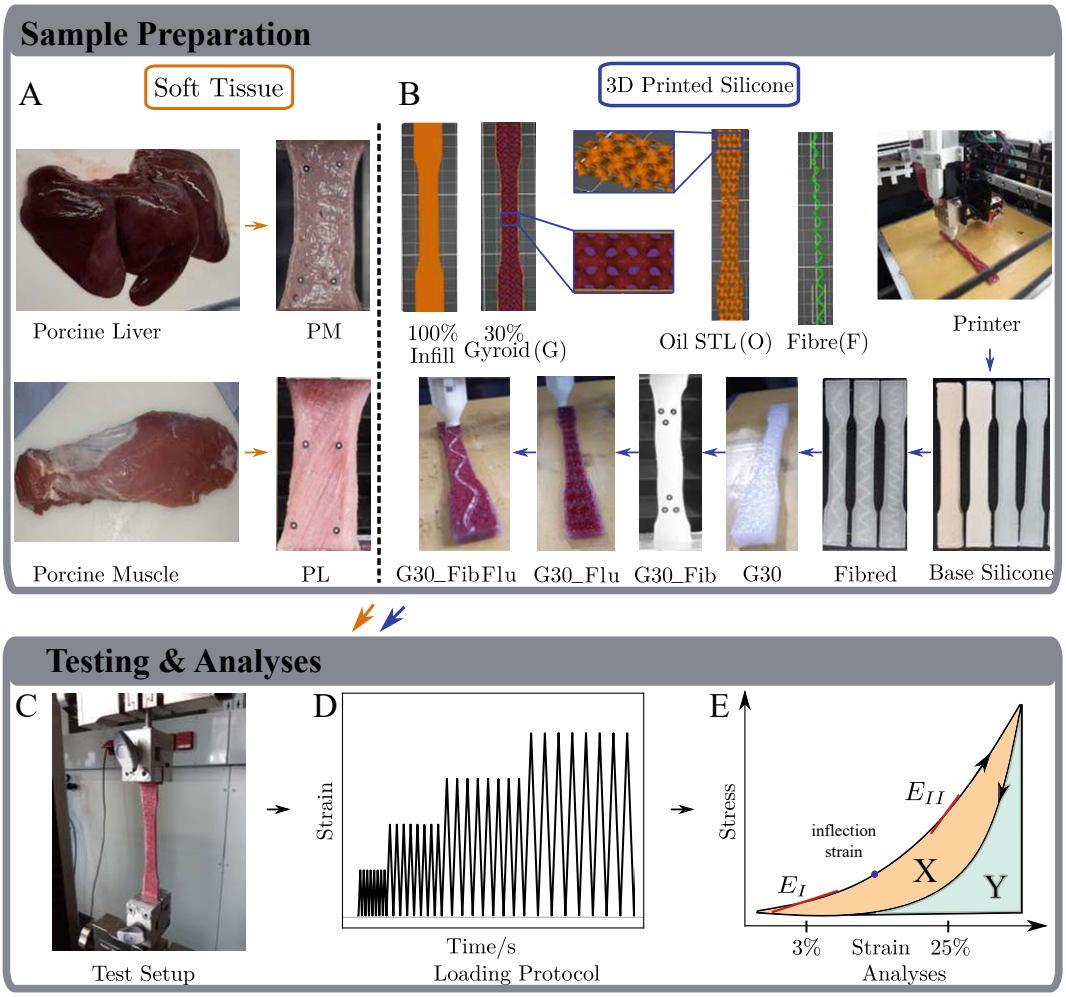

Figure 4.2: Flow chart showing the methodology of the study. A) Soft tissue section shows sample preparation of porcine muscle and liver tissue. B) 3D printed section shows the creation of tissue mimicking 3D printed silicone samples from design, printing to final samples. C) mechanical test setup. D) cyclic loading protocol. E) analyzed parameters, initial E_I and final E_{II} Elastic moduli,inflection strain ε_i as well as energy areas (X,Y).

Displacement-controlled, uniaxial tensile, triangular wave cyclic loading was applied at 1 mm/s with a preload of 5 mm on the samples with target strain levels (7.5%, 15.0%, 25% and 30% strain). Each strain level was cycled 8 times to ensure a steady state, the final cycles of each strain level were used to determine the hysteresis.

Suture Retention Tests

Additionally, suture retention experiments were performed on porcine liver tissue as well as on 3D printed silicone samples to assess the ability of the materials to hold sutures. For suture retention tests, rectangular samples were clamped on one end with a suture

Designation	Specimen Description		
	Composition	Fibre	Design Parameters
PM	Porcine muscle	N/A	N/A
PL	Porcine liver	N/A	N/A
Elk04	Elkem AMSil20104	N/A	N/A
Elk03	Elkem AMSil20103	N/A	N/A
Elk02	Elkem AMSil20102	N/A	N/A
Elk01	Elkem AMSil20101	N/A	N/A
Elk01HF	Elk01 + high-frequency fibre	PLA	λ=6, A=3, r_f=0.8 mm
Elk01MF	Elk01 + mid-frequency fibre	PLA	λ=10, A=3, r_f=0.8 mm
Elk01LF	Elk01 + low-frequency fibre	PLA	λ=20, A=3, r_f=0.8 mm
G30	Elk01 with infill pattern	N/A	30% gyroid pattern
G30Flu	G30 + fluid filler	N/A	30% gyroid + Silicone Oil
G30Fib	G30 + LF fibre	TPU	λ=20, A=3, r_f=0.8 mm
G30FibFlu	G30 + LF fibre + fluid filler	TPU	λ=20, A=3, r_f=0.8 mm

Table 4.1: Produced material sample acronyms and description.

material pulled through the a notch on the free edge. The notch is created with a suture needle and hence the notch size is dependent on the needle size. This is referred to as the suture bite. The suture bite depth is the distance from the free edge of the specimen (a_b) that shall amount to 2 mm as per the standard. The suture is tied off and pulled with a speed (v) of 1mm/s. Coated vicryl (polyglactin 910), dyed, braided sutures (Ethicon, New Jersey, USA) were used. Suture bite size of 3 mm was made with a 1/2 circle (rounded) tapered needle. Suture thread thickness was 3 mm and suture length 70 cm (see Figure 4.3). The specimens were tested with displacement controlled tensile pull test. The breaking start strength (BSS) as well as the suture retention strength (SRS) were measured and reported.

Stress and Strain determination

Actual sample strains were obtained via digital image correlation (DIC). Hereby, the position of the markers is tracked over time and the relative displacement between the marker positions at the top and bottom is determined. Hence, engineering strain is computed as:

$$\varepsilon(t) = \frac{l(t) - l_0}{l_0} \tag{4.1}$$

where l_0 is the initial length (at zero-force) and $l(t)$ the actual length of the tissue. The uni-axial linear engineering stress (σ) is calculated from the axial measured force (f) and the cross sectional area ($A_0 = B \cdot T$), measured with a calliper (prior to testing) and

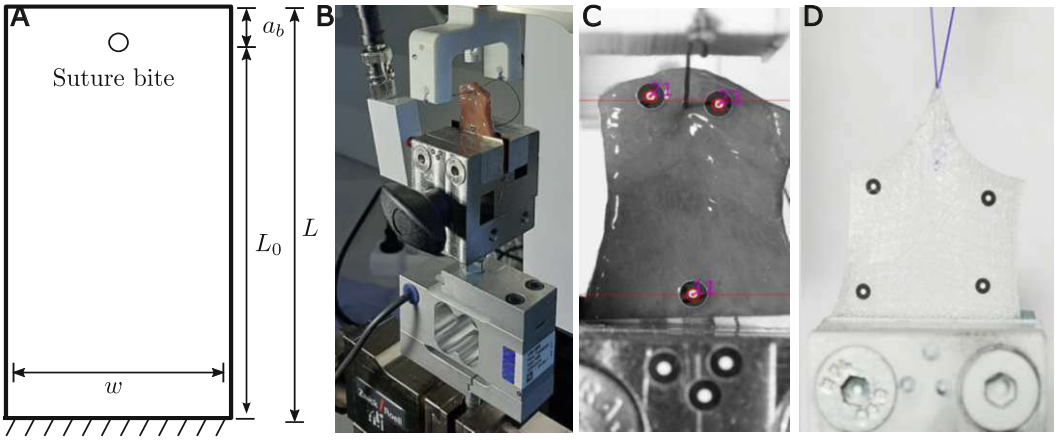

Figure 4.3: A)Suture retention test geometry showing suture bite depth (a_o), distance to clamp (L_o) and width(w) B) Mechanical test setup for suture retention C) Porcine liver tissue suture retention test setup showing DIC tracking D) 3D printed silicone sample under suture testing

averaged at 3 positions, using the following equation:

$$\sigma(t) = \frac{f(t)}{A_0} \tag{4.2}$$

Energy dissipation determination

The samples were tested in a cyclic manner and the non-linear elastic behavior was analyzed based on the initial and final Young's moduli values at the start and end regions of the material behaviour E and the inflection strain region ε_i. The dissipated energy ratio U_D was calculated as done previously by Aryeetey et. al [7]. The total energy W_T of the triangular wave cycle is the area under the loading half cycle i.e. area (X+Y) in Figure 4.2E), while the storage energy i.e. elastic energy W_S is the area under the unloading half cycle, i.e. area Y in Figure 4.2E. The dissipated energy W_D is the area between the loading and unloading half cycles, area X. The dissipated energy ratio, U_D as defined by Oyen et al. [109] is given by:

$$U_{\mathrm{D}} = \frac{W_{\mathrm{T}} - W_{\mathrm{s}}}{W_{\mathrm{T}}} = \frac{(X+Y) - Y}{(X+Y)} = \frac{W_{\mathrm{D}}}{W_{\mathrm{T}}} \tag{4.3}$$

Data representation

The material parameters measured E_I, E_{II} and U_D for each specimen type were obtained individually for all 3 samples of the specimen type. For each specimen type, the mean value of the 3 samples were obtained as well as the standard deviation over the 3 samples.

4.3 Results

4.3.1 Non-linear elasticity

Base material selection

Porcine muscle and liver tissue both showed typical non-linear elastic material behaviour characteristic of soft collagenous tissues. The porcine muscle tissue showed a mean measured stiffness and standard deviation of E_I of 10 ± 4.0 kPa within the 3% to 5% strain range with an increase to a mean final stiffness E_{II} of 580 ± 150 kPa between 15% to 25% strain range. Similarly, a rise in the stiffness of softer porcine liver tissue was observed, showing mean initial stiffness E_I of 3.0 ± 1.0 kPa with a final stiffness E_{II} of 38 ± 21 kPa (see Figure 3A).

All 3D printed base materials (Elk01 - Elk04) displayed a linear elastic response. The initial and final stiffnesses were relatively similar mostly showing a slight decrease in the final stiffness (see Figure 3B). The Elk01 material showed the lowest stiffness (140 ± 21 kPa), closest to the chosen soft biological materials and was therefore selected for further testing and tuning. Details of all stiffness results are reported in Table 4.2. The elastic moduli E_I, E_{II} of all tested samples are exhibited in Figure 4.5.

Effect of fibre reinforcement on elastic behaviour

The effect of the fibre reinforcement design was evaluated based on the results of the non-linear response in terms of initial and final elastic modulus E_I and E_{II} and inflection strain ε_i. The fibre reinforcement with varying wavelengths were tested with the aim to result in a strain stiffening behaviour. Only the low-frequency fibre sample (Elk01LF) accomplished this behaviour, whereas the mid- and high-frequency fibre sample still indicated a strain softening behaviour, similar to the bulk material (see Figure 4.4 and Table 4.2). There was no clear inflection in the high-frequency sample, and an inflection at 12% and 15% was observed for the mid- and low-frequency samples, respectively.

The non-linear elastic response of Elk01LF was similar to that of porcine muscle tissue, however with a higher initial stiffness E_I of 350 ± 20 kPa but a similar final Elastic modulus E_{II} of 520 ± 50 kPa. Further, initial stiffness E_I was increased in all fibre reinforced samples, with respect to the bulk Elk01 material. Taken together, the low-frequency wave design parameters showed the most promising results in terms of non-linear behaviour and inflection strain ε_i and were hence implemented in final samples G30Fib and G30FibFlu.

Effect of gyroid pattern and fluid infill on elastic behaviour

Figure 4.6 shows the stress strain response of Elk01 base silicone, Elk01 with 30% gyroid infill pattern (G30), and Elk01 with PDMS Oil as a fluid filler (G30Flu), as well as porcine muscle and porcine liver tissue. Reducing the infill percentage from 100% in Elk01 to G30 sample showed a reduction in initial modulus E_I from 140 ± 30 kPa to

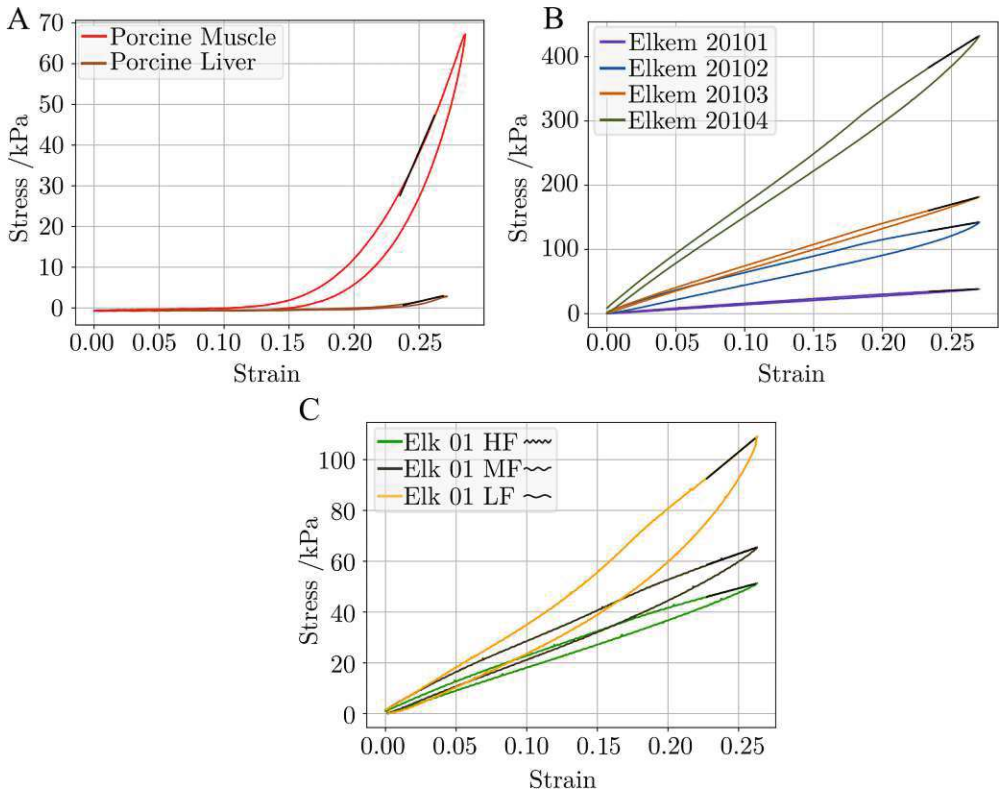

Figure 4.4: Selected stress strain plots showing the material behaviour of A) porcine muscle and liver tissue. B) Base silicones Elkem 20101- Elkem20104 3D printable base materials. C) Fibred Elk01 samples with sinusoidal fibres of high-, mid- and low- frequency (HF, MF, LF).

	Muscle	Liver		
E_I / kPa	10 ± 4.0	3 ± 1.0		
E_{II} /kPa	580 ± 150	38 ± 21		
	ElkHF	ElkMF	ElkLF	
E_I /kPa	260 ± 20	330 ± 30	350 ± 30	
E_{II}/kPa	180 ± 40	240 ± 30	520 ± 50	
	Elk01	Elk02	Elk03	Elk04
E_I /kPa	140 ± 20	780 ± 60	860 ± 80	1900 ± 70
E_{II} /kPa	175 ± 30	520 ± 40	690 ± 90	1800 ± 50

Table 4.2: Initial and final elastic moduli ± mean standard deviation for soft biological tissue, Elkem base silicone samples and fibred samples.

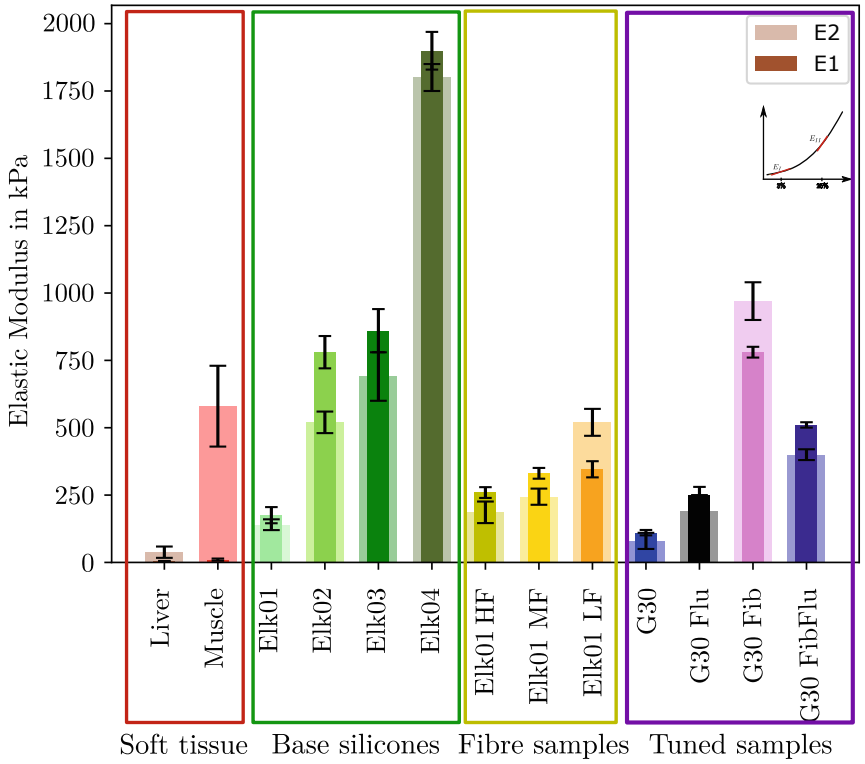

Figure 4.5: Initial mean Elastic modulus E_I (darker shade) and final mean Elastic moduli E_{II} (lighter shade) with standard deviation of 3 tested specimens per specimen concept.

110 ± 10 kPa as well as in the final elastic modulus E_{II} from 175 ± 20 kPa to 80 ± 30 kPa. Adding PDMS oil (G30Flu) increased E_I to 250 ± 30 kPa and E_{II} to 190 ± 60 kPa, still lower than the base material Elk01 (see Table 4.3).

	G30	G30Flu	G30Fib @12%	G30FibFlu @12%
E_I/kPa	80 ±30	190 ±60	970 ±70	400 ± 20
E_{II}/kPa	110 ± 10	250 ±30	780 ± 20	510 ±10

Table 4.3: Table showing the dissipated energy U_D, mean ± standard deviation for mechanically tuned samples

G30Fib showed an initial Elastic modulus E_I of 780 ± 20 kPa and final elastic modulus E_{II} of 970 ± 70 kPa at 12% strain with the inflection strain ε_i at ≈ 7% (see Table 4.3). Adding the PDMS oil to the fibre reinforced gyroid samples(G30FibFlu) still demonstrated an inflection strain ε_i of ≈ 7%. Initial and final stiffness was lowered to 510 ± 10 kPa and 400 ± 20 kPa, respectively (see Table 4.3 and Figure reffig:E2 for an overall comparison of all samples).

Testing performed on fibre reinforced samples displayed characteristics of damage during cyclic testing for cycles with strain levels above 14% strain. The observed delamination

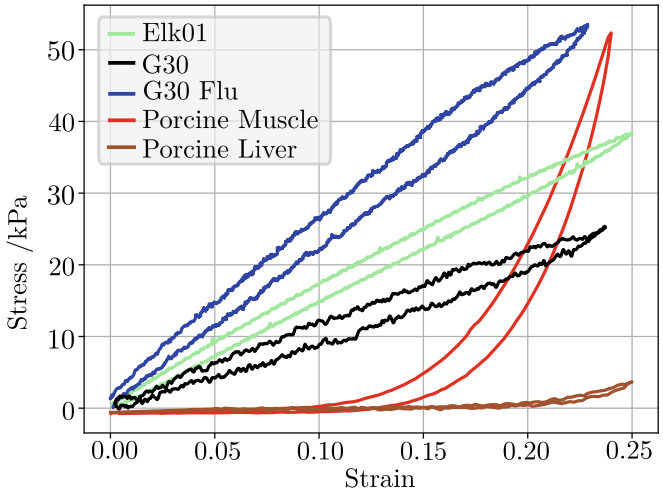

Figure 4.6: Stress strain plot of Elkem 20101 base silicone (Elk01) in green, Elkem 20101 with 30% gyroid infill pattern (G30) in black, and Elkem 20101 base material with PDMS Oil as a fluid filler (G30Flu) in blue as well as porcine muscle and porcine liver tissue in red and brown respectively.

occurred at the clamping regions (see Figure 4.9). Results for cycles below this threshold were therefore reported.

4.3.2 Suture retention tests

Additional suture retention tests were performed primarily on porcine liver tissue and 3D printed Elk01 samples with 30% gyroid infill to assess the capability for anatomical models. For porcine liver tissue, an early failure point (BSS) was observed. The mean BSS over 3 tested samples were determined to be 0.71 ± 0.08 N. The mean suture retention strength of porcine liver tissue measured over 3 samples was 1.64 ± 0.42 N, while for 3D printed silicone samples showed a mean suture retention strength of 5.1 ± 0.6 N with no obvious early failure point observed. Representative samples were selected and are shown in Figure 4.7.

4.3.3 Dissipated energy ratio

Material Selection

The dissipated energy ratio of the various samples was calculated as described in the methods section Equation III. Base materials showed varying hysteresis behaviour based on their chemical composition. Elk01, Elk03, and Elk04 showed relatively low energy dissipation with U_D of 0.09 ± 0.01 and 0.05 ± 0.02, and 0.06 ± 0.01, respectively (see Figure 4.8 and Table 4.4). Elk02 showed higher energy dissipation with 0.21 ± 0.02 much like porcine muscle and liver tissue samples. Elk02 was however not selected for further tuning due to the higher initial stiffness range. Further, as already demonstrated in Figure 4.4, the selected base material Elk01 and applied elastic tuning concept Elk01LF

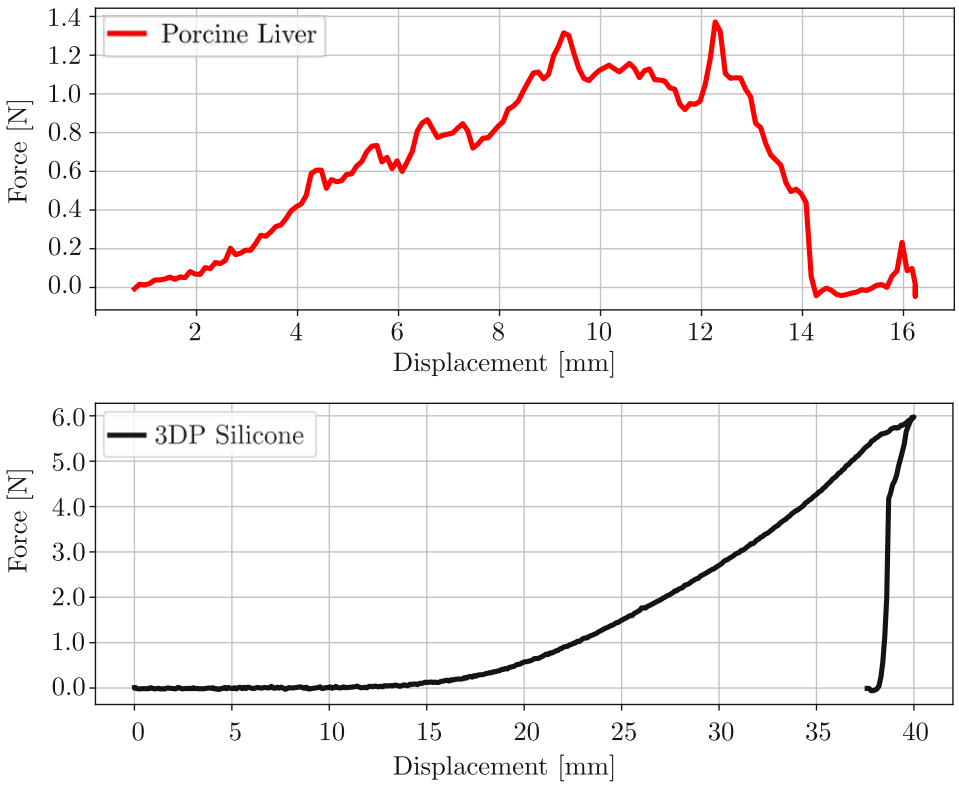

Figure 4.7: Representative force-displacement results of suture retention test in porcine liver tissue (top) and 3D printed Elk01 with 30% gyroid infill (bottom).

already indicated a similar energy dissipation ratio to biological tissue (see also 4.6), hence was selected for further material tuning.

	Muscle	Liver		
U_D	0.24 ± 0.04	0.15 ± 0.12		
	ElkHF	ElkMF	ElkLF	
U_D	0.11 ± 0.02	0.16 ± 0.02	0.17 ± 0.05	
	Elk01	Elk02	Elk03	Elk04
U_D	0.09 ± 0.01	0.21 ± 0.02	0.06 ± 0.01	0.05 ± 0.02

Table 4.4: Mean dissipated energy ratio U_D ± standard deviation for biological tissue, Elkem base silicone samples and fibred samples.

Effect of Fluid filler

The Elk01 with 'empty' 30% gyroid infill (G30) was compared initially to the 100% filled Elk01 samples and showed an increase in the dissipated energy ratio UD from 0.09 ± 0.01 to 0.16 ± 0.03. The samples filled with PDMS Oil (G30Flu samples) were observed to have an even further increase in U_D to 0.23 ± 0.05. These results are similar to dissipated

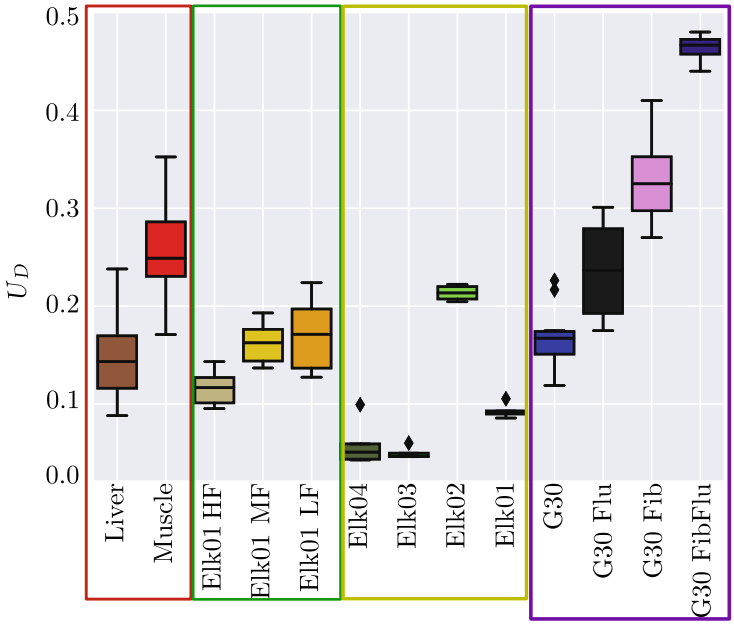

Figure 4.8: Boxplots showing the dissipated energy ratio U_D of all materials tested.

energy ratio results obtained from porcine muscle tissue of 0.24 ± 0.04. U_{D} of the samples are measured at the 8th and final cycle of the triangular wave excitation per strain level. The values are compiled over all 3 specimens of a sample type and box plots (see Figure 4.8 show the spread of the results per specimen type. The dissipated energy ratio U_{D} for the tuned sample G30Fib showed an increase to 0.31 ± 0.03 compared to Elk01, G30, G30Flu. A further increase in U_{D} is observed with G30FibFlu (0.46 ± 0.17) with the additional component of PDMS oil. Taking a closer look in Figure 4.9 demonstrated that samples of G30Fib and G30FibFlu indicated a permanent deformation as stress values become negative after unloading to 0% strain.

	G30	G30Flu	G30Fib @12%	G30FibFlu @12%
U_{D}	0.16 ± 0.03	0.23 ± 0.05	0.31 ± 0.03	0.46 ± 0.17

Table 4.5: Table showing the mean dissipated energy U_{D} ± standard deviation for mechanically tuned samples

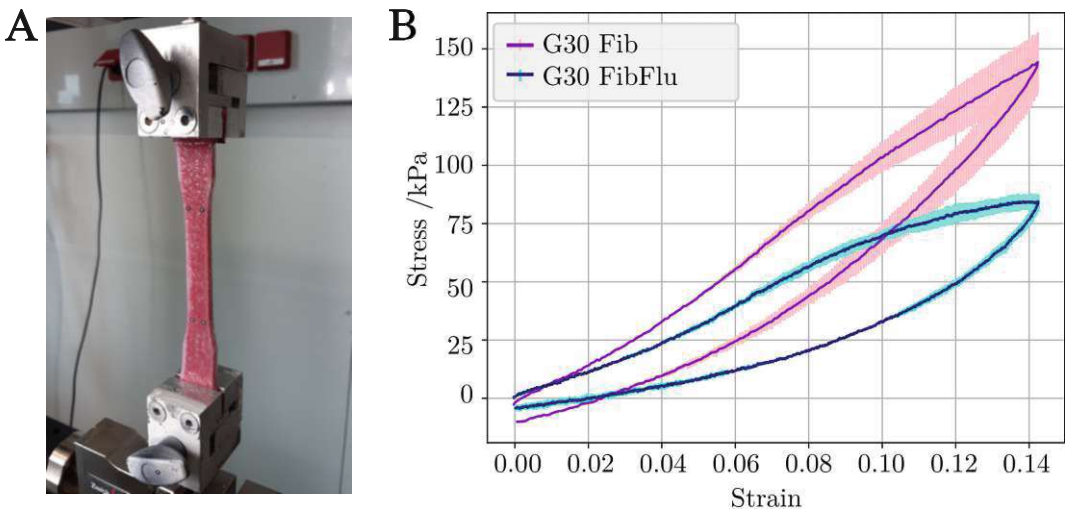

Figure 4.9: A) Image of G30FibFlu undergoing uniaxial tensile loading B) Stress strain of samples G30Fib (base material with sinusoidal fibre) and G30FibFlu (base material with sinusoidal fibre and PDMS oil fluid) showing the effect of mechanical tuning with addition of fluid.

4.4 Discussion

In this study, extrusion-based 3D printable polymeric materials were tuned to mimic soft biological tissue using a combination of microstructuring, fibre reinforcement and fluid infill and compared to two target soft tissues, porcine liver and porcine muscle tissue.

Results of the final elastic moduli E_{II} of porcine liver tissue (38 ± 21 kPa) in our study fall within the range of values reported in literature previously [77, 7, 101]. Porcine muscle elastic moduli values reported in our study (580 ± 150 kPa), are also within values reported in literature [150, 134, 106]. Qiu et al. [118] suggests that the range of strains during surgical manipulation is between 0% and 15% and hence reported initial E_I and final elastic moduli are selected within this range.

Elastic tuning involved the reduction of the elastomers overall stiffness as well as the introduction of non-linear stress stain behaviour in the otherwise linear elastic base material. The chosen base material (Elk01) showed similar stiffness properties to more flexible commercially available print materials flexible materials such as the Tango family from Stratasys, and materials from Ninjatek or PolyFlex, with elastic moduli within the range of 102 kPa and 104 kPa [167, 72, 76, 22]. The introduction of a gyroid microstructure to the base Elk01 base material reduced the materials overall final stiffness from 175 ± 30 kPa to 110 ± 10 kPa as hypothesized. This is mainly due to the reduction in the sample's density. Sinusoidal wave fibres (PLA and TPU) were printed into the polymeric matrix and successfully introduced a non-linear elastic behaviour to the sample. As expected, the mismatch of silicone matrix and fibre stiffness introduced an inflection point in the stress strain relationship. The design of the wavy fibre whether high-frequency, mid or low- frequency impacted the inflection strain, while the fibre material affected

the stiffness increase after inflection. This concept introduces control to the non-linear stress strain response of polymeric tissue substitutes and hence enables tuning of various materials towards specific collageneous soft tissue. Comparing to previous literature, the strain at the inflection point was higher than those shown by Wang et al. [156] for similar sinusoidal wave fibre reinforcements which was about 5%. However the chosen materials showed a stiffness range of 1 order of magnitude higher than in those in our study. Garcia et al. [49] also applied similar wavy fibre techniques and successfully introduced non-linear elastic material response for an ascending aorta model. The stiffness response of designed samples were between 360 kPa and 600 kPa.Hence, our current study was able to mimic soft collagenous tissue in terms of stiffness inflection strain ε_i more realistic.

In terms of viscous tuning, samples with fibre reinforcement also exhibited an increase in the dissipated energy ratio U_D, from the base material value of 0.09 ± 0.01 increasing with fibre frequency from Elk01HF (0.11 ± 0.02), to Elk01LF (0.17 ± 0.05). This is attributed to increased energy absorption of stiffening fibres. This finding is consistent with results expressed by Garcia et al. [49], who showed an increase in dissipated energy in the composite material ($\approx 40\%$) as compared to the single Tango Plus material ($\approx 35\%$). Additionally, it is observed that the introduction of the gyroid microstructure creates an increase in U_D (0.16 ± 0.03). It is hypothesized that the specific infill percentage and distinct pattern of gyroid voids may contribute to energy dissipation within the sample by redistributing stresses or creating zones of localized deformation.

Suture retention tests were performed on both porcine liver tissue and an equivalent G30 sample designed for suture retention tests. Only porcine liver tissue was tested for suture retention as it forms the lower boundary of our experiments and hence is the minimum value for comparison to 3D printed sample. Porcine liver tissue BSS and SRS results were consistent with literature results [18]. Bircher et al. performed suture retention tests on bovine liver tissue. BSS for bovine liver tissue was about 1.1 N and is consistent with our study of porcine liver tissue (0.71 ± 0.08 N) as porcine liver tissue has been shown to be softer [40]. SRS of G30 equivalent sample (5.1 ± 0.6 N) was considerably higher than that of porcine tissue (1.64 ± 0.42 N) mainly attributed to the materials higher stiffness properties as compared to soft porcine tissue. Results show that the 3d printed samples show sufficient suture retention strength to withstand manipulation during surgical procedures.

In the present study, the novel concept of introducing a fluid filler (PDMS oil) directly into the sample was used to tune the viscous response. PDMS oil was added as a filler material due to its high viscosity (100 Pas). Addition of PDMS oil showed a further increase in U_D, up to 0.23 ± 0.05. The contribution to the increased dissipated energy ratio is initially attributed to the fluid viscosity but may extend beyond this. The contribution to the increased dissipated energy ratio was initially attributed to the fluid viscosity. However, the effect of shear thinning behaviour might also contribute to the energy dynamics of the designed tissue samples and should be studied further. The U_D values obtained however were directly comparable to those of porcine muscle tissue. The final elastic modulus E_{II} of G30Flu sample rose to 190 ± 60 kPa, due to an increase

in overall sample density,but however did not match that of porcine muscle tissue (580 ± 150 kPa). The G30Fib sample showed an increase in U_D (0.31 ± 0.03) as compared to the G30 (0.16 ± 0.03) and is consistent with the hypothesis that fibre reinforcement increases energy dissipation. The inclusion of PDMS oil i.e. and G30FibFlu samples showed a further increase in U_D(0.46 ± 0.17) attributed to the contribution of both fibre reinforcement and fluid infill to energy dissipation within the sample.

Known limitations of the study are noted. The addition of the PDMS oil to the fibre reinforced gyroid sample showed an unexpected reduction in stiffness (400±20 kPa) as compared to G30Fib (780 ± 20) at the maximum attainable strain at 12 %(see Figure 4.9). This is mainly attributed to small leakages of viscous oil during testing around the clamping region. Another limitation was the damage (partial delamination) occurring in the stress strain plots for strains above 15 % for fibre reinforced G30Fib and G30FibFlu samples. This is attributed to damage of the sample around clamping regions at higher strains, verified by optical inspection after testing. These limitations can be avoided in future studies by increasing the wall thickness of the samples in order to prevent damage to clamping zones. Despite these limitations, the G30FibFlu sample showed an increased viscosity as well as non-linear elastic behaviour in cycles prior to damage cycles as anticipated. The concepts of combining microstructuring, fibre reinforcement and fluid infill to tune tissue mimicking materials mechanical response could thus be clearly demonstrated.

There are several advantages of using such 3D printed phantoms over direct usage of animal samples such as porcine tissue. Firstly, samples digitally created and hence are more reproducible compared to animal soft tissue which may show quite a large variation in mechanical properties depending on based on sex, age and species of the animal[5]. Another major advantage is the ability to further adapt the properties by slight changes in stiffness, non-linear response and energy dissipation as shown in this study for use in other clinical contexts such as in tumor research [23, 58]. The use of 3D printed samples can be adapted to use non-toxic substances which are then safer to use as compared to the preparation of samples from animal sources which may contain allergens or pathogens [95].

The results show that it is possible to tune mainly elastic polymeric materials towards soft biological tissues (non-linear elasticity and increased viscosity) within the range of their physiological stresses.Although porcine muscle and liver tissue could not be reproduced exactly, it is shown that the combination of adding fibres and fluid can be successfully used to tune polymeric base materials close to soft collagenous tissues. Further, the presented mechanisms serve as base tuning concepts that can be further refined and tuned to match a specific tissue by altering the design parameters.

4.5 Conclusion

This study showed that the mechanical properties, such as non-linear elasticity and viscoelasticity of polymeric base material, can be tuned by combining fibre reinforcement

and fluid infill to create tissue mimicking materials. Hereby, a wide range of stiffnesses (80 - 970 kPa) was achieved and energy dissipation of materials was raised by $\approx$ 40 % using microstructuring and fluid infill. Developed materials also exhibited an adequate suture retention strength (5.1 $\pm$ 0.6 N) and hence showed the capacity for use as anatomical phantoms. In future studies, further analysis of infill structures, as well as material properties of viscous fluid infills, will be carried out to create more fine-tuned materials. Also, computational models might be interesting to predict the stress-strain behaviour of those materials to overcome the limitation of physical printing and testing several sets of parameter compositions. Taken together, the basic tools necessary for the development of actual tissue mimicking materials, covering several mechanical aspects at once, have been made available to enable future development of surgical rehearsal anatomical models.

CHAPTER 5

Synthesis & Outlook

5.1 Synthesis

This dissertation advances the development of realistic anatomical models for surgical rehearsal by characterizing the mechanical properties of both soft biological tissues and tissue-mimicking materials. The research addresses three key areas:

- Constitutive Modeling: The study applies the reduced parameter AQLV (Adaptive Quasi-Linear Viscoelastic) model to capture the complex nature of soft biological tissues. This approach reduces the number of required experiments and material parameters while maintaining accuracy, facilitating easier comparison between various tissues and materials.

- Fracture Toughness: The research accounts for energy dissipation due to viscoelastic and plastic processes when determining the fracture toughness of soft biological tissues. The AQLV model parameters, applied to uniaxial tensile loading experiments, provided reasonable estimations of energy dissipation and fracture toughness, demonstrating the potential of flexible strain-dependent constitutive models in surgical applications.

- Tuning Mechanical Properties: A proof-of-concept study developed techniques to tune the mechanical properties of polymeric materials. By introducing microstructures/infill and stiff wavy fibers, the research achieved reduced material stiffness and non-linear elastic response mimicking collagenous tissues. The addition of viscous fluid to internal cavities increased viscoelastic response, creating a versatile approach applicable to various soft tissues and 3D printing technologies.

5.2 Future Outlook

The concepts discussed in Chapter 2 viscoelastic modeling, i.e. the reduced parameter AQLV can be applied to other soft biological tissues, or more specifically to human tissue. The current study was run with porcine tissue to serve as a validation, however ideal would be to apply these concepts to soft human tissue. This can aid in characterizing soft tissues with an objective measure towards the goal of surgical rehearsal as well as for further simulations.

Chapter 3 determined the viscous energy dissipation during soft tissue fracture and estimated the fracture toughness parameter. The model did not fully account for the complete strain history with each strain increase, potentially affecting result accuracy. Additionally, it overlooked effects like plastic deformation in calculating fracture energy. Future work should incorporate full strain history and distinguish other complex physical effects during tissue fracture.

Chapter 4 introduced methods for creating tissue, including microstructuring, fiber reinforcement, and fluid content to mimic mechanical responses of soft tissue. Further refinement of these models is needed to more accurately match specific tissues. Utilizing computational engineering and simulations could accelerate this fine-tuning. Additionally, experimenting with various silicone bases, infill types, and fluid viscosity may enable the development of different tissue-mimicking materials, matching the mechanical properties of actual biological tissues even closer.

List of Figures

List of Tables

Bibliography

[1] G. A.A. The phenomena of rupture and flow in solids. *philos.Trans. R. Soc. Lond.*, A 221:163–198, 1920.

[2] N. Abolhassani, R. Patel, and M. Moallem. Needle insertion into soft tissue: A survey. *Medical Engineering & Physics*, 29(4):413 – 431, 2007.

[3] S. D. Abramowitch and S. L. Woo. An improved method to analyze the stress relaxation of ligaments following a finite ramp time based on the quasi-linear viscoelastic theory. *Journal of biomechanical engineering*, 126:92–7, Feb 2004.

[4] A. Abusabir, M. A. Khan, M. Asif, and K. A. Khan. Effect of architected structural members on the viscoelastic response of 3d printed simple cubic lattice structures, 2022.

[5] G. A.I. Arroyave, R. G. Lima, P. A. L. S. Martins, N. Ramião, and R. M. N. Jorge. Methodology for mechanical characterization of soft biological tissues: Arteries. *Procedia Engineering*, 110:74–81, Jan. 2015.

[6] O. J. Aryeetey, M. Frank, A. Lorenz, S.-J. Estermann, A. G. Reisinger, and D. H. Pahr. A parameter reduced adaptive quasi-linear viscoelastic model for soft biological tissue in uniaxial tension. *Journal of the Mechanical Behavior of Biomedical Materials*, page 104999, Dec. 2021.

[7] O. J. Aryeetey, M. Frank, A. Lorenz, and D. H. Pahr. Fracture toughness determination of porcine muscle tissue based on aqlv model derived viscous dissipated energy. *Journal of the Mechanical Behavior of Biomedical Materials*, 135:105429, 2022.

[8] O. J. Aryeetey, L. Jaksa, M. Bittner-Frank, A. Lorenz, and D. H. Pahr. Development of 3d printed tissue-mimicking materials: Combining fiber reinforcement and fluid content for improved surgical rehearsal. *Materialia*, 34:102088, 2024.

[9] T. Azar and V. Hayward. Estimation of the fracture toughness of soft tissue from needle insertion. In F. Bello and P. J. E. Edwards, editors, *Biomedical Simulation*, pages 166–175, Berlin, Heidelberg, 2008. Springer Berlin Heidelberg.

[10] B. Babaei, S. D. Abramowitch, E. L. Elson, S. Thomopoulos, and G. M. Genin. A discrete spectral analysis for determining quasi-linear viscoelastic properties of biological materials. *Journal of The Royal Society Interface*, 12(113):20150707, Dec. 2015.

[11] B. Babaei, A. Velasquez-Mao, K. M. Pryse, W. B. McConnaughey, E. L. Elson, and G. M. Genin. Energy dissipation in quasi-linear viscoelastic tissues, cells, and extracellular matrix. *Journal of the mechanical behavior of biomedical materials*, 84:198–207, 2018.

[12] S. R. Barber, S. Jain, Y.-J. Son, and E. H. Chang. Virtual functional endoscopic sinus surgery simulation with 3d-printed models for mixed-reality nasal endoscopy. *Otolaryngol Head Neck Surg*, 159(5):933–937, Nov 2018.

[13] L. Bernardi, E. Mazza, and A. E. Ehret. The effect of clamping conditions on tearing energy estimation for highly stretchable materials. *Engineering Fracture Mechanics*, 188, Sept. 2017.

[14] L. Bernardi, E. Mazza, and A. E. Ehret. The effect of clamping conditions on tearing energy estimation for highly stretchable materials. *Engineering Fracture Mechanics*, 188:300–308, Feb. 2018.

[15] T. M. Best, J. McElhaney, W. E. Garrett, and B. S. Myers. Characterization of the passive responses of live skeletal muscle using the quasi-linear theory of viscoelasticity. *Journal of Biomechanics*, 27(4):413–419, Apr. 1994.

[16] L. E. Bilston. Soft tissue rheology and its implications for elastography: Challenges and opportunities. *NMR in Biomedicine*, 31(10):e3832, 2018. e3832 NBM-17-0090.R1.

[17] K. Bircher, A. E. Ehret, and E. Mazza. Microstructure based prediction of the deformation behavior of soft collagenous membranes. *Soft Matter*, 13(30):5107–5116, 2017.

[18] K. Bircher, M. Zündel, M. Pensalfini, A. E. Ehret, and E. Mazza. Tear resistance of soft collagenous tissues. *Nature Communications*, 10(1):792, Feb. 2019.

[19] B. Boubaker, M. Pato, and E. Pires. A finite element model of skeletal muscle. *Virtual and Physical Prototyping*, 1:159–170, Sept. 2006.

[20] H. F. Brinson and L. C. Brinson. Nonlinear viscoelasticity. In *Polymer Engineering Science and Viscoelasticity: An Introduction*, pages 327–364. Springer US, Boston, MA, 2008.

[21] Y. Bu, L. Li, C. Yang, R. Li, and J. Wang. Measuring viscoelastic properties of living cells. *Acta Mechanica Solida Sinica*, 32(5):599–610, Oct. 2019.

[22] S. Bustamante, S. Bose, P. Bishop, R. Klatte, and F. Norris. Novel application of rapid prototyping for simulation of bronchoscopic anatomy. *Journal of cardiothoracic and vascular anesthesia*, 28:1122–5, Aug 2014.

[23] R. Cao, Z. Huang, T. Varghese, and G. Nabi. Tissue mimicking materials for the detection of prostate cancer using shear wave elastography: a validation study. *Medical physics*, 40:022903, Feb 2013.

[24] Y. Cao, G.-Y. Li, X. Zhang, and Y.-L. Liu. Tissue-mimicking materials for elastography phantoms: A review. *Extreme Mechanics Letters*, 17:62 – 70, 2017.

[25] A. Capilnasiu, L. Bilston, R. Sinkus, and D. Nordsletten. Nonlinear viscoelastic constitutive model for bovine liver tissue. *Biomechanics and Modeling in Mechanobiology*, pages 1–22, 2020.

[26] E. O. Carew, A. Garg, J. E. Barber, and I. Vesely. Stress relaxation preconditioning of porcine aortic valves. *Annals of Biomedical Engineering*, 32(4):563–572, Apr. 2004.

[27] T. Chanthasopeephan, J. P. Desai, and A. C. W. Lau. Measuring forces in liver cutting: New equipment and experimental results. *Annals of Biomedical Engineering*, 31(11):1372–1382, Dec 2003.

[28] T. Chanthasopeephan, J. P. Desai, and A. C. W. Lau. Determining fracture characteristics in scalpel cutting of soft tissue. In *The First IEEE/RAS-EMBS International Conference on Biomedical Robotics and Biomechatronics, 2006. BioRob 2006.*, pages 899–904, Feb 2006.

[29] S. Chatelin, J. Oudry, N. Périchon, L. Sandrin, P. Allemann, L. Soler, and R. Willinger. In vivo liver tissue mechanical properties by transient elastography: comparison with dynamic mechanical analysis. *Biorheology*, 48:75–88, 2011.

[30] D. Chimich, N. Shrive, C. Frank, L. Marchuk, and R. Bray. Water content alters viscoelastic behaviour of the normal adolescent rabbit medial collateral ligament. *Journal of Biomechanics*, 25(8):831–837, 1992.

[31] M. V. Chin-Purcell and J. L. Lewis. Fracture of articular cartilage. *J Biomech Eng*, 118(4):545–556, Jan. 1996.

[32] C. Chui, E. Kobayashi, X. Chen, T. Hisada, and I. Sakuma. Combined compression and elongation experiments and non-linear modelling of liver tissue for surgical simulation. *Medical and Biological Engineering and Computing*, 42(6):787–798, Nov. 2004.

[33] C. Chui, E. Kobayashi, X. Chen, T. Hisada, and I. Sakuma. Transversely isotropic properties of porcine liver tissue: experiments and constitutive modelling. *Medical & biological engineering & computing*, 45:99–106, Jan 2007.

[34] J. Claflin and S. A. Waits. Three dimensionally printed interactive training model for kidney transplantation. *Journal of surgical education*, 77:1013–1017, Sep-Oct 2020.

[35] G. Cooney, A. Kiernan, D. Winter, and C. Simms. Optimised suture-based wound closure using a biomechanical abdominal model. *British Journal of Surgery*, 105:395–400, Feb. 2018.

[36] M. Czerner, M. Czerner, L. A. Fasce, J. F. Martucci, R. Ruseckaite, and P. M. Frontini. Deformation and fracture behavior of physical gelatin gel systems. *Food hydrocolloids*, v. 60:pp. 299–307–2016 v.60, 2016.

[37] G. Doucet, S. Ryan, M. Bartellas, M. Parsons, A. Dubrowski, and T. Renouf. Modelling and manufacturing of a 3d printed trachea for cricothyroidotomy simulation. *Cureus*, 9:e1575, Aug 2017.

[38] K. M. Dunford, T. LeRoith, and A. R. Kemper. Effects of postmortem time and storage fluid on the material properties of bovine liver parenchyma in tension. *Journal of the Mechanical Behavior of Biomedical Materials*, 87:240–255, Nov. 2018.

[39] S.-J. Estermann, D. H. Pahr, and A. Reisinger. Hyperelastic and viscoelastic characterization of hepatic tissue under uniaxial tension in time and frequency domain. *Journal of the Mechanical Behavior of Biomedical Materials*, 112:104038, 2020.

[40] S.-J. Estermann, D. H. Pahr, and A. Reisinger. Quantifying tactile properties of liver tissue, silicone elastomers, and a 3d printed polymer for manufacturing realistic organ models. *Journal of the Mechanical Behavior of Biomedical Materials*, 104:103630, 2020.

[41] M. M. Fedewa, T. R. J. Oegema, M. H. Schwartz, A. MacLeod, and J. L. Lewis. Chondrocytes in culture produce a mechanically functional tissue. *Journal of orthopaedic research : official publication of the Orthopaedic Research Society*, 16:227–36, Mar 1998.

[42] T. Finni, J. Peltonen, L. Stenroth, and N. J. Cronin. Viewpoint: On the hysteresis in the human achilles tendon. *Journal of Applied Physiology*, 114(4):515–517, Mar. 2024.

[43] M. M. Fitzgerald, K. Bootsma, J. A. Berberich, and J. L. Sparks. Tunable stress relaxation behavior of an alginate-polyacrylamide hydrogel: Comparison with muscle tissue. *Biomacromolecules*, 16(5):1497–1505, May 2015.

[44] D. Fovargue, S. Kozerke, R. Sinkus, and D. Nordsletten. Robust mr elastography stiffness quantification using a localized divergence free finite element reconstruction. *Medical Image Analysis*, 44:126–142, Feb. 2018.

[45] M. Frank, D. Marx, V. Nedelkovski, J.-T. Fischer, D. H. Pahr, and P. J. Thurner. Dehydration of individual bovine trabeculae causes transition from ductile to quasi-brittle failure mode. *Journal of the Mechanical Behavior of Biomedical Materials*, 87:296–305, Nov. 2018.

[46] J. R. Fredieu, J. Kerbo, M. Herron, R. Klatte, and M. Cooke. Anatomical models: a digital revolution. *Medical Science Educator*, 25(2):183–194, Jun 2015.

[47] Y. Fung. *Biomechanics: Mechanical Properties of Living Tissues*. Springer, 1993.

[48] Z. Gao, K. Lister, and J. P. Desai. Constitutive modeling of liver tissue: Experiment and theory. *Annals of Biomedical Engineering*, 38(2):505–516, Feb 2010.

[49] J. Garcia, M. AlOmran, A. Emmott, R. Mongrain, K. Lachapelle, and R. Leask. Tunable 3d printed multi-material composites to enhance tissue fidelity for surgical simulation. 2018.

[50] J. I. Gear, C. Cummings, A. J. Craig, A. Divoli, C. D. C. Long, M. Tapner, and G. D. Flux. Abdo-man: a 3d-printed anthropomorphic phantom for validating quantitative sirt. *EJNMMI physics*, 3:17, Dec 2016.

[51] R. Gharleghi, C. Dessalles, R. Lal, S. McCraith, K. Sarathy, N. Jepson, J. Otton, A. Barakat, and S. Beier. 3d printing for cardiovascular applications: From end-to-end processes to emerging developments. *Annals of Biomedical Engineering*, 49, May 2021.

[52] J. M. Giles, A. E. Black, and J. E. Bischoff. Anomalous rate dependence of the preconditioned response of soft tissue during load controlled deformation. *Journal of Biomechanics*, 40(4):777–785, Jan. 2007.

[53] G. D. Goh, S. L. Sing, Y. F. Lim, J. L. J. Thong, Z. K. Peh, S. R. Mogali, and W. Y. Yeong. Machine learning for 3d printed multi-materials tissue-mimicking anatomical models. *Materials & Design*, 211:110125, Dec. 2021.

[54] C. Gokgol, C. Basdogan, and D. Canadinc. Estimation of fracture toughness of liver tissue: Experiments and validation. *Medical Engineering & Physics*, 34(7):882 – 891, 2012.

[55] D. Gutierrez-Lemini. *Engineering Viscoelasticity*. Springer, New York, http://dx.doi.org/10.1007/978-1-4614-8139-3., 1 edition, 2014.

[56] N. Hammad, J. Mansfield, E. Green, J. Bell, B. Knight, N. Liversedge, J. C. Tham, R. Welbourn, A. Shore, K. Kos, and C. Winlove. The mechanical properties of human adipose tissues and their relationships to the structure and composition of the extracellular matrix. *American journal of physiology. Endocrinology and metabolism*, 305, 10 2013.

[57] M. Hao, J. Wang, R. Wang, M. Gong, L. Zhang, D. Wang, Y. Lu, L. Zhang, and X. Lin. Mechanical dependence of 3d-printed thermoplastic polyurethane reinforced with minor continuous carbon fibres. *Virtual and Physical Prototyping*, 18(1):e2224304, Dec. 2023.

[58] C. Hazelaar, M. van Eijnatten, M. Dahele, J. Wolff, T. Forouzanfar, B. Slotman, and W. F. A. R. Verbakel. Using 3d printing techniques to create an anthropomorphic thorax phantom for medical imaging purposes. *Medical physics*, 45:92–100, Jan 2018.

[59] I. Hernandez-Giron, J. M. den Harder, G. J. Streekstra, J. Geleijns, and W. J. H. Veldkamp. Development of a 3d printed anthropomorphic lung phantom for image quality assessment in ct. *Physica medica : PM : an international journal devoted to the applications of physics to medicine and biology : official journal of the Italian Association of Biomedical Physics (AIFB)*, 57:47–57, Jan 2019.

[60] M. Hollenstein, A. Nava, D. Valtorta, J. G. Snedeker, and E. Mazza. Mechanical characterization of the liver capsule and parenchyma. In M. Harders and G. Székely, editors, *Biomedical Simulation*, pages 150–158, Berlin, Heidelberg, 2006. Springer Berlin Heidelberg.

[61] T. Ishii, K. Fukumitsu, E. Ogawa, T. Okamoto, and S. Uemoto. Living donor liver transplantation in situs inversus totalis with a patient-specific three-dimensional printed liver model. *Pediatric Transplantation*, 24(3):e13675, 2020.

[62] R. L. Izzo, R. P. O'Hara, V. Iyer, R. Hansen, K. M. Meess, S. V. S. Nagesh, S. Rudin, A. H. Siddiqui, M. Springer, and C. N. Ionita. 3d printed cardiac phantom for procedural planning of a transcatheter native mitral valve replacement. *Proceedings of SPIE–the International Society for Optical Engineering*, 9789(28615797):978908, Feb. 2016.

[63] L. Jaksa, D. Pahr, G. Kronreif, and A. Lorenz. Development of a multi-material 3d printer for functional anatomic models. *International journal of bioprinting*, 7:420, 2021.

[64] L. Jaksa, D. Pahr, G. Kronreif, and A. Lorenz. Calibration dependencies and accuracy assessment of a silicone rubber 3d printer. *Inventions*, 7(2), 2022.

[65] M. Jaradat, E. Soliman, and M. Reda Taha. 3d-printed bio-inspired mechanically interlocked viscoelastic dampers for energy dissipation. *Materials & Design*, 228:111826, Apr. 2023.

[66] Z. Jin, Y. Li, K. Yu, L. Liu, J. Fu, X. Yao, A. Zhang, and Y. He. 3d printing of physical organ models: Recent developments and challenges. *Advanced Science*, 8(17):2101394, 2021.

[67] P. Jordan, A. E. Kerdok, R. D. Howe, and S. Socrate. Identifying a minimal rheological configuration: A tool for effective and efficient constitutive modeling of soft tissues. *J Biomech Eng*, 133(4), Mar. 2011.

[68] P. Jordan, S. Socrate, T. E. Zickler, and R. D. Howe. Constitutive modeling of porcine liver in indentation using 3d ultrasound imaging. *Papers from the Second International Conference on the Mechanics of Biomaterials and Tissues*, 2(2):192–201, Apr. 2009.

[69] A. R. Kemper, A. C. Santago, J. D. Stitzel, J. L. Sparks, and S. M. Duma. Biomechanical response of human liver in tensile loading. *Annals of advances in automotive medicine. Association for the Advancement of Automotive Medicine. Annual Scientific Conference*, 54:15–26, 2010.

[70] A. R. Kemper, A. C. Santago, J. D. Stitzel, J. L. Sparks, and S. M. Duma. Effect of strain rate on the material properties of human liver parenchyma in unconfined compression. *Journal of Biomechanical Engineering*, 135(10):104503, 2013.

[71] M. Khadem, B. Fallahi, C. Rossa, R. Sloboda, N. Usmani, and M. Tavakoli. *A Mechanics-based Model for Simulation and Control of Flexible Needle Insertion in Soft Tissue*, volume 2015. May 2015.

[72] L. Kiraly, M. Tofeig, N. K. Jha, and H. Talo. Three-dimensional printed prototypes refine the anatomy of post-modified norwood-1 complex aortic arch obstruction and allow presurgical simulation of the repair. *Interactive cardiovascular and thoracic surgery*, 22:238–40, Feb 2016.

[73] A. S. Kobayashi. *Springer handbook of Experimental Solid Mechanics*. Springer, 2008.

[74] J. H. Koolstra, E. Tanaka, and T. M. G. J. Van Eijden. Viscoelastic material model for the temporomandibular joint disc derived from dynamic shear tests or strain-relaxation tests. *Journal of Biomechanics*, 40(10):2330–2334, Jan. 2007.

[75] B. E. Koop and J. L. Lewis. A model of fracture testing of soft viscoelastic tissues. *Journal of Biomechanics*, 36(4):605–608, Apr. 2003.

[76] S. N. Kurenov, C. Ionita, D. Sammons, and T. L. Demmy. Three-dimensional printing to facilitate anatomic study, device development, simulation, and planning in thoracic surgery. *The Journal of thoracic and cardiovascular surgery*, 149:973–9.e1, Apr 2015.

[77] W. Li, B. Belmont, J. M. Greve, A. B. Manders, B. C. Downey, X. Zhang, Z. Xu, D. Guo, and A. Shih. Polyvinyl chloride as a multimodal tissue-mimicking material with tuned mechanical and medical imaging properties. *Medical Physics*, 43(10):5577–5592, 2016.

[78] J. Lim and J. Kim. 3d vascular replicas composed of elastomer-hydrogel skin multilayers for simulation of endovascular intervention. *Adv. Funct. Mater.*, 30(51):2003395, Feb. 2020.

[79] F. Liu, Q. Chen, C. Liu, Q. Ao, X. Tian, J. Fan, H. Tong, and X. Wang. Natural polymers for organ 3d bioprinting. *Polymers*, 10(11), 2018.

[80] Z. Liu and L. Bilston. On the viscoelastic character of liver tissue: experiments and modelling of the linear behaviour. *Biorheology*, 37:191–201, 2000.

[81] Y.-C. Lu, A. R. Kemper, and C. D. Untaroiu. Effect of storage on tensile material properties of bovine liver. *Journal of the Mechanical Behavior of Biomedical Materials*, 29:339–349, Jan. 2014.

[82] O. Lund, V. Chandrasekaran, R. Grocott-Mason, H. Elwidaa, R. Mazhar, A. Khaghani, A. Mitchell, C. Ilsley, and M. H. Yacoub. Primary aortic valve replacement with allografts over twenty-five years: valve-related and procedure-related determinants of outcome. *The Journal of thoracic and cardiovascular surgery*, 117:77–90; discussion 90–1, Jan 1999.

[83] D. B. MacManus, M. Maillet, S. O'Gorman, B. Pierrat, J. G. Murphy, and M. D. Gilchrist. Sex- and age-specific mechanical properties of liver tissue under dynamic loading conditions. *Journal of the Mechanical Behavior of Biomedical Materials*, 99:240–246, Nov. 2019.

[84] M. M. Maddox, A. Feibus, J. Liu, J. Wang, R. Thomas, and J. L. Silberstein. 3d-printed soft-tissue physical models of renal malignancies for individualized surgical simulation: a feasibility study. *Journal of robotic surgery*, 12:27–33, Mar 2018.

[85] M. Mahvash and P. E. Dupont. Mechanics of dynamic needle insertion into a biological material. *IEEE Transactions on Biomedical Engineering*, 57(4):934–943, April 2010.

[86] M. A. Makary and M. Daniel. Medical error—the third leading cause of death in the us. *BMJ*, 353, 2016.

[87] S. Marconi, E. Negrello, V. Mauri, L. Pugliese, A. Peri, F. Argenti, F. Auricchio, and A. Pietrabissa. Toward the improvement of 3d-printed vessels' anatomical models for robotic surgery training. *The International journal of artificial organs*, 42:558–565, Oct 2019.

[88] E. Mazza, A. Nava, D. Hahnloser, W. Jochum, and M. Bajka. The mechanical response of human liver and its relation to histology: An in vivo study. *Medical Image Analysis*, 11(6):663–672, Dec. 2007.

[89] K. M. Meess, R. L. Izzo, M. L. Dryjski, R. E. Curl, L. M. Harris, M. Springer, A. H. Siddiqui, S. Rudin, and C. N. Ionita. 3d printed abdominal aortic aneurysm

phantom for image guided surgical planning with a patient specific fenestrated endovascular graft system. *Proceedings of SPIE–the International Society for Optical Engineering*, 10138, Feb 2017.

[90] W. T. Mehtsun, A. M. Ibrahim, M. Diener-West, P. J. Pronovost, and M. A. Makary. Surgical never events in the united states. *Surgery*, 153:465–72, Apr 2013.

[91] C. E. Miller, M. A. Vanni, and B. B. Keller. Characterization of passive embryonic myocardium by quasi-linear viscoelasticity theory. *Journal of Biomechanics*, 30(9):985 – 988, 1997.

[92] K. Miller. Constitutive modelling of abdominal organs. *Journal of biomechanics*, 33:367–73, Mar 2000.

[93] Y. Mine, H. Mitsui, Y. Oshima, Y. Noishiki, M. Nakai, and S. Sano. Suture retention strength of expanded polytetrafluoroethylene (eptfe) graft. *Acta medica Okayama*, 64:121–8, Apr. 2010.

[94] S. Misra, K. T. Ramesh, and A. M. Okamura. Modeling of tool-tissue interactions for computer-based surgical simulation: A literature review. *Presence: Teleoperators and Virtual Environments*, 17(5):463–491, 2008.

[95] B. H. P. Mobo, P. M. Rabinowitz, L. A. Conti, and O. A. Taiwo. Occupational health of animal workers., 2010.

[96] K. M. Moerman, C. K. Simms, and T. Nagel. Control of tension-compression asymmetry in ogden hyperelasticity with application to soft tissue modelling. *Journal of the Mechanical Behavior of Biomedical Materials*, 56:218–228, Mar. 2016.

[97] I. K. Moppett and S. H. Moppett. Surgical caseload and the risk of surgical never events in england. *Anaesthesia*, 71(1):17–30, 2016.

[98] D. A. Morrow, T. L. Haut Donahue, G. M. Odegard, and K. R. Kaufman. Transversely isotropic tensile material properties of skeletal muscle tissue. *Journal of the Mechanical Behavior of Biomedical Materials*, 3(1):124–129, Jan. 2010.

[99] L. Mullins. Effect of Stretching on the Properties of Rubber. *Rubber Chemistry and Technology*, 21(2):281–300, 06 1948.

[100] L. Mullins and N. R. Tobin. Theoretical Model for the Elastic Behavior of Filler-Reinforced Vulcanized Rubbers. *Rubber Chemistry and Technology*, 30(2):555–571, 03 1957.

[101] A. Nava, E. Mazza, M. Furrer, P. Villiger, and W. H. Reinhart. In vivo mechanical characterization of human liver. *Medical Image Analysis*, 12(2):203–216, Apr. 2008.

[102] A. Nava, E. Mazza, O. Haefner, and M. Bajka. Experimental observation and modelling of preconditioning in soft biological tissues. In S. Cotin and D. Metaxas, editors, *Medical Simulation*, pages 1–8, Berlin, Heidelberg, 2004. Springer Berlin Heidelberg.

[103] A. Nekouzadeh and G. M. Genin. *Adaptive Quasi-Linear Viscoelastic Modeling*, chapter 1, pages 47–83. Springer Berlin Heidelberg, Berlin, Heidelberg, 2013.

[104] A. Nekouzadeh, K. Pryse, E. Elson, and G. Genin. A simplified approach to quasi-linear viscoelastic modeling. *Journal of biomechanics*, 40:3070–8, 02 2007.

[105] O. Nelles. *Nonlinear system identification: from classical approaches to neural networks and fuzzy models*. Springer Science & Business Media, 2013.

[106] X. Nie, J.-I. Cheng, W. W. Chen, and T. Weerasooriya. Dynamic tensile response of porcine muscle. *Journal of Applied Mechanics*, 78(2), nov 2010.

[107] A. M. Okamura, C. Simone, and M. D. O'leary. Force modeling for needle insertion into soft tissue. *IEEE transactions on biomedical engineering*, 51(10):1707–1716, 2004.

[108] C. Okeke, A. Thite, J. Durodola, N. Fellows, and M. Greenrod. Modelling of hyperelastic polymers for automotive lamps under random vibration loading with proportional damping for robust fatigue analysis. *Procedia Structural Integrity*, 13, Dec. 2018.

[109] M. Oyen and R. Cook. Technique for estimating fracture resistance of cultured neocartilage. *Journal of materials science. Materials in medicine*, 12:327–32, May 2001.

[110] M. Pensalfini, S. Meneghello, V. Lintas, K. Bircher, A. Ehret, and E. Mazza. The suture retention test, revisited and revised. *Journal of the Mechanical Behavior of Biomedical Materials*, 77, 08 2017.

[111] B. P. Pereira, P. W. Lucas, and T. Swee-Hin. Ranking the fracture toughness of thin mammalian soft tissues using the scissors cutting test. *Journal of Biomechanics*, 30(1):91–94, 1997.

[112] A. Pipkin and T. Rogers. A non-linear integral representation for viscoelastic behaviour. *Journal of the Mechanics and Physics of Solids*, 16(1):59–72, 1968.

[113] P. Provenzano, R. Lakes, T. Keenan, and R. vanderby. Nonlinear ligament viscoelasticity. *Annals of Biomedical Engineering*, 29(10):908–914, Oct. 2001.

[114] K. M. Pryse, A. Nekouzadeh, G. M. Genin, E. L. Elson, and G. I. Zahalak. Incremental mechanics of collagen gels: new experiments and a new viscoelastic model. *Annals of biomedical engineering*, 31:1287–96, Nov 2003.

[115] P. P. Purslow. Measurement of the fracture toughness of extensible connective tissues. *Journal of Materials Science*, 18(12):3591–3598, Dec. 1983.

[116] K. Qiu, G. Haghiashtiani, and M. C. McAlpine. 3d printed organ models for surgical applications. *Annual Review of Analytical Chemistry*, 11(1):287–306, 2018. PMID: 29589961.

[117] K. Qiu, G. Haghiashtiani, and M. C. McAlpine. 3d printed organ models for surgical applications. *Annual Review of Analytical Chemistry*, 11(1):287–306, 2018. PMID: 29589961.

[118] K. Qiu, Z. Zhao, G. Haghiashtiani, S.-Z. Guo, M. He, R. Su, Z. Zhu, D. B. Bhuiyan, P. Murugan, F. Meng, S. H. Park, C.-C. Chu, B. M. Ogle, D. A. Saltzman, B. R. Konety, R. M. Sweet, and M. C. McAlpine. 3d printed organ models with physical properties of tissue and integrated sensors. *Advanced Materials Technologies*, 3(3):1700235, 2018.

[119] C. Quaia, H. S. Ying, A. M. Nichols, and L. M. Optican. The viscoelastic properties of passive eye muscle in primates. i: Static forces and step responses. *PLOS ONE*, 4(4):e4850, Apr. 2009.

[120] C. Quaia, H. S. Ying, and L. M. Optican. The viscoelastic properties of passive eye muscle in primates. ii: testing the quasi-linear theory. *PloS one*, 4(19649257):e6480–e6480, Aug. 2009.

[121] C. Quaia, H. S. Ying, and L. M. Optican. The viscoelastic properties of passive eye muscle in primates. iii: Force elicited by natural elongations. *PLOS ONE*, 5(3):e9595, Mar. 2010.

[122] N. L. Ramo, C. M. Puttlitz, and K. L. Troyer. The development and validation of a numerical integration method for non-linear viscoelastic modeling. *PloS one*, 13(29293558):e0190137–e0190137, Jan. 2018.

[123] M. Randazzo, J. M. Pisapia, N. Singh, and J. P. Thawani. 3d printing in neurosurgery: A systematic review. *Surg Neurol Int*, 7(Suppl 33):S801–S809, 2016.

[124] A. Rethy, J. O. Sæternes, J. Halgunset, R. Mårvik, E. F. Hofstad, J. A. Sánchez-Margallo, and T. Langø. Anthropomorphic liver phantom with flow for multimodal image-guided liver therapy research and training. *International journal of computer assisted radiology and surgery*, 13:61–72, Jan 2018.

[125] E. Roan and K. Vemaganti. The nonlinear material properties of liver tissue determined from no-slip uniaxial compression experiments. *Journal of biomechanical engineering*, 129:450–6, Jun 2007.

[126] W. J. Rugh. *Nonlinear system theory*. Johns Hopkins University Press Baltimore, MD, 1981.

[127] A. Scerrati, F. Trovalusci, A. Albanese, G. S. Ponticelli, V. Tagliaferri, C. L. Sturiale, M. A. Cavallo, and E. Marchese. A workflow to generate physical 3d models of cerebral aneurysms applying open source freeware for cad modeling and 3d printing. *Interdisciplinary Neurosurgery*, 17:1–6, Sept. 2019.

[128] R. A. Schapery. On the characterization of nonlinear viscoelastic materials. *Polymer Engineering & Science*, 9(4):295–310, 1969.

[129] Z. L. Shen, H. Kahn, R. Ballarini, and S. J. Eppell. Viscoelastic properties of isolated collagen fibrils. *Biophysical journal*, 100(21689535):3008–3015, June 2011.

[130] T. Shin, O. Ukimura, and I. S. Gill. Three-dimensional printed model of prostate anatomy and targeted biopsy-proven index tumor to facilitate nerve-sparing prostatectomy. *European Urology*, 69(2):377–379, Feb. 2016.

[131] R. Sinkus, S. Lambert, K. Z. Abd-Elmoniem, C. Morse, T. Heller, C. Guenthner, A. M. Ghanem, S. Holm, and A. M. Gharib. Rheological determinants for simultaneous staging of hepatic fibrosis and inflammation in patients with chronic liver disease. *NMR in Biomedicine*, 31(10):e3956, Oct. 2018.

[132] B. Smith and P. Dasgupta. 3d printing technology and its role in urological training. *World journal of urology*, 38:2385–2391, Oct 2020.

[133] D. Smith, U. Komaragiri, and R. Tanov. Calibration of nonlinear viscoelastic materials in abaqus using the adaptive quasi-linear viscoelastic model, smith, d., komaragiri, u., tanov, r. *2010 Similia Customer Conference*, May 2010.

[134] B. Song, W. Chen, Y. Ge, and T. Weerasooriya. Dynamic and quasi-static compressive response of porcine muscle. *Journal of Biomechanics*, 40(13):2999–3005, Jan. 2007.

[135] C. Storm, J. J. Pastore, F. C. MacKintosh, T. C. Lubensky, and P. A. Janmey. Nonlinear elasticity in biological gels. *Nature*, 435(7039):191–194, May 2005.

[136] Z. Sun and D. Liu. A systematic review of clinical value of three-dimensional printing in renal disease. *Quant Imaging Med Surg*, 8(3):311–325, Apr 2018.

[137] B. Takabi and B. L. Tai. A review of cutting mechanics and modeling techniques for biological materials. *Medical Engineering & Physics*, 45:1 – 14, 2017.

[138] K. Tan, S. Cheng, L. Jugé, and L. E. Bilston. Characterising soft tissues under large amplitude oscillatory shear and combined loading. *Journal of Biomechanics*, 46(6):1060–1066, Apr. 2013.

[139] D. Taylor. Measuring fracture toughness in biological materials. *Journal of the Mechanical Behavior of Biomedical Materials*, 77:776 – 782, 2018.

[140] D. Taylor, N. O'Mara, E. Ryan, M. Takaza, and C. Simms. The fracture toughness of soft tissues. *Journal of the Mechanical Behavior of Biomedical Materials*, 6:139 – 147, 2012.

[141] S. S. TROSTLE, D. G. WILSON, W. C. STONE, and M. D. MARKEL. A study of the biomechanical properties of the adult equine linea alba: Relationship of tissue bite size and suture material to breaking strength. *Veterinary Surgery*, 23(6):435–441, 1994.

[142] K. L. Troyer, D. J. Estep, and C. M. Puttlitz. Viscoelastic effects during loading play an integral role in soft tissue mechanics. *Acta Biomaterialia*, 8(1):234 – 243, 2012.

[143] A. Tsamis, J. T. Krawiec, and D. A. Vorp. Elastin and collagen fibre microstructure of the human aorta in ageing and disease: a review. *Journal of the Royal Society, Interface*, 10:20121004, Jun 2013.

[144] N. W. Tschoegl and N. W. Tschoegl. Energy storage and dissipation in a linear viscoelastic material. In *The Phenomenological Theory of Linear Viscoelastic Behavior: An Introduction*, pages 443–488. Springer Berlin Heidelberg, Berlin, Heidelberg, 1989.

[145] S. Umale, C. Deck, N. Bourdet, P. Dhumane, L. Soler, J. Marescaux, and R. Willinger. Experimental mechanical characterization of abdominal organs: liver, kidney & spleen. *Journal of the Mechanical Behavior of Biomedical Materials*, 17:22–33, Jan. 2013.

[146] I. Valverde, G. Gomez, J. F. Coserria, C. Suarez-Mejias, S. Uribe, J. Sotelo, M. N. Velasco, J. Santos De Soto, A.-R. Hosseinpour, and T. Gomez-Cia. 3d printed models for planning endovascular stenting in transverse aortic arch hypoplasia. *Catheterization and cardiovascular interventions : official journal of the Society for Cardiac Angiography & Interventions*, 85:1006–12, May 2015.

[147] M. Van Loocke, C. G. Lyons, and C. K. Simms. A validated model of passive muscle in compression. *Journal of biomechanics*, 39:2999–3009, 2006.

[148] M. Van Loocke, C. G. Lyons, and C. K. Simms. Viscoelastic properties of passive skeletal muscle in compression: stress-relaxation behaviour and constitutive modelling. *Journal of biomechanics*, 41:1555–66, 2008.

[149] M. Van Loocke, C. K. Simms, and C. G. Lyons. Viscoelastic properties of passive skeletal muscle in compression-cyclic behaviour. *Journal of biomechanics*, 42:1038–48, May 2009.

[150] C. Van Sligtenhorst, D. S. Cronin, and G. Wayne Brodland. High strain rate compressive properties of bovine muscle tissue determined using a split hopkinson bar apparatus. *Journal of biomechanics*, 39:1852–8, 2006.

[151] D. Veronda and R. Westmann. Mechanical characterization of skin—finite deformations. *Journal of Biomechanics*, 3(1):111–124, 1970.

[152] M. Vukicevic, B. Mosadegh, J. K. Min, and S. H. Little. Cardiac 3d printing and its future directions. *JACC Cardiovasc Imaging*, 10(2):171–184, 02 2017.

[153] M. Wagner, T. Werther, E. Unger, G. Kasprian, G. Dovjak, C. Dorfer, H. Schned, P. Steinbauer, K. Goeral, M. Olischar, K. Roessler, A. Berger, and G. Oberoi. Development of a 3d printed patient-specific neonatal brain simulation model using multimodality imaging for perioperative management. *Pediatric research*, 91:64–69, Jan 2022.

[154] K. Wang, C.-C. Ho, C. Zhang, and B. Wang. A review on the 3d printing of functional structures for medical phantoms and regenerated tissue and organ applications. *Engineering*, 3(5):653 – 662, 2017.

[155] K. Wang, C. Wu, Z. Qian, C. Zhang, B. Wang, and M. A. Vannan. Dual-material 3d printed metamaterials with tunable mechanical properties for patient-specific tissue-mimicking phantoms. *Additive Manufacturing*, 12:31 – 37, 2016.

[156] K. Wang, Y. Zhao, Y.-H. Chang, Z. Qian, C. Zhang, B. Wang, M. A. Vannan, and M.-J. Wang. Controlling the mechanical behavior of dual-material 3d printed meta-materials for patient-specific tissue-mimicking phantoms. *Materials & Design*, 90:704 – 712, 2016.

[157] X. Wang, J. Schoen, and M. Rentschler. A quantitative comparison of soft tissue compressive viscoelastic model accuracy. *Journal of the mechanical behavior of biomedical materials*, 20C:126–136, Jan. 2013.

[158] Y. Wang, X. Gao, Q. Yang, H. Wang, T. Shi, Y. Chang, C. Xu, and Y. Sun. Three-dimensional printing technique assisted cognitive fusion in targeted prostate biopsy. *Asian journal of urology*, 2:214–219, Oct 2015.

[159] C. Wex, A. Stoll, M. Fröhlich, S. Arndt, and H. Lippert. How preservation time changes the linear viscoelastic properties of porcine liver. *Biorheology*, 50(3-4):115–131, 2013.

[160] S. Wickramasinghe, O. Al-Ketan, C. Peng, Y. L. Tee, M. Kajtaz, and P. Tran. Influence of design parameters on the flexural properties of a bio-inspired suture structure. *Virtual and Physical Prototyping*, 18(1):e2204845, Dec. 2023.

[161] M. Xi, G. Yun, and B. Narsu. A mathematical model for viscoelastic properties of biological soft tissue. *Theory in Biosciences*, 141(1):13 – 25, 2022. Cited by: 0.

[162] Y. Xiao, E. A. Friis, S. H. Gehrke, and M. S. Detamore. Mechanical testing of hydrogels in cartilage tissue engineering: beyond the compressive modulus. *Tissue engineering. Part B, Reviews*, 19:403–12, Oct 2013.

[163] Y. xiong Zheng, D. fei Yu, J. gang Zhao, Y. lian Wu, and B. Zheng. 3d printout models vs. 3d-rendered images: Which is better for preoperative planning? *Journal of Surgical Education*, 73(3):518 – 523, 2016.

[164] Q. Xu, B. Engquist, M. Solaimanian, and K. Yan. A new nonlinear viscoelastic model and mathematical solution of solids for improving prediction accuracy. *Scientific Reports*, 10(1):2202, Feb. 2020.

[165] T. Q. Yang and Y. Chen. Stress response and energy dissipation in a linear viscoelastic material under periodic triangular strain loading. *J. Polym. Sci. Polym. Phys. Ed.*, 20(8):1437–1442, Aug. 1982.

[166] W. Yang, V. R. Sherman, B. Gludovatz, E. Schaible, P. Stewart, R. O. Ritchie, and M. A. Meyers. On the tear resistance of skin. *Nature Communications*, 6(1):6649, Mar. 2015.

[167] S.-J. Yoo, T. Spray, E. H. r. Austin, T.-J. Yun, and G. S. van Arsdell. Hands-on surgical training of congenital heart surgery using 3-dimensional print models. *The Journal of thoracic and cardiovascular surgery*, 153:1530–1540, Jun 2017.

[168] N. N. Zein, I. A. Hanouneh, P. D. Bishop, M. Samaan, B. Eghtesad, C. Quintini, C. Miller, L. Yerian, and R. Klatte. Three-dimensional print of a liver for preoperative planning in living donor liver transplantation. *Liver transplantation : official publication of the American Association for the Study of Liver Diseases and the International Liver Transplantation Society*, 19:1304–10, Dec 2013.

[169] M. Zhang, P. Nigwekar, B. Castaneda, K. Hoyt, J. V. Joseph, A. di Sant'Agnese, E. M. Messing, J. G. Strang, D. J. Rubens, and K. J. Parker. Quantitative characterization of viscoelastic properties of human prostate correlated with histology. *Ultrasound in Medicine and Biology*, 34(7):1033–1042, July 2008.

[170] X. Zhang, X. Gao, P. Zhang, Y. Guo, H. Lin, X. Diao, Y. Liu, C. Dong, Y. Hu, S. Chen, and X. Chen. Dynamic mechanical analysis to assess viscoelasticity of liver tissue in a rat model of nonalcoholic fatty liver disease. *Medical Engineering & Physics*, 44:79–86, June 2017.